CHALMERS UNIVERSITY OF TECHNOLOGY
Gothenburg, Sweden
www.chalmers.se

Galaxies do not live alone in the Universe. Many reside in galaxy clusters, the crowded cities of the cosmos, where they swim through a vast ocean of hot gas known as the intracluster medium. As they move through this environment and encounter other galaxies along their paths, their evolution can be dramatically transformed. Much like life in crowded cities can shape the lives of people, life in these dense cosmic environments can accelerate the aging of galaxies by stripping away the gas needed to form new stars.

This thesis explores these processes in the nearby Antlia Cluster using observations from the MeerKAT radio telescope in South Africa. By observing neutral atomic hydrogen, the raw material from which future stars are formed, it becomes possible to trace how galaxies are affected by their environments and how gas is removed from them over time.

Particular focus is placed on the spiral galaxy NGC 3281, which is observed undergoing multiple simultaneous evolutionary processes. The galaxy shows evidence of gas being stripped far beyond its disk, while also hosting an active supermassive black hole at its center. Together, these observations provide a detailed view of how dense environments can reshape galaxies and influence their evolution over cosmic time.

VICENTE HORACIO SALINAS FROEMEL • Through the Antlia Cluster: the environment shaping NGC 3281 • 2026

LICENTIATE THESIS

Through the Antlia Cluster: the environment shaping NGC 3281

VICENTE HORACIO
SALINAS FROEMEL

DEPARTMENT OF PHYSICS AND ASTRONOMY
CHALMERS UNIVERSITY OF TECHNOLOGY
Gothenburg, Sweden 2026
www.chalmers.se

THESIS FOR THE DEGREE OF LICENTIATE IN PHYSICS AND ASTRONOMY

Through the Antlia Cluster: the environment shaping NGC 3281

Vicente Horacio Salinas Froemel

Department of Physics and Astronomy
Chalmers University of Technology
Gothenburg, Sweden, 2026

Through the Antlia Cluster: the environment shaping NGC 3281

VICENTE HORACIO SALINAS FROEMEL

This thesis has been prepared using LaTeX.

Department of Physics and Astronomy
Chalmers University of Technology
SE-412 96 Gothenburg, Sweden
Phone: +46 (0)31 772 1000
www.chalmers.se

Printed by Chalmers Reproservice
Gothenburg, Sweden, April 2026

Abstract

Neutral atomic hydrogen (H I) provides the gas reservoir that fuels star formation and is highly sensitive to environmental mechanisms in galaxy clusters, making it a key tracer for understanding galaxy evolution. Environmental mechanisms in galaxy clusters alter the fate of this gas, thereby influencing galaxy evolution. These mechanisms range from gravitational interactions to hydrodynamical effects, which can ignite or enhance internal processes such as AGN activity, resulting in a complex interplay that shapes the observed properties of galaxies. In this licentiate thesis, we introduce the observational and theoretical framework required to study these processes, together with a detailed case study of a nearby galaxy undergoing these processes: We present an environmental study of the Seyfert 2 galaxy NGC 3281 in the Antlia cluster using deep MeerKAT H I and radio continuum observations, complemented by optical imaging. NGC 3281 hosts a truncated H I disk and is missing $\sim 81^{+12}_{-29}\%$ of its expected H I mass. We report the discovery of an isolated, large, starless H I cloud extending up to $\sim$ 200 kpc from NGC 3281 while carrying the kinematic signature of the galaxy's rotation. Together with two smaller nearby H I clouds, this material accounts for $\sim 18^{+25}_{-9}\%$ of the inferred missing H I. The H I morphology and distribution indicate ram pressure stripping as the dominant mechanism shaping the gas, while the complete detachment of the cloud and faint stellar features suggest that a past weak gravitational interaction contributed to loosening the gas reservoir. We estimate that the main H I cloud was stripped from the galaxy $\sim$ 300–350 Myr ago. We detect strong redshifted H I absorption consistent with ongoing cold gas inflow, and the radio continuum emission reveals kpc-scale bipolar outflows emerging from the nucleus. NGC 3281 therefore represents one of the clearest nearby examples of a galaxy undergoing multiple simultaneous evolutionary processes.

Keywords: Galaxy Evolution, Intracluster Medium, Galaxy Clusters, Ram Pressure Stripping, Gravitational Interactions, Active Galactic Nuclei.

List of Publications

This thesis is based on the following publications:

[A] **Vicente Salinas**, Kelley M. Hess, Junhyun Baek, Clara C. de la Casa, Ralf Kotulla, S. S. Sridhar, Hao Chen, Aeree Chung, Kana Morokuma-Matsui, Valeria Olivares, Yuanyuan Su, Ming Sun, “An environmental view of the galaxy NGC 3281”. To be submitted to MNRAS.

Acknowledgments

We acknowledge the use of the ilifu cloud computing facility – www.ilifu.ac.za, a partnership between the University of Cape Town, the University of the Western Cape, Stellenbosch University, Sol Plaatje University and the Cape Peninsula University of Technology. The ilifu facility is supported by contributions from the Inter-University Institute for Data Intensive Astronomy (IDIA – a partnership between the University of Cape Town, the University of Pretoria and the University of the Western Cape), the Computational Biology division at UCT and the Data Intensive Research Initiative of South Africa (DIRISA).

Acronyms

ΛCDM:	Lambda Cold Dark Matter
ICM:	Intracluster Medium
BCG:	Brightest Cluster Galaxy
AGN:	Active Galactic Nucleus
RPS:	Ram Pressure Stripping
ISM:	Interstellar Medium
CO:	Carbon Monoxide
H I:	Neutral atomic hydrogen
WSRT:	Westerbork Synthesis Radio Telescope
VLA:	Very Large Array
SMBH:	Supermassive Black Hole
EHT:	Event Horizon Telescope
BLR:	Broad-Line Region

NLR:	Narrow-Line Region
QSO:	Quasi-Stellar Object
SDSS:	Sloan Digital Sky Survey
HIM:	Hot Ionized Medium
WIM:	Warm Ionized Medium
WNM:	Warm Neutral Medium
CNM:	Cold Neutral Medium
sSFR:	Specific Star Formation Rate
UV:	Ultraviolet
SKA:	Square Kilometre Array
PSF:	Point Spread Function
IDIA:	Inter-University Institute for Data Intensive Astronomy
SIP:	SoFiA Image Pipeline

Contents

I Overview 1

II Publications 93

Part I

Overview

CHAPTER 1

Introduction

1.1 Galaxies

Galaxies do not evolve in isolation. Their observable properties, including morphology, stellar populations, gas content, and nuclear activity, are shaped by a continuous interplay between internal processes and their environment (Boselli and Gavazzi, 2006; Blanton and Moustakas, 2009; Cortese et al., 2021). Understanding how galaxies are transformed over cosmic time is one of the central questions of modern astrophysics (Somerville and Davé, 2015).

A galaxy is characterized as a gravitationally bound system composed of stars, gas, dust, and dark matter. In the context of the Lambda Cold Dark Matter (ΛCDM) model, such systems are formed from gas inside dark matter haloes, where it cools radiatively, and can become sufficiently dense for gravity to overcome internal pressure, allowing the gas to collapse and form stars (White and Rees, 1978). Subsequent evolution is governed not only by internal star formation and feedback, but also by external influences that can alter both their structure and gas reservoir. As a result, we find galaxies with a wide diversity of shapes, colors, and sizes.

In order to organize this diversity, early studies sought morphological classification schemes. These differences were systematically characterized by Hubble (1926)

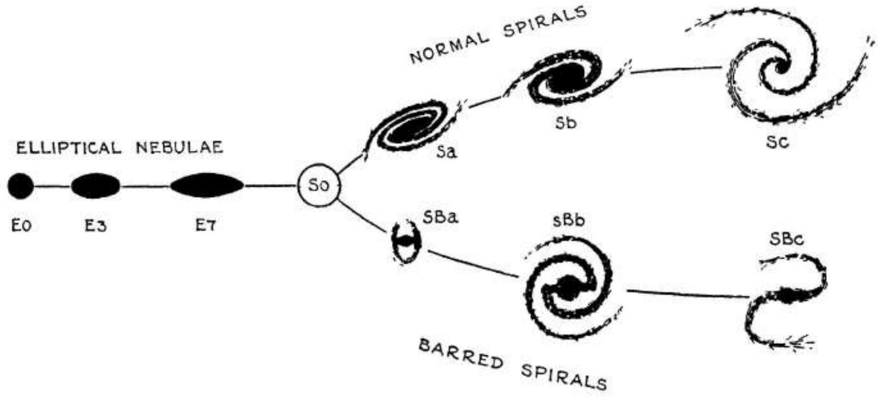

Figure 1.1: Hubble sequence (Hubble, 1936). From left to right, the diagram shows the progression from early-type to late-type galaxies.

and Hubble (1936), who introduced the Hubble sequence as a morphological framework for classifying galaxies (see Fig. 1.1). Here, spheroidal systems are classified as elliptical galaxies, while disk-like galaxies correspond to spiral galaxies, with lenticular galaxies (S0) occupying an intermediate position (Sandage, 1961). Outside of this scheme, irregular galaxies are also observed, which lack a well-defined morphology (de Vaucouleurs, 1959). Hubble grouped elliptical and lenticular galaxies into what he termed early-type galaxies, while spirals and irregulars were classified as late-type galaxies, reflecting the original interpretation that galaxies evolved from ellipticals into spirals. Later work showed that galaxies instead evolve in the other direction: from spiral to elliptical systems (A. Toomre and J. Toomre, 1972), but the terminology remained the same.

Late-type galaxies tend to be blue in color, which is characteristic of young stellar populations dominated by hot massive stars, while early-type galaxies have red colors associated with old stars (e.g. Strateva et al., 2001). The kinematic properties of galaxies also differ: spiral galaxies are supported by rotation and high angular momentum, which maintain a disk-like structure, while elliptical galaxies are dominated by disordered motions and high velocity dispersion (e.g. Binney and Tremaine, 2008). Together with the fact that elliptical galaxies are, on average, more massive than spirals, these properties hint at a formation history involving hierarchical growth through galaxy mergers (e.g. A. Toomre and J. Toomre, 1972; White and Rees, 1978). However, mergers are only one aspect of galaxy transformation. Because galaxies reside within a larger cosmic structure, their evolution is also influenced by their environments (Boselli and Gavazzi, 2006).

Galaxies are the fundamental building blocks of large-scale structure, providing an observable record of the formation and evolution of cosmic structure. Tracing how galaxies are transformed is thus the main goal of galaxy evolution studies, as this evolution is governed by the same physical laws that shape the Universe. They are ideal laboratories to explore a wide range of physical processes that operate across different scales and environments.

1.2 Environment and galaxy evolution

Galaxy clustering and large-scale structure

In the hierarchical growth of the Universe, galaxies assemble into a network known as the cosmic web (see Fig. 1.2). This structure is composed of filaments, sheets, and dense nodes, separated by large underdense regions known as voids (e.g. Bond et al., 1996). The cosmic web arises from primordial density fluctuations in the early Universe and evolves under the action of gravity. As galaxies flow along overdense regions, they progressively build larger structures, such as galaxy groups and, ultimately, massive galaxy clusters (e.g. Peebles, 1980), which occupy the nodes of the cosmic web. Galaxy clusters can contain hundreds to thousands of galaxies, and the space between them is filled with a hot, diffuse plasma known as the intracluster medium (ICM; Sarazin 1986). It is estimated that $\sim 80 - 90\%$ of the matter content in clusters is dark matter, $\sim 10 - 15\%$ is in the ICM, and less than $\sim 1\%$ resides in the stellar component of galaxies (Lin and Mohr, 2004; Gonzalez et al., 2007). At the center of galaxy clusters you typically find the brightest cluster galaxy (BCG), which is usually a massive elliptical galaxy (Kravtsov and Borgani, 2012).

If left alone, an isolated galaxy would form stars for as long as it has fuel to continue the process. Once this material is exhausted, the existing stars will become old, thus changing its optical color. The process by which star formation declines or ceases entirely is commonly referred to as quenching (Peng et al., 2010). However, a galaxy is unlikely to be left alone forever, as it will usually interact with its environment and encounter other galaxies as it moves through the cosmic web (Mo et al., 2010). Galaxies residing in high-density regions evolve differently from their counterparts in more isolated environments, commonly referred to as field galaxies. This environmental dependence is clearly illustrated by the morphology–density relation

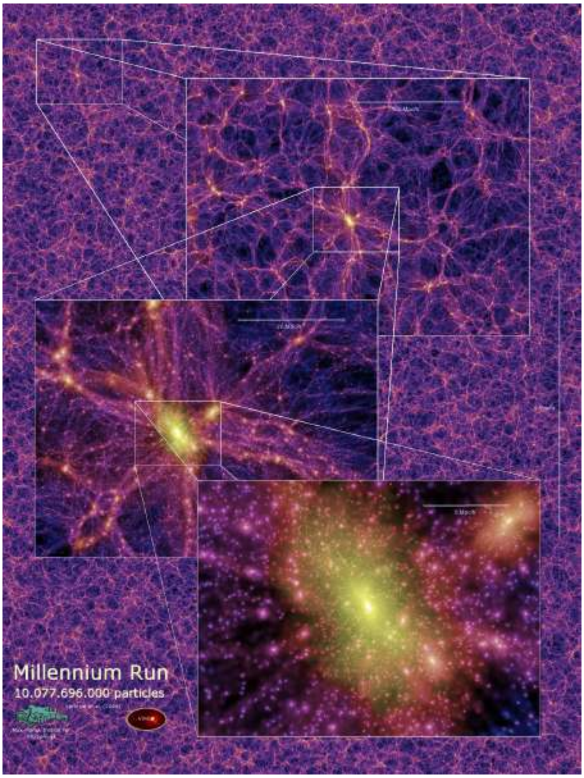

Figure 1.2: Large-scale structure from the Millennium Simulation (Springel et al., 2005). The image illustrates the filamentary distribution of dark matter as a result of the primordial density fluctuations from a ΛCDM model.

presented by Dressler (1980): as shown in Fig. 1.3, the fraction of elliptical galaxies increases with local density, while the fraction of late-type galaxies decreases. This result suggests that galaxies in dense environments are subject to external processes that can accelerate their evolutionary transformation.

Environmental mechanisms

The processes driving galaxy evolution can be broadly divided into internal and external mechanisms (Somerville and Davé, 2015). Internal mechanisms, as the name

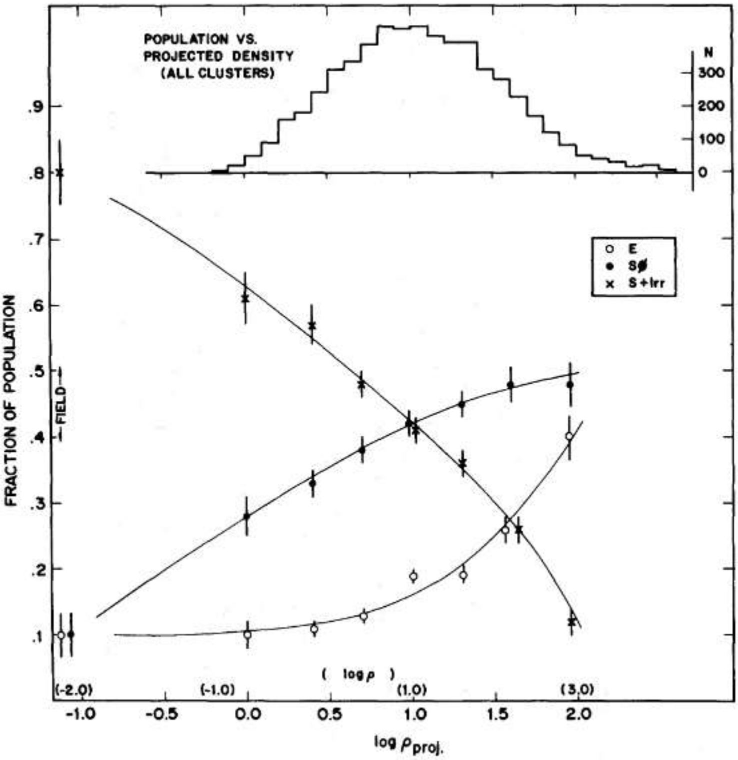

Figure 1.3: Morphology-density relation from (Dressler, 1980). Open circles are elliptical galaxies (E), filled circles are lenticular galaxies (S0), and crosses are spirals plus irregular galaxies (S+Irr).

indicates, originate within the galaxy itself and include gravitational instabilities, stellar feedback from supernova explosions, and outflows powered by active galactic nuclei (AGN; Kormendy and Ho 2013). These processes regulate star formation and can heat or expel gas from the galactic disk.

External mechanisms arise from interactions between a galaxy and its surrounding environment. These can be further classified into gravitational and hydrodynamical processes. Gravitational effects include galaxy–galaxy interactions, tidal interactions with the cluster potential (Merritt, 1983; Byrd and Valtonen, 1990), and the cumulative impact of multiple rapid encounters, commonly referred to as harassment (Moore et al., 1998). In extreme cases, gravitational interactions can lead to galaxy mergers, resulting in the formation of a more massive system (A. Toomre and J. Toomre, 1972).

Hydrodynamical processes occur when a galaxy interacts with the ambient medium. Examples include ram pressure stripping (Gunn and Gott, 1972), viscous stripping (Nulsen, 1982), thermal evaporation (Cowie and McKee, 1977; Cowie and Songaila, 1977), and starvation (Larson et al., 1980). Among these, ram pressure stripping (RPS) is one of the most extensively studied and can have a profound impact on galaxy evolution. This process occurs when the ICM exerts pressure on the interstellar medium (ISM) of a galaxy, removing gas from the galaxy and thereby suppressing future star formation.

1.3 Cold gas in galaxies

The component most directly affected by many of these mechanisms is the cold gas reservoir of a galaxy, which serves as the primary fuel for star formation (e.g. Kennicutt, 1998). Understanding how physical processes alter the distribution and state of the cold gas is therefore central to understanding galaxy evolution.

Cold gas can primarily be found in two phases: molecular and neutral atomic. The molecular phase is dominated by H_2 and is most directly associated with ongoing star formation, as stars form in dense molecular clouds. Since H_2 does not emit efficiently at the low temperatures typical of molecular clouds, it is commonly traced through emission from carbon monoxide (CO), which serves as a proxy for the molecular gas content (e.g. Bolatto et al., 2013).

The neutral atomic gas, commonly referred to as H I, is typically more extended than the stellar disk (e.g. Broeils and M.-H. Rhee, 1997). Being the most weakly bound baryonic component of a galaxy, it is especially vulnerable to environmental processes such as tidal interactions and RPS.

H I emits radiation at a wavelength of 21 cm (rest frequency of 1420.4 MHz) due to the hyperfine transition of the hydrogen atom (Field, 1958). This is a highly forbidden transition with an extremely low probability, corresponding to a mean lifetime of order 10^7 years for an individual hydrogen atom. Nevertheless, because galaxies contain vast quantities of H I, the collective emission from many atoms makes the 21 cm line readily observable, enabling direct measurements of the atomic gas content of galaxies (e.g. M. J. Meyer et al., 2004). The integrated 21 cm emission yields the total H I mass of a galaxy, while the Doppler shift of the line traces the line-of-sight velocity, providing direct information on the gas kinematics.

1.4 Radio telescopes and interferometry

The 21 cm line lies in the radio part of the electromagnetic spectrum and is therefore observed with radio telescopes. A single-dish radio telescope typically consists of a large parabolic reflector that collects and focuses incoming radio waves onto a receiver. The angular resolution of a telescope is set by the ratio between the observed wavelength (λ) and the diameter of the dish (D), approximately given by

$$\theta \approx 1.2\,\frac{\lambda}{D} \tag{1.1}$$

Because the 21 cm line corresponds to a relatively long wavelength, achieving high angular resolution requires a large dish diameter. In practice, this makes it challenging for single-dish telescopes to resolve fine spatial structure in distant galaxies. To overcome this limitation, multiple radio antennas can be combined to form what is known as an interferometer (Ryle and Hewish, 1960). By correlating the signals received by antennas separated by large distances, it is possible to achieve an angular resolution equivalent to that of a single dish whose diameter equals the maximum separation between antennas (i.e. the maximum baseline, where a baseline refers to the separation between any pair of antennas). In this case, the angular resolution is approximately given by

$$\theta \approx \frac{\lambda}{B_{\rm max}}, \tag{1.2}$$

where $B_{\rm max}$ denotes the maximum projected baseline length of the array.

Interferometric arrays can therefore span many kilometers, providing the angular resolution required to spatially resolve the distribution of H I in galaxies. Such spatially resolved observations are essential for distinguishing between different environmental mechanisms, as gravitational interactions and RPS leave distinct signatures in the gas morphology and kinematics. This capability has been fundamental in advancing our understanding of the role of cold gas in galaxy evolution. By resolving the structure of H I disks, such observations have revealed extended gas envelopes, tidal features, asymmetries, and truncated gas disks, particularly in dense environments.

A major development in radio interferometry was the construction of the West-

Figure 1.4: The Karl G. Jansky Very Large Array (VLA) located on the Plains of San Agustin in New Mexico, USA. The array consists of 27 antennas arranged in a Y-shaped configuration, providing baselines up to 36 km and enabling high-resolution radio imaging. Image credit: NRAO/AUI/NSF.

erbork Synthesis Radio Telescope (WSRT) in the Netherlands and later the Karl G. Jansky Very Large Array (VLA) in New Mexico, USA (see Fig. 1.4). These facilities enabled spatially resolved H I imaging of nearby galaxies at angular resolutions far superior to single-dish observations. Early WSRT studies of Virgo Cluster galaxies (Warmels, 1988) first quantified the H I deficiency of cluster spirals relative to field galaxies. Subsequent higher-resolution observations with the VLA (Cayatte et al., 1990; Chung et al., 2009) revealed that the atomic gas disks of cluster galaxies are often significantly truncated and morphologically disturbed compared to their stellar components. Together, these results provided the smoking gun for environmentally driven gas removal processes and firmly established spatially resolved H I imaging as a decisive tool for studying galaxy evolution.

1.5 Thesis outline

This licentiate thesis investigates how dense environments influence the cold gas reservoirs of galaxies and how such environmental processes may be connected to nuclear activity. Using deep H I and radio continuum observations of the Antlia cluster, with particular focus on the spiral galaxy NGC 3281, this work explores the interplay between RPS, gravitational perturbations, and active galactic nucleus fueling.

The structure of the thesis is as follows. Chapter 2 introduces the environmental framework of galaxy evolution, describing galaxy environments and clusters, and detailing both gravitational and hydrodynamical mechanisms responsible for gas removal and star formation quenching. Chapter 3 focuses on the cold gas component of galaxies, beginning with its role in star formation and nuclear activity, and then presenting H I, its emission and absorption properties, observational limitations, and the presence of cold gas beyond galactic disks. Chapter 4 presents the principles of radio interferometric imaging, including uv coverage, weighting schemes, resolution–sensitivity trade-offs, and the motivation for multi-resolution imaging. Chapter 5 describes the observational data and analysis strategy adopted in this work, including imaging parameter choices, source finding and masking, and continuum subtraction. Chapter 6 introduces the target system and its cluster environment, summarizing ancillary data and the observational context prior to the presentation of the research article that constitutes the main scientific contribution of this thesis.

CHAPTER 2

Galaxy Evolution in Dense Environments

2.1 Galaxy environments

Galaxies reside in a wide range of environments that differ significantly in density, gravitational potential, and gas content. These range from relatively isolated field regions to galaxy groups and massive clusters, forming a continuous hierarchy in density and mass across the cosmic web (Bond et al., 1996; Springel et al., 2005).

In low-density environments such as the field, galaxies evolve largely through internal mechanisms, including star formation, stellar and supernova feedback, and other secular processes within their disks. In contrast, galaxies residing in groups and clusters are subject to additional external influences arising from interactions with neighboring galaxies and with the surrounding medium (Boselli and Gavazzi, 2006; Blanton and Moustakas, 2009; Cortese et al., 2021). These environmental effects can significantly modify the distribution of cold gas, star formation activity, and ultimately the morphology of the galaxy (Dressler, 1980; Peng et al., 2010).

Between these extremes lie the filamentary structures of the cosmic web, which connect galaxy groups and clusters over megaparsec scales (Aragón-Calvo et al., 2010). Filaments act as pathways through which matter flows toward the densest nodes of large-scale structure. Galaxies located within these structures can exhibit mild to intermediate properties between those of field and cluster galaxies (O'Kane et al., 2024), suggesting that environmental influences may already begin to affect their evolution before they reach the densest regions. As they migrate along these structures, galaxies are gradually incorporated into galaxy groups and clusters, where environmental effects become progressively stronger.

Galaxy groups represent intermediate-density environments typically containing a few to several tens of galaxies, where gravitational interactions and mergers are relatively common. Compared to clusters, the lower velocity dispersions in groups make galaxy–galaxy interactions more efficient (Ostriker, 1980; Makino and Hut, 1997), allowing tidal encounters and mergers to play a significant role in driving galaxy evolution.

In many cases, galaxies that are observed in clusters today have previously resided in smaller groups. As a result, some evolutionary transformations may occur before galaxies enter the cluster environment, a process commonly referred to as preprocessing (Fujita, 2004). Consequently, galaxies may already undergo significant evolutionary changes before being accreted into a cluster, and the observed properties of cluster galaxies may reflect a combination of processes acting both prior to and after their accretion into the cluster environment.

2.2 Galaxy clusters

Galaxy clusters are the most massive gravitationally bound structures in the Universe, typically containing hundreds to thousands of galaxies embedded within dark matter halos with masses of order 10^{14}–$10^{15}\ M_\odot$ (Allen et al., 2011). In addition to their galaxy populations, these systems host a large reservoir of hot, diffuse plasma known as the intracluster medium (ICM), briefly introduced in Section 1.2.

The ICM reaches temperatures of 10^7–10^8 K and emits strongly at X-ray wavelengths through thermal bremsstrahlung radiation (Sarazin, 1986). X-ray observations therefore provide a powerful probe of the thermodynamic state and spatial distribution of the intracluster gas.

Galaxy clusters are strongly dominated by dark matter. Observations of galaxy dynamics, gravitational lensing, and X-ray measurements of the ICM indicate that most of the cluster mass resides in an extended dark matter halo (Zwicky, 1933; Clowe et al., 2006; Vikhlinin et al., 2006). Only a small fraction of the total mass is contained within galaxies themselves, while the ICM constitutes the dominant baryonic component of the system (Lin and Mohr, 2004; Gonzalez et al., 2007).

The deep gravitational potential wells of clusters give rise to large galaxy velocity dispersions, typically of order 500–1000 km s^{-1} (Binney and Tremaine, 2008). These high relative velocities reduce the probability of galaxy mergers compared to lower-density environments such as galaxy groups (Ostriker, 1980; Makino and Hut, 1997). Instead, galaxies in clusters more frequently experience rapid encounters and tidal perturbations produced by interactions with other galaxies and with the global cluster potential (Moore et al., 1996; Moore et al., 1998).

Galaxy clusters grow hierarchically through the accretion of galaxies and galaxy groups along the filaments of the cosmic web. As galaxies fall into the cluster potential, they encounter increasingly dense intracluster gas and stronger tidal fields. Mergers between clusters and infalling groups can strongly disturb the ICM, generating shocks, cold fronts, and large-scale asymmetries in the gas distribution (Markevitch and Vikhlinin, 2007).

A well-known example of such a system is the Bullet Cluster (see Fig. 2.1), where X-ray observations reveal a highly disturbed ICM produced by the collision of two galaxy clusters (Clowe et al., 2006). This system illustrates how cluster mergers can dramatically reshape the distribution of the hot intracluster gas and produce complex dynamical states.

The physical conditions present in galaxy clusters therefore create an environment where several processes can influence the evolution of galaxies. Interactions with other galaxies, the cluster gravitational potential, and the surrounding ICM can significantly affect galaxy structure and gas content.

2.3 Evolutionary mechanisms

The physical conditions present in dense environments give rise to a variety of processes that can influence the evolution of galaxies. In this section we describe the main processes that operate in dense environments, focusing on gravitational interactions, hydrodynamical effects, and feedback driven by active galactic nuclei (AGN).

Gravitational interactions

Gravitational interactions represent one of the primary channels through which galaxy evolution is influenced by the surrounding environment. In dense environments such as galaxy groups and clusters, galaxies are subject not only to encounters with neighboring galaxies but also to the large-scale gravitational potential of the cluster itself.

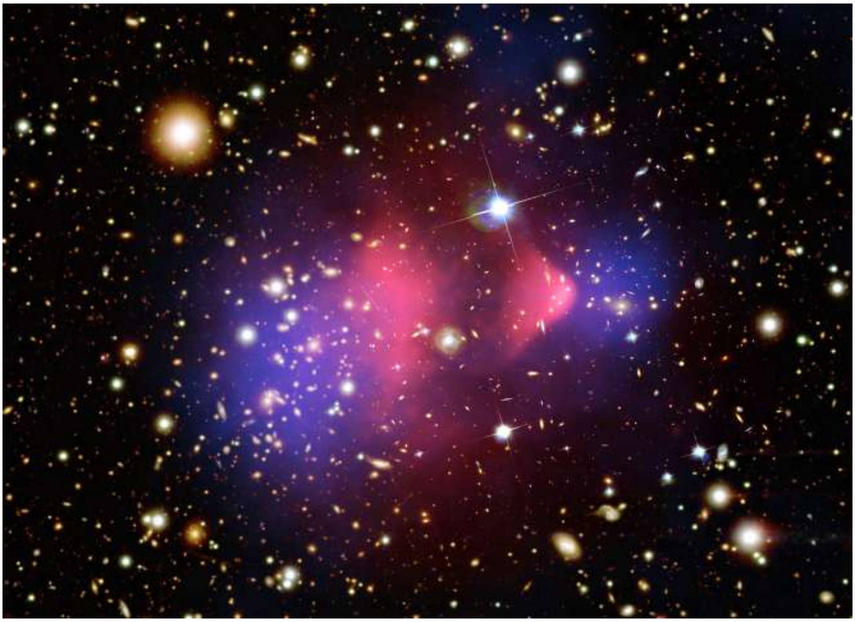

Figure 2.1: Composite image of the Bullet Cluster. The hot intracluster gas traced by X-ray emission is shown in red, while the total mass distribution inferred from gravitational lensing is shown in blue. The background optical image shows the galaxies in the cluster. The spatial separation between the X-ray emitting gas and the dominant mass component provides strong evidence that the system is the result of a collision between two galaxy clusters (Clowe et al., 2006). Image credit: X-ray: NASA/CXC/CfA/M. Markevitch; Optical and lensing map: NASA/STScI, Magellan/U. Arizona/D. Clowe; Lensing map: ESO WFI.

These interactions can perturb galactic disks, redistribute stars and gas, and produce a variety of morphological signatures including tidal tails, bridges, and stellar streams. The cumulative effect of such interactions can significantly alter galaxy structure and star formation activity. In the following sections, we discuss the main gravitational processes.

Galaxy–galaxy tidal interactions

Gravitational encounters between galaxies generate tidal forces that can perturb both their stellar and gaseous components. During close passages, the gravitational forces exerted by a companion galaxy can distort galactic disks and produce features such as tidal bridges, tails, and stellar streams. These disturbances primarily affect the outer regions of galactic disks, where gravitational binding is weaker and stars and gas can be more easily displaced.

Early numerical simulations demonstrated that many of the peculiar structures observed in galaxies can arise naturally from gravitational encounters alone. Using restricted three-body calculations, A. Toomre and J. Toomre (1972) showed that the tidal forces generated during a close passage between disk galaxies can strongly distort an initially circular stellar disk. As illustrated in Fig. 2.2, the interaction produces a tidal bridge extending toward the perturbing companion and a counter tail forming on the opposite side of the galaxy. Together, these structures generate the characteristic S-shaped morphology commonly observed in tidally interacting systems.

Tidal encounters can therefore produce significant distortions in galactic structure even when the interacting galaxies do not merge. Repeated interactions of this kind can redistribute stars and gas within galaxies and contribute to the gradual morphological evolution of galaxies.

Galaxy mergers

Galaxy mergers represent the most extreme outcome of galaxy–galaxy interactions. In these events, interacting galaxies lose orbital energy through dynamical friction and eventually form a single remnant galaxy (Binney and Tremaine, 2008). During the merger, tidal forces can remove stars and gas from the galactic disks, forming extended streams and tidal tails. An example of three merging galaxies is shown in Fig. 2.3.

Galaxy mergers are commonly classified according to the mass ratio of the interacting galaxies (Burkert and Naab, 2003). Major mergers occur when galaxies of comparable mass interact and typically produce strong tidal distortions and large-scale structural transformation. Such interactions can completely disrupt stellar disks and lead to the formation of spheroidal remnants, providing one pathway for the transformation of spiral galaxies into elliptical systems. Minor mergers involve a massive galaxy interacting with a significantly smaller companion and generally produce weaker disturbances. In these cases the primary galaxy often retains its disk structure, although the interaction can contribute to the growth of the bulge and stellar halo.

Numerical simulations have shown that mergers can redistribute angular momentum within galaxies and drive gas toward their central regions (Barnes and L. E.

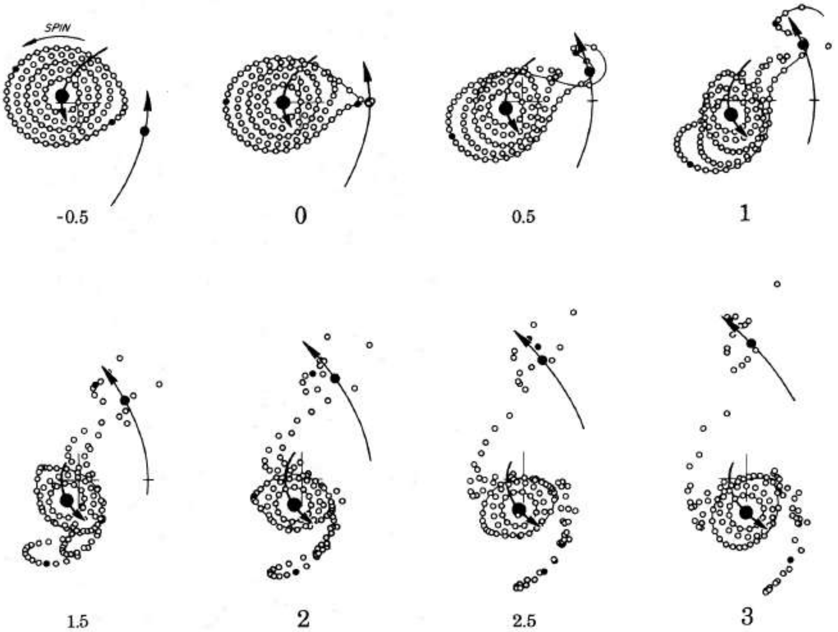

Figure 2.2: Three-body simulation of a tidal encounter between two disk galaxies from A. Toomre and J. Toomre (1972). The panels illustrate successive stages of the interaction as a companion galaxy passes a rotating stellar disk. Tidal forces distort the initially circular stellar distribution, producing a bridge toward the perturbing galaxy and a counter tail on the opposite side of the disk. As the interaction progresses, these features become more pronounced, giving rise to the characteristic S-shaped morphology commonly observed in tidally interacting galaxies.

Hernquist, 1991; Mihos and L. Hernquist, 1996). This inflow of gas can trigger very intense episodes of star formation, commonly referred to as starbursts, in which the star formation rate increases dramatically over a relatively short period of time. As the merger progresses, the stellar disks become increasingly disrupted and the final remnant may resemble a spheroidal system (Barnes and L. Hernquist, 1992). In this configuration the stellar motions become largely random and the system becomes supported primarily by velocity dispersion rather than ordered rotation, consistent with the properties of elliptical galaxies mentioned in Chapter 1 (R. L. Davies et al., 1983). In addition, the rapid consumption of gas during the starburst can significantly deplete the cold gas reservoir (Tacconi et al., 2008), leaving the remnant with little

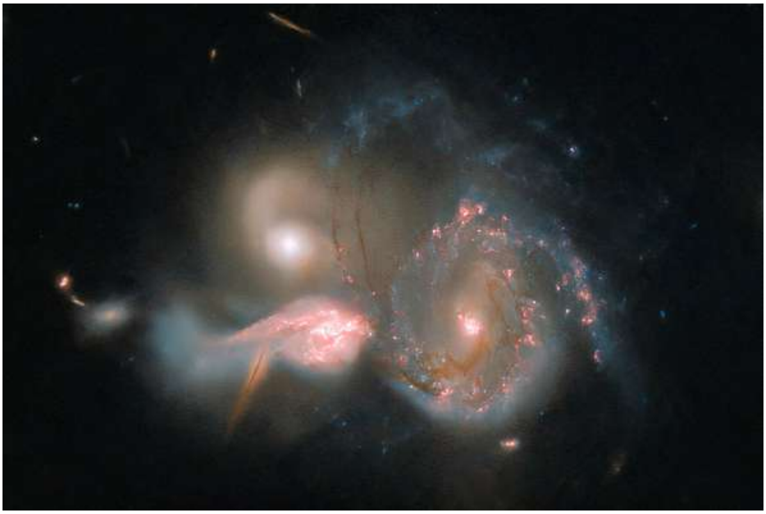

Figure 2.3: Hubble Space Telescope image of the interacting galaxy system Arp 273. The system shows three galaxies in the process of merging. We can observe pronounced tidal distortions and disrupted spiral structure, streams of stars and gas are pulled from the disks as tidal forces redistribute material throughout the system. Image credit: NASA, ESA, and the Hubble Heritage Team (STScI/AURA).

fuel for further star formation.

Because mergers require relatively long interaction times, they occur most frequently in galaxy groups where velocity dispersions are lower and galaxies can remain gravitationally bound for extended periods. In contrast, the much higher relative velocities found in galaxy clusters make such mergers less common.

Tidal interactions with the cluster potential

In addition to encounters with other galaxies, systems residing in clusters are also affected by the global gravitational potential of the cluster itself. As galaxies orbit within the cluster, the strong tidal field generated by the overall mass distribution can perturb their components. These tidal forces can strip material from the outer regions of galaxies, remove loosely bound stars and gas, and gradually heat stellar disks, leading to thicker and more dynamically disturbed systems (Merritt, 1983; Byrd and Valtonen, 1990). Tidal effects are expected to be strongest near the cluster center, where the gravitational potential gradient is largest. Over time, repeated passages through the cluster potential can therefore contribute to the gradual structural transformation of galaxies.

Galaxy harassment

Galaxies moving through cluster environments may undergo numerous rapid encounters with other cluster members. These high-velocity interactions can occur repeatedly as galaxies orbit within the cluster potential, producing a cumulative effect known as galaxy harassment (Moore et al., 1996).

Because galaxy velocities in clusters are typically very large, close encounters generally occur on short timescales and rarely lead to mergers. Nevertheless, repeated gravitational perturbations can gradually heat stellar disks, remove loosely bound material from the outer regions of galaxies, and induce structural distortions. Numerical simulations have shown that these cumulative interactions can significantly modify galaxy morphology, particularly for low-mass disk galaxies, which may be transformed into spheroidal systems over time (Moore et al., 1996; Moore et al., 1998).

Hydrodynamical processes

Interactions between galaxies and the surrounding ICM can also play an important role in shaping galaxy evolution in dense environments. As galaxies move through the hot intracluster gas, hydrodynamical forces can remove gas from their disks or alter its distribution within the galaxy. These processes primarily affect the gaseous component of galaxies and can therefore strongly influence the availability of cold gas and the subsequent star formation activity. While early theoretical work provided analytic descriptions of these mechanisms, their complex gas dynamics have been explored in greater detail through numerical hydrodynamical simulations, which have helped to clarify how gas is removed and redistributed within cluster galaxies. The main mechanisms operating in this context include ram pressure stripping, viscous stripping, thermal evaporation, and strangulation.

Ram pressure stripping

Ram pressure stripping (RPS) occurs when a galaxy moves through the ICM, thus experiencing a wind produced by its motion relative to the surrounding hot gas. This interaction exerts a pressure on the interstellar medium (ISM) of the galaxy which can remove gas from the disk. A simple formalism that quantifies this pressure was introduced by Gunn and Gott (1972), where ram pressure is given by

$$P_{\rm ram} \approx \rho_{\rm e} v^2, \tag{2.1}$$

where $\rho_{\rm e}$ is the density of the surrounding medium and v is the velocity of the galaxy relative to it. This relation implies that galaxies moving rapidly through a dense medium experience stronger ram pressure than galaxies moving slowly or through a lower-density environment.

RPS becomes effective when the ram pressure exerted by the ICM exceeds the gravitational restoring force that binds the gas to the galactic disk. This condition can be expressed as

$$\rho_{\rm e} v^2 \gtrsim 2\pi G \Sigma_\star \Sigma_{\rm gas}, \tag{2.2}$$

where $\Sigma_\star$ and $\Sigma_{\rm gas}$ are the stellar and gas surface densities of the disk, respectively. When this condition is satisfied, the external ram pressure can overcome the gravitational restoring force of the disk and displace gas from the galaxy. This expression provides a simplified description of the stripping process, as the effectiveness of RPS also depends on additional factors such as the inclination of the galaxy relative to its direction of motion, the structure of the ISM, and the orbital path of the galaxy within the cluster. Because the outer regions of galactic disks are typically more weakly bound, stripping often begins in the outskirts and may progress inward as the galaxy moves deeper into the cluster potential or encounters denser regions of the ICM. The stellar component, however, is generally expected to remain largely unaffected by RPS (albeit not entirely, see Smith et al., 2012) due to its stronger gravitational binding within the galaxy.

Observationally, RPS can produce a variety of signatures, including truncated gas disks, asymmetric gas distributions, and extended tails of stripped material trailing behind galaxies as they move through the cluster environment. Early observational hints of gas removal were already inferred from optical morphologies and dust distributions by Gallagher (1978). Subsequent interferometric studies by Warmels (1988) and Cayatte et al. (1990) provided some of the first strong observational indications of galaxies affected by RPS. Later works by Gavazzi et al. (1995) and Chung et al. (2009) revealed direct evidence of ongoing stripping of the neutral gas, with galaxies displaying prominent one-sided gaseous tails, leading to the discovery of the so-called jellyfish galaxies (see Fig. 2.4).

In the most extreme cases, the stripped gas can condense within the tails and form stars in situ outside the main body of the galaxy (Gavazzi et al., 1995; Gullieuszik et al., 2023). These star-forming knots are commonly observed in optical and Hα emission and indicate that the stripped material can remain sufficiently dense to collapse and form new stellar populations. Star formation can also be triggered within the disk itself due to the compression of the ISM by the ram-pressure wind, producing bright Hα regions at the leading edge of the galaxy, as illustrated in the left panel of Fig. 2.4 for GCG 97−073. Galaxies exhibiting extended gaseous tails with embedded star-forming regions are commonly referred to as jellyfish galaxies, an example of which is shown in the right panel of Fig. 2.4 for the GASP galaxy JO206. Integral-field spectroscopic surveys, such as the GASP survey (Poggianti et al., 2017), which is based on the sample of stripping candidates presented in Poggianti et al. (2016), have revealed numerous examples of these systems and have enabled detailed studies of the gas kinematics and star formation occurring within the stripped tails.

Another morphological feature that has been associated with some jellyfish galaxies is the apparent unwinding of their spiral arms. This phenomenon was first reported in the jellyfish galaxy JO201 by Bellhouse et al. (2017). The unwinding appears as spiral arms that become stretched and displaced in the direction opposite to the galaxy motion through the ICM, suggesting that the outer disk structure may be affected by the stripping process. However, this feature has been observed in only a subset of confirmed jellyfish galaxies and may also arise from other mechanisms, such as gravitational interactions or tidal perturbations. Whether spiral arm unwinding can be produced exclusively by RPS therefore remains a subject of ongoing debate. More recently, Vulcani et al. (2022) identified a complementary sample of galaxies displaying similar optical features in the same clusters studied by Poggianti et al. (2016). Based on this work, the fraction of optical jellyfish galaxies is estimated to be approximately $\sim 15\%$ of the blue, non-interacting cluster population, increasing to $\sim 35\%$ if all galaxies exhibiting unwinding features are included.

The location of galaxies within clusters also provides important clues about the physical conditions under which RPS occurs. In particular, projected phase-space diagrams, which combine cluster-centric distance and line-of-sight velocity, have become a useful tool for identifying galaxies that are likely experiencing strong environmental effects. In these diagrams, galaxy velocities are typically normalized by the cluster velocity dispersion and distances by the virial radius R_{200}. Galaxies undergoing RPS are often found along regions of phase space associated with recent infall into the cluster potential, where relative velocities and ICM densities are suf-

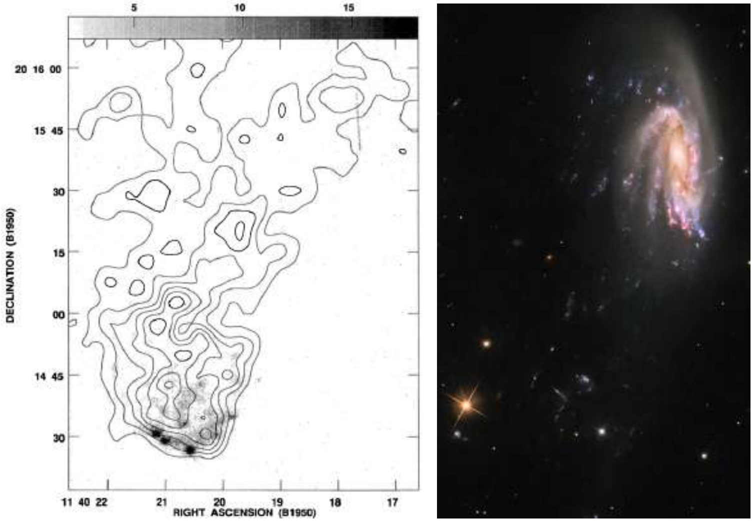

Figure 2.4: Examples of jellyfish galaxies undergoing ram pressure stripping. The left panel shows radio continuum contours superposed on grayscale Hα emission of the jellyfish galaxy GCG 97−073 from Gavazzi et al. (1995). The right panel shows broad-band optical emission from the jellyfish galaxy JO206 from the GASP survey (Poggianti et al. 2016; image credit: ESO/GASP collaboration). Galaxies displaying such one-sided tails are commonly referred to as jellyfish galaxies.

ficiently high to produce efficient gas removal (e.g. Jaffé et al., 2015; J. Rhee et al., 2017). As illustrated in Fig. 2.5, these regions correspond to galaxies moving at high velocities relative to the cluster and located at intermediate cluster-centric distances. In many cases the orientation of the stripped tails provides additional information about the direction of motion of the galaxy through the ICM, with the tails often pointing radially away from the cluster center (e.g. Chung et al., 2009; Smith et al., 2022; Salinas et al., 2024).

Viscous stripping

Gas can also be removed from galaxies through viscous interactions between the ISM of the galaxy and the surrounding intracluster gas. As a galaxy moves through the cluster medium, velocity shear develops at the interface between the ISM and the external gas. Viscous and turbulent transport processes across this boundary can

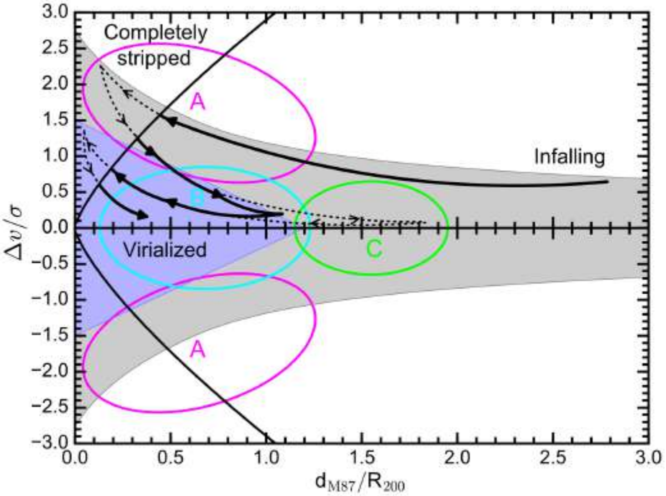

Figure 2.5: Schematic phase–space diagram illustrating the orbital evolution of galaxies in a cluster environment. The projected cluster-centric distance is normalized by the virial radius R_{200}, and the line-of-sight velocity is normalized by the cluster velocity dispersion σ. The gray region indicates the extent of the cluster potential, while the blue shaded region marks the virialized population. The arrows trace the typical orbit of an infalling galaxy. Galaxies enter the cluster at large radii and accelerate toward the cluster center, reaching the region where ram pressure stripping is the most effective (region A). After passing pericenter, galaxies move back toward larger radii while decreasing in velocity, eventually populating regions of low velocity at large cluster-centric distances (region C), often referred to as backsplash systems. As they lose energy through successive orbits, galaxies settle into the virialized region (region B). Figure from Yoon et al. (2017).

transfer momentum from the surrounding medium to the galactic gas, gradually removing material from the outer layers of the disk (Nulsen, 1982). Hydrodynamical instabilities, such as Kelvin–Helmholtz instabilities, may also develop at this interface and contribute to the stripping of gas.

Unlike RPS, which can remove gas rapidly once the condition in Eq. 2.2 is satisfied, viscous stripping operates as a more continuous process in which gas is steadily removed through transport processes and turbulent mixing at the ISM–ICM interface. The efficiency of this mechanism depends on several factors, including the relative velocity of the galaxy, the density contrast between the ISM and the surrounding medium, and the effective viscosity of the hot gas.

Although viscous stripping is generally expected to be less efficient than RPS in massive clusters, it may contribute to the gradual removal of gas from galaxies as they move through the cluster environment.

Thermal evaporation

Thermal conduction between the hot ICM and the colder ISM of galaxies can also lead to gas loss. If heat is efficiently conducted across the ISM–ICM interface, the temperature difference between the two media can cause cold gas clouds to evaporate into the surrounding hot plasma (Cowie and McKee, 1977; Cowie and Songaila, 1977).

The evaporation rate depends strongly on the temperature of the surrounding medium and on the efficiency of thermal conduction. In practice, the effectiveness of this mechanism may be reduced if magnetic fields suppress thermal conduction in the intracluster gas. Nevertheless, thermal evaporation may contribute to the gradual removal of cold gas from galaxies residing in dense environments.

Starvation

Another process that can influence galaxy evolution in dense environments is starvation. In this scenario, the extended gaseous halo surrounding a galaxy is removed or disrupted as the galaxy enters a dense medium such as a galaxy group or cluster. Because this halo gas normally acts as a reservoir that can cool and replenish the cold gas within the disk, its removal prevents the galaxy from accreting new material.

Physically, this mechanism is also a hydrodynamical interaction with the surrounding medium. In practice, it can be understood as a mild form of RPS that primarily affects the diffuse halo gas rather than the cold gas within the disk. Because the halo gas is only weakly bound to the galaxy, even relatively modest interactions with the surrounding ICM can remove it.

Once the supply of fresh gas is halted, the galaxy can no longer replenish the cold gas consumed by star formation. The remaining gas in the disk is therefore gradually depleted as star formation continues, leading to a progressive decline in star formation activity. This idea was originally proposed by Larson et al. (1980), who suggested that galaxies entering dense environments may cease accreting gas from their surroundings, causing star formation to decline as the existing gas reservoir in the disk is exhausted.

Active galactic nuclei

Galaxy evolution is influenced not only by external environmental effects, but also by internal processes operating within galaxies themselves. One of the most important of these is feedback driven by active galactic nuclei (AGN). AGN are powered by the accretion of matter onto supermassive black holes (SMBHs) located at the centers of most galaxies, and can release large amounts of energy in the form of radiation, winds, and relativistic jets. This energy can couple to the surrounding ISM and, in some cases, heat or expel gas from the host galaxy. AGN activity is therefore commonly invoked as a mechanism capable of regulating star formation and influencing the evolution of massive galaxies (Kormendy and Ho, 2013; Heckman and Best, 2014).

The following subsections briefly introduce the physical origin of AGN activity, describe the unified model that explains the main observational classes of AGN, and discuss the principal forms of AGN-driven feedback.

Supermassive black holes

SMBHs are observed at the centers of most massive galaxies in the local Universe, with masses ranging from 10^6 to $10^{10}\,M_\odot$. Dynamical measurements indicate that most galaxies hosting classical bulges contain central SMBHs, and observations reveal strong correlations between SMBH mass and properties of the host galaxy bulge, such as the stellar velocity dispersion. These correlations suggest a close connection between the growth of SMBHs and the evolution of their host galaxies (Kormendy and Ho, 2013).

In the Milky Way, precise measurements of stellar orbits around the compact radio source Sagittarius A* have revealed the presence of a central black hole with a mass of approximately $4 \times 10^6\,M_\odot$ (Ghez et al., 2008). More recently, very-long-baseline interferometry (VLBI) observations by the Event Horizon Telescope (EHT) have provided the first direct images of the immediate surroundings of an SMBH.

When gas accretes onto these black holes, gravitational energy can be efficiently converted into radiation, producing the phenomenon known as an AGN (Lynden-Bell, 1969). These span a wide range of luminosities and observational manifestations. They can outshine the entire stellar population of their host galaxies and are observed across the electromagnetic spectrum, from radio to X-rays and γ-rays (Padovani et al., 2017). Historically, several classes of AGN have been identified, including Seyfert galaxies, quasars (quasi-stellar objects, QSOs), radio galaxies, and blazars. Although these objects display diverse observational properties, they are generally understood to arise from the same basic physical mechanism: accretion of material onto an SMBH. Differences between the observed classes are largely attributed to factors such as viewing angle, accretion rate, and the presence of relativistic jets (R. Antonucci, 1993; Urry and Padovani, 1995).

The unified model and classification of AGN

Although AGN exhibit a wide range of observational properties, many of these differences can be understood within the framework of the unified model. In this picture, the various classes of AGN arise primarily from orientation effects relative to the observer's line of sight (Urry and Padovani, 1995). A schematic representation of this model is shown in Fig. 2.6. The basic structure of an AGN consists of an SMBH surrounded by an accretion disk that emits strong thermal emission across the electromagnetic spectrum. Close to the disk lies the broad-line region (BLR), composed of rapidly moving gas clouds that produce Doppler-broadened emission lines. On larger scales, the narrow-line region (NLR) contains lower-density gas that produces narrower emission lines.

Surrounding the central region is a geometrically thick, dusty torus that can obscure the inner structures depending on the viewing angle. When the central engine is viewed directly, both the accretion disk and the BLR are visible, producing what are typically classified as Type 1 AGN. If the torus obscures the line of sight to the BLR, only the NLR is observed, resulting in Type 2 AGN (Khachikian and Weedman, 1974; R. R. J. Antonucci and Miller, 1985). These systems are typically radiatively efficient, with emission dominated by the accretion disk. They include Seyfert galaxies and QSOs, with QSOs representing the high-luminosity end of this population (Schmidt, 1963; Padovani et al., 2017). Seyfert galaxies are typically hosted in spiral galaxies and represent the low-luminosity end of this class (Ho et al., 1997). Both Seyferts and QSOs can be observed as either Type 1 or Type 2 depending on orientation. NGC 3281, the focus of this licentiate thesis, is a Seyfert 2 galaxy (i.e. an example of a Type 2 AGN in the low-luminosity regime).

In some systems, relativistic jets emerge perpendicular to the accretion disk and can extend well beyond the host galaxy (Blandford and Znajek, 1977; Blandford and Rees, 1978). When these jets are oriented close to the line of sight, strong relativistic beaming can dominate the observed emission, producing objects such as blazars. When viewed at larger angles, these same systems are observed as radio galaxies (Urry and Padovani, 1995). AGN that produce powerful jets are often referred to

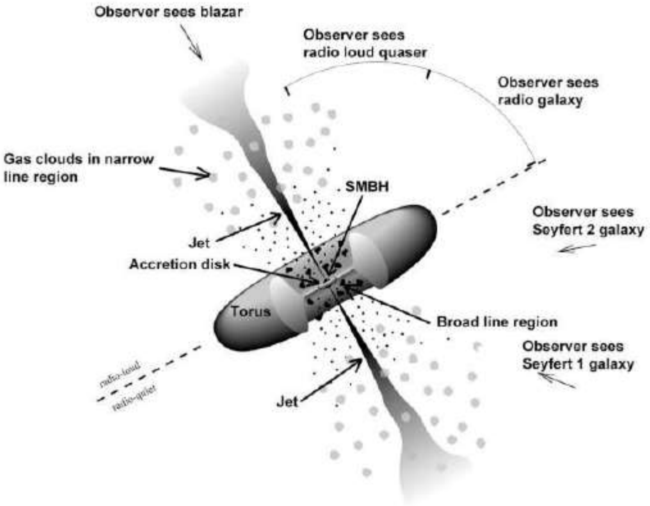

Figure 2.6: Schematic illustration of the unified model of active galactic nuclei. A central SMBH is surrounded by an accretion disk and a broad-line region, embedded within an obscuring dusty torus. Narrow-line emission arises on larger scales, while relativistic jets emerge perpendicular to the disk. The observed classification of AGN depends primarily on the viewing angle relative to the torus and jet axis, producing different observational classes such as Seyfert galaxies, radio galaxies, QSOs, and blazars (Urry and Padovani, 1995).

as radio-loud, in contrast to radio-quiet systems where such jets are weak or absent (Kellermann et al., 1989). In radio-loud AGN, these jets can form large-scale radio structures and are classified as Fanaroff–Riley type I (FR I) and type II (FR II) sources based on their morphology and luminosity (Fanaroff and Riley, 1974). FR I sources have jets that fade with distance from the nucleus, while FR II sources show bright hotspots at the lobe edges. These systems are typically hosted by massive ellipticals and are rare in spirals. Despite this, radio-loud AGN are important in clusters, as their jets transport energy into the ISM and ICM and can affect gas cooling and galaxy evolution.

This combined framework shows that the diversity of AGN properties arises not only from orientation, but also from intrinsic differences in accretion rate and jet production. Orientation determines whether the BLR is visible (Type 1 vs Type 2), while accretion mode and jet power distinguish between radiative systems such as

Seyferts and QSOs, and jet-dominated radio galaxies such as FR I and FR II sources.

AGN-driven feedback and outflows

Accretion onto SMBHs releases large amounts of energy that can interact with the surrounding gas in the host galaxy (Lynden-Bell, 1969). Part of this energy is radiated across the electromagnetic spectrum, while another fraction can be transferred mechanically through winds, outflows, or relativistic jets (Fabian, 2012). These processes can alter the physical state and distribution of gas within galaxies and are commonly referred to as AGN feedback.

In some AGN, part of the accretion energy is released in the form of highly collimated relativistic jets that emerge perpendicular to the accretion disk (Blandford and Znajek, 1977; Blandford and Rees, 1978). The emission from these structures is typically dominated by synchrotron radiation produced by relativistic electrons spiraling in magnetic fields, making them particularly prominent at radio wavelengths (Rybicki and Lightman, 1979). These jets can propagate far beyond the host galaxy, transporting energy into the surrounding ISM and ICM (Fabian, 2012).

AGN can also drive less collimated gaseous outflows originating from the accretion disk or the nuclear region of the galaxy (Veilleux et al., 2005; King and Pounds, 2015). These outflows are commonly detected through broad emission or absorption lines in optical, ultraviolet, and X-ray spectra, and may also contain molecular gas observable at millimeter wavelengths (Crenshaw et al., 2003; Feruglio et al., 2010; Tombesi et al., 2010). Unlike relativistic jets, these winds interact more directly with the ISM of the host galaxy and can redistribute or remove gas from the central regions (e.g. Veilleux et al., 2005).

A well-known nearby example of an AGN launching bipolar outflows is the radio galaxy Centaurus A (NGC 5128), shown in Fig. 2.7. This galaxy hosts an active nucleus powered by accretion onto a central SMBH, producing jets and outflows that extend far beyond the galactic disk.

As these outflows propagate away from the nucleus, they interact with the surrounding gas in the host galaxy and, in some cases, with the larger-scale environment. Jets can inject energy into the surrounding medium and inflate cavities in the hot gas of galaxy groups and clusters, while wide-angle winds can drive multiphase outflows capable of removing or heating the ISM. Through these interactions, AGN are able to transfer significant amounts of energy and momentum to their surroundings, regulating gas cooling in galaxy groups and clusters (Croston et al., 2005; Fabian, 2012), and potentially suppressing star formation in their host galaxies (Silk

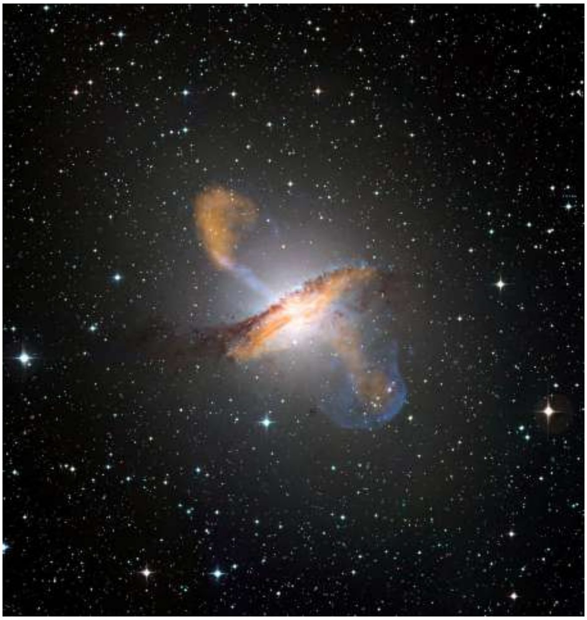

Figure 2.7: Multiwavelength composite image of the nearby radio galaxy Centaurus A (NGC 5128), revealing jets and lobes produced by the active galactic nucleus powered by accretion onto a central SMBH. The optical emission (stars and dust lane) is shown using data from the Wide Field Imager (WFI) on the MPG/ESO 2.2 m telescope, while submillimetre emission at 870 μm from LABOCA on APEX is shown in orange and X-ray emission from the *Chandra* X-ray Observatory is shown in blue. Image credit: ESO/WFI (Optical); MPIfR/ESO/APEX/A. Weiss et al. (Submillimetre); NASA/CXC/CfA/R. Kraft et al. (X-ray).

and Rees, 1998).

2.4 Gas removal and star formation quenching

A key feature shared by many of the environmental mechanisms described in the previous sections is their ability to alter the gas reservoirs of galaxies. Processes such as tidal interactions, RPS, and AGN-driven outflows can remove, redistribute, or heat the gaseous component of a galaxy. Because cold gas provides the fuel for star formation, modifications to this gas reservoir can lead to a decline in star formation activity and eventually to the quenching of the galaxy. Therefore, understanding how all of these processes affect the gas content of galaxies is essential for interpreting the full picture of galaxy transformation.

Once star formation is quenched, the stellar population evolves passively, with the young, blue stars fading on relatively short timescales, causing the galaxy to become progressively redder and fainter. This process is not spatially uniform, particularly for environmental mechanisms such as RPS, where the outer regions are affected first, leading to truncated star-forming disks. As stellar populations age and the disk fades, spiral features become less prominent and the system appears smoother and more centrally concentrated. In this context, Marasco et al., 2023 show that, following quenching, the fading of the stellar disk leads to the disappearance of spiral structure and a redistribution of light toward the central regions, resulting in a transformation from blue, star-forming spirals to redder, more passive systems on timescales of $\sim$1–3.5 Gyr.

Figure 2.8 shows the fraction of red (quenched) galaxies as a function of stellar mass and local overdensity using data from the Sloan Digital Sky Survey (Peng et al., 2010). The diagram demonstrates that galaxy quenching depends on both stellar mass and environment: massive galaxies exhibit a high quenched fraction largely independent of environment, while increasing environmental density further enhances the quenched fraction. This indicates that galaxies can become quenched through internal, mass-dependent processes even in relatively low-density environments, while environmental effects provide an additional channel for quenching in denser regions.

Internal mechanisms associated with massive galaxies, such as feedback from AGN, are thought to play a key role in regulating star formation in the most massive systems. At the same time, environmental processes become increasingly important as galaxies move into denser regions, where interactions with the ICM and with other galaxies can further modify their gas reservoirs.

The connection between environmental processes and AGN activity is not straightforward. Gravitational interactions, such as tidal encounters and mergers, can drive gas inflows toward the central SMBH and are therefore considered an efficient mechanism for triggering AGN activity (e.g. Shlosman et al., 1989; Hopkins and Quataert, 2010). As a result, AGN may be preferentially associated with galaxies that have undergone pre-processing in group environments prior to cluster infall. In contrast, the effect of RPS on AGN activity remains less clear. While the removal of gas can limit the fuel available for accretion, some studies suggest that RPS may temporarily enhance accretion during the peak of the stripping process (Poggianti et al., 2017;

Peluso et al., 2022). Observationally, AGN in clusters are often found in regions of phase space associated with recently infalling galaxies, where both gas-rich conditions and strong environmental interactions are present (Haines et al., 2012; Maier et al., 2022). This highlights that AGN activity itself may be influenced by the same environmental processes that regulate the gas content of galaxies.

Rather than being driven by a single dominant mechanism, galaxy evolution is therefore more accurately described as the result of multiple processes acting together. Both observations and simulations indicate that these mechanisms rarely act in isolation, but instead operate simultaneously and can influence each other. For example, tidal interactions can weaken the gravitational potential of a galaxy, making its gas more susceptible to removal by RPS (Mayer et al., 2006). Similarly, observational studies have found systems in which signatures of gravitational interactions coexist with one-sided HI tails characteristic of RPS, suggesting that both processes are acting together (e.g. Oosterloo and J. van Gorkom, 2005; Kleiner et al., 2021; Serra et al., 2023). In some cases, tidal effects may even be a necessary step for RPS to efficiently displace the gas (Serra et al., 2023). As a result, disentangling the relative importance of individual mechanisms is often challenging, since their combined action can produce complex and overlapping observational signatures (Smith et al., 2025).

Because many of these processes primarily affect the gaseous component of galaxies, observations of cold gas provide one of the most direct ways to trace environmental transformation. Among the different phases of the ISM, neutral atomic hydrogen (H I) is particularly important in this context. The H I component of galaxies often extends well beyond the stellar disk and is therefore especially sensitive to environmental interactions such as tidal forces and RPS. As a result, H I observations provide a powerful tool for identifying and characterizing the processes responsible for gas removal and the subsequent quenching of star formation in cluster galaxies.

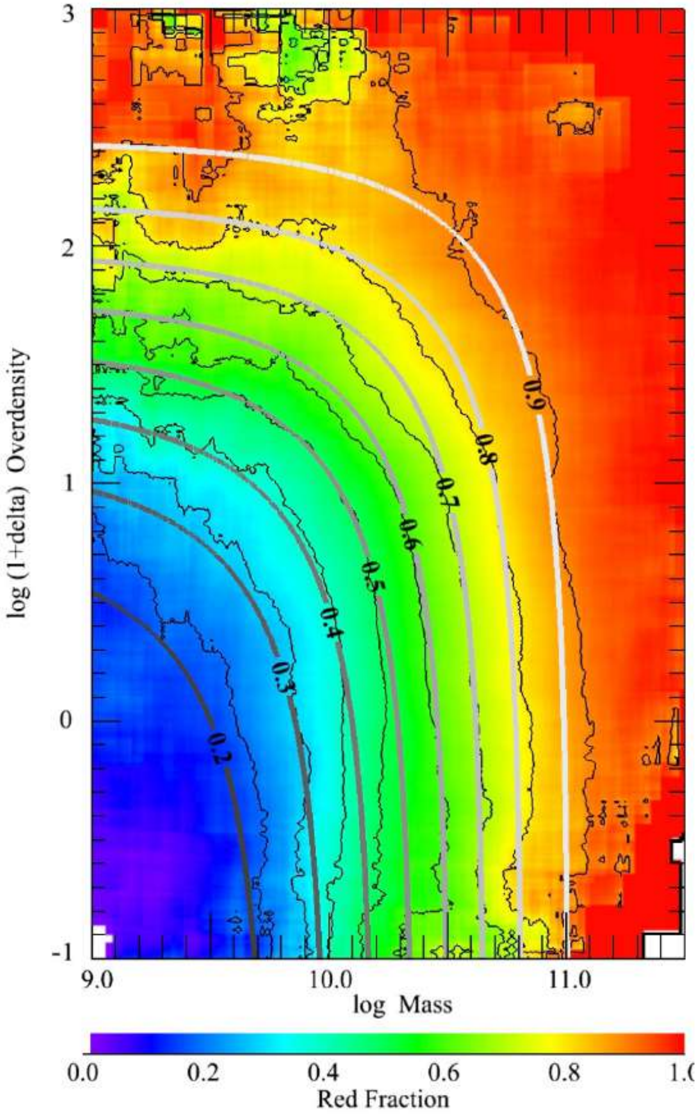

Figure 2.8: Fraction of red (quenched) galaxies in the Sloan Digital Sky Survey (SDSS) as a function of stellar mass and environmental overdensity. The color scale indicates the fraction of galaxies that are quiescent. The diagram shows that the probability of a galaxy being quenched increases with both stellar mass and environmental density, illustrating the combined roles of mass-dependent and environmental processes in galaxy evolution (Peng et al., 2010).

CHAPTER 3

Neutral Hydrogen in Galaxies

3.1 Gas in galaxies

As discussed in the previous chapter, the gas component of galaxies plays a central role in their evolution. The ISM is composed of multiple phases spanning a wide range of temperatures and densities, distributed across different regions of the galaxy and tracing different physical conditions and processes.

The ISM can be broadly divided into different phases according to temperature. The hot ionized medium (HIM), with temperatures of $T \sim 10^5$–10^7 K, is typically found in galactic halos and is often associated with feedback processes such as supernova explosions and AGN activity. At intermediate temperatures, the warm ionized medium (WIM) and warm neutral medium (WNM), with $T \sim 10^4$ K, trace diffuse gas distributed throughout the disk and halo (McKee and Ostriker, 1977).

At lower temperatures, the cold neutral medium (CNM) has $T \sim 10^2, \mathrm{K}$ and is predominantly composed of neutral atomic hydrogen (H I). It also contains helium, trace metals, and dust. Molecular gas forms a distinct, denser phase of the ISM with temperatures below $\sim 50, \mathrm{K}$. Molecular gas, primarily in the form of H_2, is directly associated with star-forming regions. Since H_2 does not emit efficiently at the low temperatures typical of molecular clouds, it is commonly traced through emission from carbon monoxide (CO; Bolatto et al. 2013). CO traces the molecular gas because both CO and H_2 are confined to UV-shielded regions of the ISM, with CO surviving in the dense interiors of molecular clouds where H_2 is abundant.

The evolution of cold gas in galaxies is therefore governed by the conversion of atomic hydrogen into molecular gas, which subsequently forms stars (Krumholz et al., 2008; Krumholz et al., 2009). The cold neutral gas acts as a reservoir from which molecular clouds can form. On global (galaxy-integrated) scales, this distinction is reflected in the observed scaling relations shown in Fig. 3.1, where the molecular gas fraction exhibits a tighter correlation with specific star formation rate (sSFR) compared to the atomic gas component (Saintonge et al., 2017). At the same time, galaxies typically contain a larger reservoir of atomic hydrogen than molecular gas, indicating that H I serves as the long-term fuel supply that can be converted into molecular gas and sustain star formation over time (Walter et al., 2008; Saintonge et al., 2017).

On smaller (resolved) scales within galaxies, the transition from atomic to molecular gas is associated with characteristic column density thresholds, above which the gas becomes sufficiently self-shielded to allow the formation of molecular hydrogen (Schaye, 2004; Krumholz et al., 2008). This behavior is illustrated by the Kennicutt–Schmidt relation (Fig. 3.2), which links the surface density of gas to the surface density of star formation (Kennicutt, 1998), and reflects the connection between gas density and star formation activity.

The different phases of the ISM are also distributed differently within galaxies. The HIM is typically found in extended halos. The WIM and WNM trace diffuse gas distributed throughout both the disk and halo. Neutral atomic hydrogen (H I), which comprises both the CNM and WNM phases, is not limited to the stellar disk and often extends well beyond it, with H I diameters typically about 1.5–2 times larger than the optical diameter (Broeils and M.-H. Rhee, 1997). Within this component, the CNM is primarily associated with denser structures in the disk, where it is organized in clouds and filaments, while the WNM forms a more diffuse, extended medium (see Fig. 3.3). Molecular gas is concentrated in the densest regions of the disk, typically along spiral arms and in the inner parts of galaxies. This spatial distribution is illustrated in Fig. 3.4.

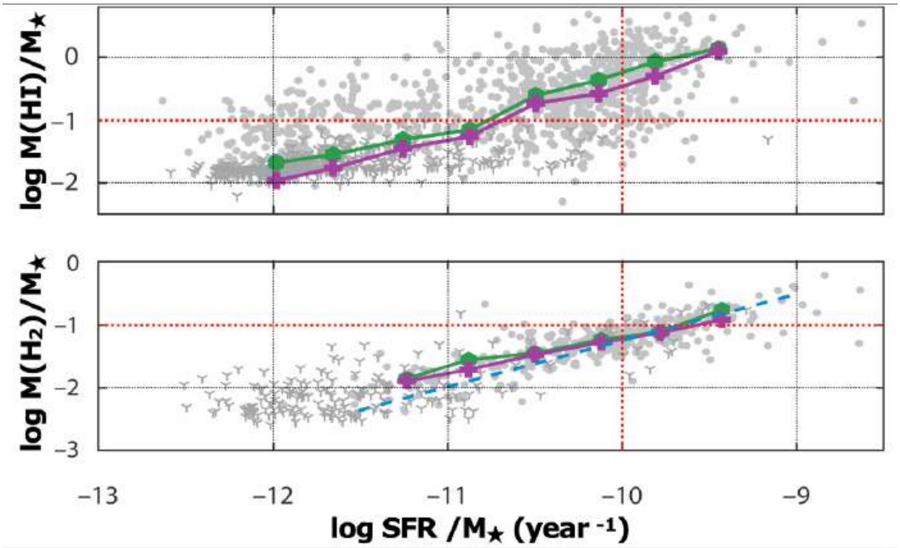

Figure 3.1: Gas fraction as a function of specific star formation rate (sSFR) for atomic hydrogen (top) and molecular gas (bottom). The molecular gas fraction shows a tighter correlation with sSFR, while atomic hydrogen exhibits a larger scatter and typically higher gas fractions. This reflects the role of H_2 as the immediate fuel for star formation and H I as a more extended gas reservoir. Adapted from Saintonge and Catinella (2022).

3.2 Neutral atomic hydrogen

While the molecular phase traces the immediate sites of star formation, hydrogen is the most abundant element in the Universe, and H I represents the phase through which gas transitions before becoming molecular, acting as the main fuel reservoir for star formation. The distribution and kinematics of H I are also highly sensitive to the evolutionary state of galaxies, retaining signatures of past interactions with their environment.

H I emission

H I is traced through the 21 cm hyperfine transition of neutral hydrogen, corresponding to a rest frequency of $\nu_{\rm HI} = 1420.405\,{\rm MHz}$. This transition arises from the spin-flip of the electron–proton system. The transition is highly forbidden, with a

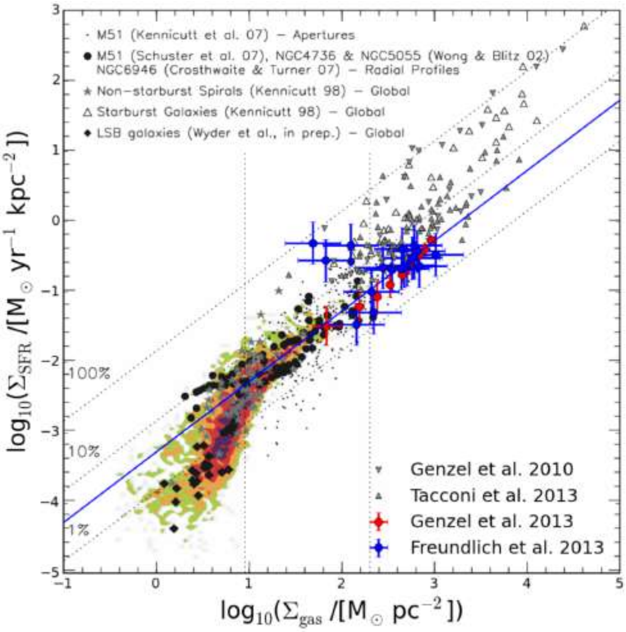

Figure 3.2: Kennicutt–Schmidt relation between gas surface density and star formation rate surface density for a compilation of galaxies spanning a wide range of environments and redshifts. The relation shows that higher gas surface densities are associated with higher star formation rate surface densities, reflecting the dependence of star formation on the local gas reservoir. The different symbols correspond to various samples, including nearby spirals, starburst galaxies, and high-redshift systems. Figure from Freundlich et al. (2014).

spontaneous decay rate of $A_{21} = 2.85 \times 10^{-15}\ \mathrm{s}^{-1}$, corresponding to a characteristic lifetime of $\sim 10^7$ years for an individual atom. As a result, the emission from a single hydrogen atom is extremely weak. However, galaxies contain an enormous number of hydrogen atoms. For a galaxy with an H I mass comparable to that of the Milky Way ($\sim 10^9\ M_\odot$), this corresponds to a total number of atoms of order $N_{\mathrm{H\,I,tot}} \sim 10^{65}$, so that the cumulative emission from many atoms produces a detectable signal.

When this emission is integrated over the spatial extent of a galaxy, it produces a spectrum as a function of radial velocity, $S(v)$, which contains information on both the gas content and the kinematics of the system. In disk galaxies, this spectrum is primarily shaped by rotation and typically shows a characteristic double-horn profile

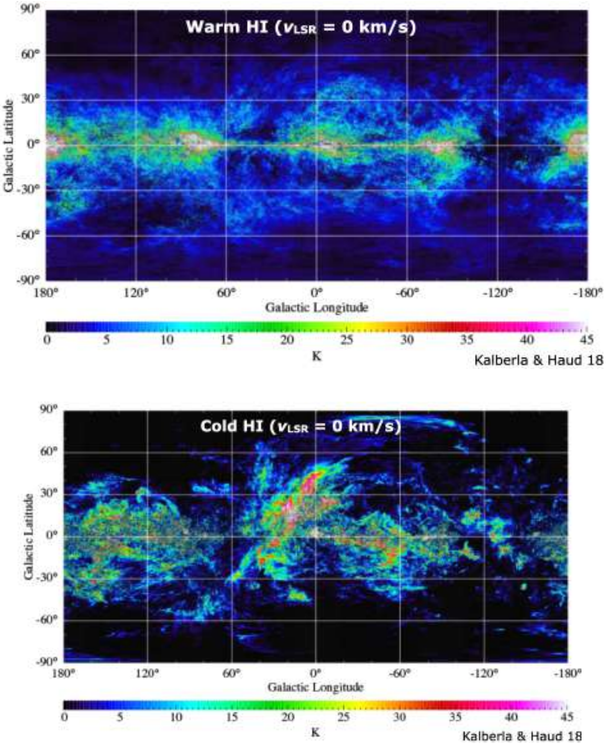

Figure 3.3: Top: warm H I tracing diffuse, extended gas. Bottom: cold H I highlighting denser, filamentary structures associated with the Galactic disk. The maps are shown in brightness temperature units (K). Adapted from Kalberla and Haud (2018).

(Fig. 3.5), with two peaks corresponding to the maximum projected rotation velocity on the approaching and receding sides of the disk. The width of the line reflects the rotational velocity projected along the line of sight and therefore depends on the inclination of the galaxy. The total flux is directly proportional to the total H I mass.

The distribution of H I within galaxies is described in terms of the column density, $N_{\rm H\,I}$, defined as the number of hydrogen atoms per unit area along the line of sight. This provides a direct measure of how much gas is present when projected onto the plane of the sky. At column densities of $N_{\rm H\,I} \sim 10^{21}\,{\rm cm}^{-2}$, atomic gas becomes sufficiently shielded to transition into molecular gas, marking the onset of star for-

(a) Near-infrared (2MASS)

(b) X-ray (eROSITA)

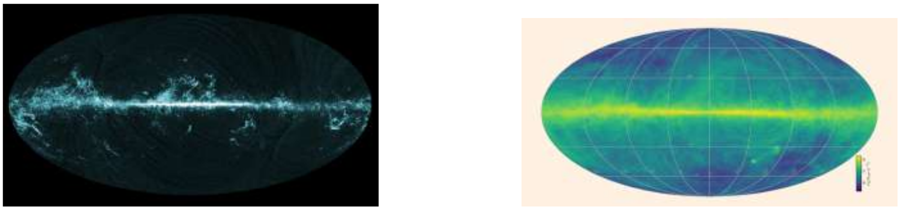

(c) Molecular gas (CO)

(d) Atomic hydrogen (H I)

Figure 3.4: Multiwavelength view of the Milky Way illustrating the distribution of its main baryonic components. *Top left:* Near-infrared emission from the 2MASS survey traces the stellar distribution and reveals the structure of the Galactic disk through dust extinction (Skrutskie et al., 2006). *Top right:* X-ray emission observed by eROSITA traces hot ionized gas in the Galactic halo and large-scale structures such as superbubbles (Predehl et al., 2021). *Bottom left:* Molecular gas traced by CO emission from *Planck* highlights dense molecular clouds concentrated along the Galactic plane (Planck Collaboration et al., 2014). *Bottom right:* Neutral atomic hydrogen (H I) from the HI4PI survey reveals an extended gas reservoir distributed across the disk and halo (HI4PI Collaboration et al., 2016). Together, these panels illustrate how different gas phases and the stellar component occupy distinct regions of the Galaxy.

mation. Lower column densities of $N_{\rm H\,I} \sim 10^{20}\,{\rm cm}^{-2}$ typically trace the outer regions of galactic thin disks, while values of $N_{\rm H\,I} \sim 10^{19}\,{\rm cm}^{-2}$ probe more diffuse gas in thick disks and the surrounding environment.

On larger scales, the distribution of H I in galaxies follows a well-defined scaling relation between the total H I mass and the size of the H I disk (see Fig. 3.6). The H I diameter is typically measured at a fixed column density threshold, commonly taken to be $N_{\rm H\,I} = 1.25 \times 10^{20}\,{\rm cm}^{-2}$ ($\sim 1\,M_\odot\,{\rm pc}^{-2}$), corresponding to the characteristic extent of the neutral gas disk. Observations show that this diameter is tightly correlated with the total H I mass (Broeils and M.-H. Rhee, 1997; J. Wang et al., 2016). This

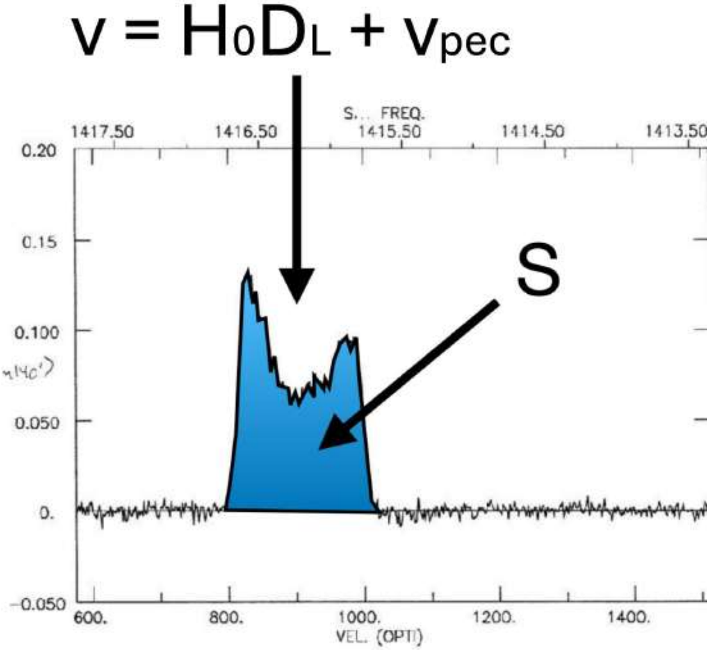

Figure 3.5: H I spectrum of a disk galaxy. The central frequency shift traces the observed recessional velocity ($v = H_0 D_L + v_{\rm pec}$), which is dominated by the Hubble flow but may include a contribution from the galaxy's peculiar motion. The integrated flux S is proportional to the total H I mass. The width of the profile reflects the rotational velocity of the galaxy. The characteristic double-horn shape arises from a rotating disk with a flat rotation curve. Image credit: Kelley Hess.

relation is remarkably consistent across different galaxy types and environments, implying that galaxies share a nearly constant average H I surface density. Physically, this reflects the balance between processes that convert atomic gas into molecular form in the inner regions and those that ionize low-density gas in the outer regions, naturally setting the extent of the H I disk. This property remains true, even after a galaxy has interacted with its environment.

The observed H I emission can be expressed in terms of brightness temperature, T_B, which provides a direct measure of the intensity of the radiation field. The spin temperature, T_s, describes the excitation of the hyperfine levels of neutral hydrogen and is defined through the ratio of atoms in the two spin states. Under conditions of

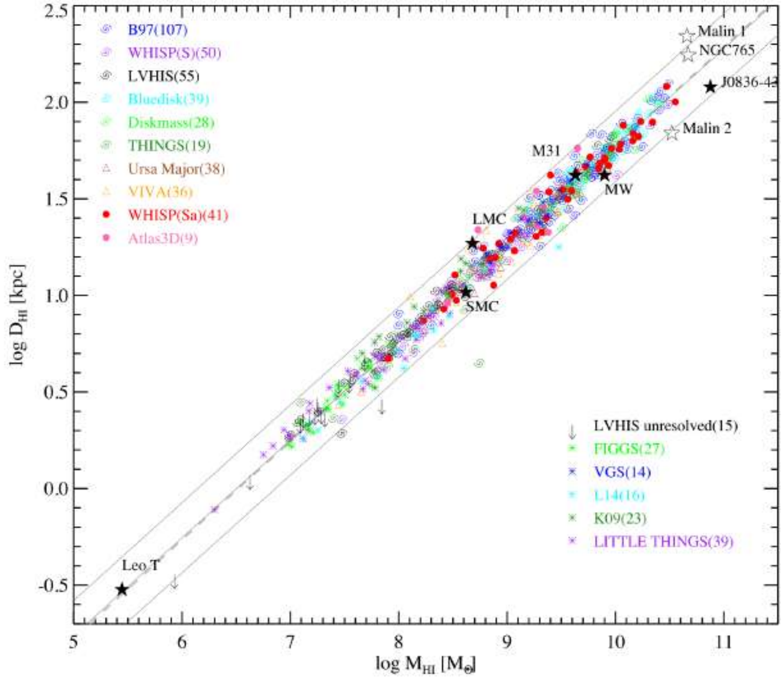

Figure 3.6: The D_{HI}–M_{HI} relation for 562 galaxies compiled from 15 interferometric data sets. Upper limits for unresolved galaxies from LVHIS are also shown. Selected individual galaxies are highlighted with star symbols. The solid lines represent the best-fitting linear relation and its 3σ scatter, while the dashed line indicates the relation from Broeils and M.-H. Rhee (1997). Figure from J. Wang et al. (2016).

thermal equilibrium, the relative populations of the upper and lower hyperfine levels are described by the Boltzmann equation,

$$\frac{n_1}{n_0} = \frac{g_1}{g_0} \exp\left(-\frac{h\nu_{\mathrm{HI}}}{kT_s}\right), \tag{3.1}$$

where n_1 and n_0 are the populations of the upper and lower hyperfine states, respectively, $g_1/g_0 = 3$ is the ratio of their statistical weights, and ν_{HI} is the rest-frame frequency of the H I hyperfine transition. For a medium with spin temperature T_s and optical depth τ, the brightness temperature can be written as

$$T_B = T_s(1 - e^{-\tau}), \tag{3.2}$$

and in the optically thin regime ($\tau \ll 1$),

$$T_B \approx T_s\,\tau. \tag{3.3}$$

The optical depth per unit frequency can be related to the volume density of neutral hydrogen atoms along the line of sight through

$$d\tau_\nu = -\frac{3c^2}{32\pi\nu_{\mathrm{H\,I}}} A_{21} n_{\mathrm{H\,I}} \frac{h}{kT_s}\phi(\nu)\,dl, \tag{3.4}$$

where $n_{\mathrm{H\,I}}$ is the volume density of neutral hydrogen, $\phi(\nu)$ is the line profile function, dl is an infinitesimal path length along the line of sight, k is the Boltzmann constant, h is Planck's constant, c is the speed of light, and A_{21} is the Einstein coefficient for the spontaneous hyperfine transition of neutral hydrogen. Integrating this expression over frequency and along the line of sight gives

$$N_{\mathrm{H\,I}} = \int n_{\mathrm{H\,I}}\,dl = \frac{32\pi k\nu_{\mathrm{H\,I}}}{3hc^2A_{21}} \int T_s\,\tau_\nu\,d\nu. \tag{3.5}$$

Changing variables from frequency to velocity using $d\nu = (\nu_{\mathrm{H\,I}}/c)\,dv$ gives

$$N_{\mathrm{H\,I}} = \frac{32\pi k\nu_{\mathrm{H\,I}}^2}{3hc^3A_{21}} \int T_s\,\tau(v)\,dv. \tag{3.6}$$

The quantity $T_s\tau$ can be related to the observed brightness temperature of the radiation field through the optically thin approximation, $T_B \approx T_s\tau$. Substituting this relation into the previous expression gives

$$N_{\mathrm{H\,I}} = 1.82 \times 10^{18} \int T_B(v)\,dv \quad \mathrm{cm}^{-2}, \tag{3.7}$$

where $T_B(v)$ is the brightness temperature measured by the telescope as a function of velocity v, expressed in $\mathrm{km\,s^{-1}}$. The integral is taken over the velocity width of the H I line, so that the column density is proportional to the velocity-integrated brightness temperature.

To connect this expression to observable quantities, the brightness temperature can be related to the measured flux density, S_ν, through the Rayleigh–Jeans approximation, which relates the specific intensity of the radiation field to an equivalent blackbody temperature,

$$T_B = (1+z)^3 \frac{c^2 S_\nu}{2k\nu_{\mathrm{H\,I}}^2 \Omega_{\mathrm{bm}}}, \tag{3.8}$$

where z is the redshift of the source, S_ν is the flux density, and Ω_{bm} is the beam solid angle. For a synthesized beam with major and minor axes a and b, the beam solid angle is given by

$$\Omega_{\mathrm{bm}} = \frac{\pi ab}{4\ln 2}. \tag{3.9}$$

Combining these relations, the column density can be written directly in terms of the observed flux density as

$$N_{\mathrm{H\,I}} = 2.33 \times 10^{20} (1+z)^4 \left(\frac{S}{\mathrm{Jy\,Hz}}\right)\left(\frac{ab}{\mathrm{arcsec}^2}\right)^{-1} \ \mathrm{cm}^{-2}, \tag{3.10}$$

where S is the frequency-integrated flux density per beam, and a and b are the major and minor axes of the synthesized beam. In this work, the frequency-integrated flux density is expressed in units of Jy Hz rather than the more commonly used Jy km s^{-1}. This choice reflects the native units of the data cubes and allows the H I column density and mass to be calculated directly from the observed spectral data without requiring an additional conversion from velocity to frequency units.

The total number of emitting hydrogen atoms is related to the luminosity of the line through the Einstein coefficient of the transition. For optically thin emission this gives

$$\mathcal{N}_{\mathrm{H\,I,tot}} = \frac{16\pi D_L^2 S}{3h\nu_{\mathrm{H\,I}} A_{21}}, \tag{3.11}$$

where D_L is the luminosity distance and S is the frequency-integrated flux density. Multiplying by the hydrogen atom mass m_H then yields

$$M_{\mathrm{H\,I}} = m_H \mathcal{N}_{\mathrm{H\,I,tot}} = 49.7\, D_L^2\, S \quad M_\odot, \tag{3.12}$$

where D_L is expressed in Mpc and S in Jy Hz.

These relations provide a direct connection between the observed flux density and both the column density and total mass of neutral atomic hydrogen (M. Meyer et al., 2017).

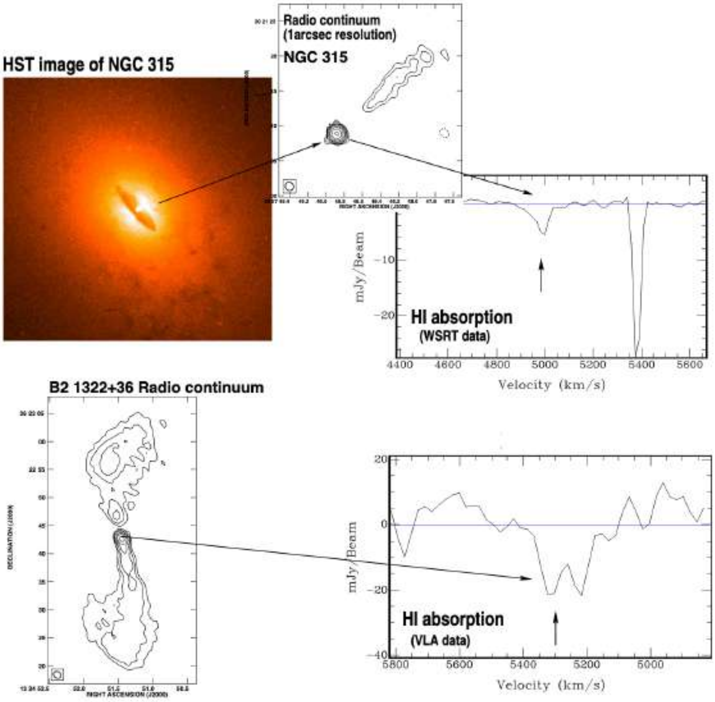

Figure 3.7: H I absorption detected with the WSRT and the VLA against the core of two radio galaxies: NGC 315 and B2 1322+36. The absorption appears as a decrement in flux density against the radio continuum emission, illustrating how H I absorption probes gas along the line of sight toward compact sources in the central regions of galaxies. Adapted from Morganti et al. (2001).

H I absorption

Unlike emission, H I absorption is only observed when neutral atomic hydrogen lies along the line of sight to a sufficiently bright background radio continuum source. Such continuum emission is commonly produced by synchrotron radiation associated with AGN. It can also arise from star-forming regions, where the continuum emission is produced by synchrotron emission from supernova remnants and thermal free–free emission. In this configuration, the intervening gas absorbs part of the continuum radiation, producing a decrement in the observed spectrum (see Fig. 3.7).

The observed decrement in flux density can be expressed in terms of the optical depth, allowing the H I column density to be estimated by integrating the optical depth over velocity according to

$$N_{\rm H\,I} = 1.82 \times 10^{18} \frac{T_s}{f} \int \tau(v)\, dv \quad {\rm cm}^{-2}, \tag{3.13}$$

following Wolfe and Burbidge (1975), where T_s is the spin temperature, f is the covering factor of the background continuum source, and $\tau(v)$ is the optical depth as a function of radial velocity.

H I absorption can be broadly divided into two classes: associated absorbers, which arise in the host galaxy of the background radio source, and intervening absorbers, which trace gas in unrelated galaxies along the line of sight. Large surveys such as the First Large Absorption Survey in H I (FLASH; Yoon et al. 2025) and the MeerKAT Absorption Line Survey (MALS; Deka et al. 2024) are designed to detect both types of systems, which are important for studying the gas content of galaxies across cosmic time. In this work, we focus on associated absorption.

In contrast to H I emission, which traces the global gas reservoir, H I absorption provides a localized view of the gas distribution, typically probing the inner regions of galaxies in the case of associated systems. In addition, H I emission is limited to a certain column density that depends on the present-day capabilities of radio interferometers. The depth of an H I absorption line, however, depends primarily on the strength of the background radio continuum source. Therefore, as long as the background source exists, we can in principle detect H I at larger redshift and lower column density than what is possible with H I emission.

H I absorption is therefore useful for studying the kinematics of gas in galaxies, and is particularly powerful in systems hosting AGN, where strong radio continuum emission allows the velocity structure of the absorbing gas to be studied in detail. In such systems, absorption profiles can reveal inflowing or outflowing gas, providing insight into the processes that regulate the fueling of the central engine and the impact of feedback on the surrounding interstellar medium (see Section 3.4).

H I rotation curves

It has already been mentioned that H I observations provide direct access to the kinematics of galaxies, for example through the overall rotational velocity traced by the width of the emission line. In spatially resolved observations, however, the velocity of the H I emission can be measured as a function of position, allowing the modeling of H I rotation curves. These rotation curves extend further than the stellar compo-

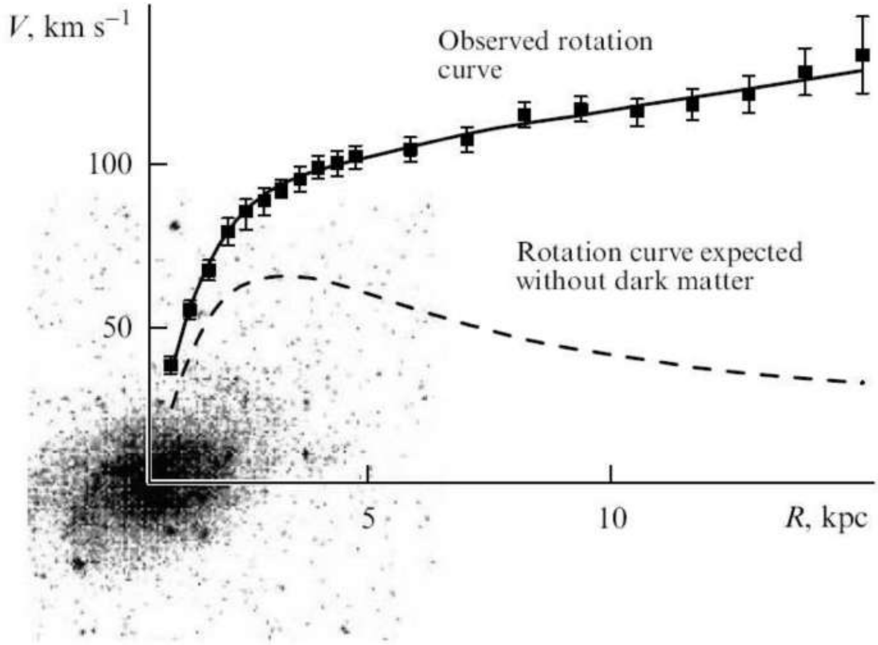

Figure 3.8: Example of a galaxy rotation curve. The inner regions are traced by stellar light, while H I observations extend the rotation curve to larger radii. The observed flat rotation at large distances indicates the presence of mass beyond the visible stellar disk. Figure from (Zasov et al., 2017).

nent, as H I typically reaches well beyond the optical disk. This allows the kinematics of galaxies to be probed at large radii, where the rotation curves are often observed to remain flat (see Fig. 3.8). The persistence of high rotational velocities at large distances cannot be explained by the gravitational potential of the visible matter alone, and provides strong evidence for the presence of an extended dark matter component surrounding galaxies (Rubin et al., 1980).

H I rotation curves also provide a sensitive probe of disturbances in the gas kinematics. Deviations from regular rotation can trace non-circular motions, such as radial inflows and outflows, as well as perturbations induced by bars and spiral density waves. By modeling the rotation curve and subtracting it from the observed velocity field, residual maps can be constructed to isolate gas that deviates from circular rotation, providing insight into extra-planar or dynamically disturbed components.

Observational limitations

The interpretation of H I observations is fundamentally limited by the sensitivity and resolution of the data. These factors determine which gas structures can be detected and how accurately their properties can be measured, and therefore influence our view of the distribution and kinematics of H I in galaxies.

A primary limitation arises from the sensitivity of the observations, which sets a minimum detectable column density. As a result, low column density gas can remain undetected, biasing observations toward denser structures. This is particularly important for extended, diffuse H I components, such as the outer regions of galactic disks or gas removed through environmental processes. This has posed a challenge for interferometric H I observations, historically requiring long integration times to reach the necessary sensitivity. However, recent advances in radio facilities, such as MeerKAT and upcoming instruments like the Square Kilometre Array (SKA), are significantly improving sensitivity through increased collecting area and lower system temperatures, enabling the detection of low column density H I and the study of diffuse gas structures that were previously inaccessible.

The spatial resolution of H I observations also affects the interpretation of the data. In interferometric observations, the angular resolution is approximately given by $\theta \sim \lambda / B_{\rm max}$, where $B_{\rm max}$ is the maximum baseline between antennas, which sets the smallest angular scale that can be resolved. As a result, the emission is effectively blurred, so structures smaller than this scale cannot be distinguished. This causes small-scale features to blend together, reduces the apparent peak column densities, and smooths velocity gradients in kinematic maps.

In addition, interferometric observations can miss extended, faint emission, as they are insensitive to angular scales larger than those corresponding to their shortest baselines. This results in a filtering of large-scale, low surface brightness structures, meaning that diffuse H I emission may not be fully recovered. This can lead to an underestimation of the total gas content. Arrays with a dense distribution of antennas on short baselines, such as MeerKAT, are therefore better suited to detect extended emission compared to arrays with fewer short spacings.

Finally, the common assumption that the gas is optically thin can lead to an underestimation of the true column density in regions of high gas density. Observational studies combining H I emission and absorption measurements in the Milky Way have shown that optical depth corrections can increase the inferred H I column density by

$\sim 38\%$ and the total H I mass by $\sim 31\%$, although these values likely represent lower limits and may vary depending on the local gas properties (Y. Wang et al., 2020).

As a result, the observed H I distribution represents only a partial and resolution-dependent view of the gas.

In practice, sensitivity and spatial resolution are closely linked, and improving one often comes at the expense of the other. Observations optimized for high resolution are better suited to resolving small-scale structures, but are typically less sensitive to diffuse gas. Conversely, observations optimized for sensitivity can recover extended emission, but at the cost of reduced spatial detail. A complete picture of the H I distribution therefore requires combining information across multiple spatial scales. In sparse arrays such as the VLA or ALMA, this is typically achieved by combining observations from multiple array configurations. In contrast, the dense distribution of antennas in the core of MeerKAT allows a broad range of spatial scales to be recovered within a single configuration by applying different weighting schemes during imaging, allowing both compact and diffuse gas components to be identified and properly characterized, as will be discussed in the following chapters.

3.3 Environmental impact on cold gas

As discussed in the previous chapters, galaxies in groups and clusters are subject to a variety of processes that can alter their evolution. Their impact is often seen most directly in the cold gas reservoir. In this context, H I is a particularly sensitive tracer of environmental transformation, since it is usually more extended and less tightly bound than the stellar disk.

Galaxies do not all contain the same amount of H I. Their neutral gas content is linked to global properties such as optical size and stellar mass, which define the expected H I reservoir of a galaxy in the absence of strong environmental perturbations. In particular, the H I mass is correlated with stellar mass, with low-mass galaxies often being more gas-rich relative to their stellar content, while more massive galaxies tend to have lower H I fractions.

Early studies of galaxies in dense environments revealed systematic deficits of neutral atomic hydrogen. In a study of galaxies in the Virgo cluster, R. D. Davies and Lewis (1973) found that galaxies exhibit reduced H I content across a range of morphological types. Recent studies have confirmed that this effect is widespread in dense environments, with galaxies in clusters consistently exhibiting reduced H I content compared to their field counterparts (Solanes et al., 2001; Boselli and Gavazzi, 2006; Jaffé et al., 2016).

A quantitative definition of H I deficiency was introduced by Giovanelli and Haynes (1985), who formalized this effect by comparing the H I content of galaxies in clusters to that of galaxies of similar morphological type in the field. The H I deficiency parameter is commonly defined as the logarithmic difference between the expected H I mass of a galaxy and its observed H I mass,

$$\mathrm{Def}_{\mathrm{HI}} = \log_{10}(M_{\mathrm{HI,exp}}) - \log_{10}(M_{\mathrm{HI,obs}}), \tag{3.14}$$

where $M_{\mathrm{HI,exp}}$ represents the H I mass expected for an isolated galaxy of similar properties, and $M_{\mathrm{HI,obs}}$ is the observed H I mass. Positive values of $\mathrm{Def}_{\mathrm{HI}}$ therefore indicate that a galaxy is deficient in H I relative to the field population.

The expected H I mass is typically estimated using scaling relations based on optical diameter and morphological type. For example, it can be expressed as (Solanes et al., 1996; Boselli and Gavazzi, 2009)

$$\log_{10}\left(h^2 M_{\mathrm{HI,exp}}\right) = c + d\log_{10}\left[\left(\frac{hD_{25}}{\mathrm{kpc}}\right)^2\right], \tag{3.15}$$

where D_{25} is the optical diameter measured at the $\mu_B = 25\,\mathrm{mag\,arcsec^{-2}}$ isophote, $h = H_0/(100\,\mathrm{km\,s^{-1}\,Mpc^{-1}})$, and c and d are coefficients that depend on morphological type.

Systems with high H I deficiency often exhibit truncated gas disks, asymmetric distributions, and extended, disturbed gas structures. An example of these signatures in a cluster environment is shown in Fig. 3.9, which presents galaxies from the VIVA survey in the Virgo cluster. The sample includes systems with clear signs of interaction, truncated H I disks, and disturbed morphologies consistent with RPS. These structures trace the response of the outer, loosely bound gas to gravitational interactions. Therefore, H I observations often provide information about the evolutionary history of the galaxy that would otherwise remain hidden.

Among the environmental processes discussed in Chapter 2, RPS is widely considered one of the primary mechanisms responsible for the removal of H I in cluster galaxies. The truncated gas disks and one-sided tails described before are commonly interpreted as signatures of this process (see left panel in Fig. 2.4). The efficiency of this process depends on the location of galaxies within the cluster; as introduced in Chapter 2, phase-space diagrams show that RPS is most effective for galaxies with high velocities and smaller clustercentric distances (e.g Jaffé et al., 2018). Building on this, the distribution of galaxies in phase space (see Fig. 3.10) highlights how the

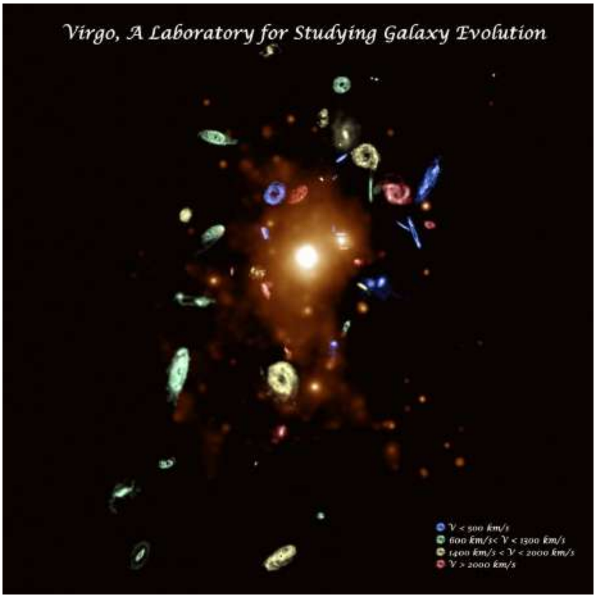

Figure 3.9: Galaxies from the VIVA (VLA Imaging of Virgo in Atomic Gas) survey overlaid on the ROSAT X-ray map of the Virgo cluster, tracing the hot ICM. The sample includes late-type galaxies spanning a wide range of environments, from the dense cluster core to the outskirts, and exhibits a diversity of H I morphologies, including undisturbed disks and strongly perturbed systems undergoing environmental processing. The H I images have been enlarged by a factor of 10 for clarity. Image credit: Chung et al. (2009); ROSAT X-ray image from Böhringer et al. (1994).

H I content varies across the cluster, with H I-poor systems located in the virialized region, which corresponds to galaxies that have spent a significant amount of time within the cluster potential and have therefore experienced prolonged environmental processing, while H I detections are more common in regions associated with recent infall.

The removal or redistribution of H I will then drive the evolution of galaxies toward more passive systems. Without a sustained gas reservoir, star formation declines over time, and galaxies transition from actively star-forming to quiescent states. This is also reflected in the phase-space distribution shown in Fig. 3.10, where passive (red) galaxies are found throughout the cluster, but dominate the virialized region. In contrast, star-forming systems are more commonly located in the infall region,

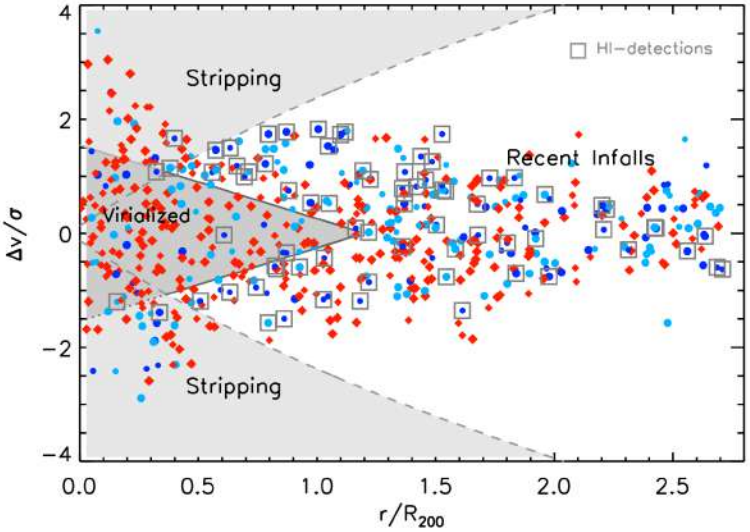

Figure 3.10: Phase-space distribution of galaxies in the Abell 963 cluster, colour-coded by their NUV−R colour, with red, cyan, and blue points indicating progressively bluer systems. H I detections are highlighted with grey squares. The shaded regions indicate areas associated with stripping, recent infall, and virialized populations (Jaffé et al., 2016).

where galaxies have not yet experienced the full impact of environmental processing. Together, these trends illustrate how the distribution of H I, star formation activity, and environment are closely linked in shaping the evolution of galaxies in dense environments (e.g. de la Casa et al., 2025).

3.4 Cold gas and nuclear activity

In Section 3.2, H I absorption was introduced as a decrease in flux against a background radio continuum source. In the absence of such a continuum source, H I absorption cannot be detected. In galaxies hosting an AGN, the radio continuum emission provides a bright background against which the intervening gas can be probed, making H I absorption observations particularly relevant for AGN studies. Fig. 3.7 shows a couple of examples of AGN related cases of H I absorption.

The first detections of H I absorption were made in the Centaurus A galaxy by

Roberts (1970), and since then H I absorption studies have been motivated by the possibility of probing the central regions of AGN hosts. Absorption profiles centred on the systemic velocity of the galaxy trace regularly rotating gas, while redshifted or blueshifted components relative to systemic velocity are commonly interpreted as signatures of inflowing or outflowing gas, respectively.

Early work by J. H. van Gorkom et al. (1989) suggested that most H I absorption was redshifted, which for some time led to the view that inflowing gas was common. This interpretation supported the idea that H I absorption could directly trace gas feeding the central SMBH. However, more recent studies have found that blueshifted H I absorption is more commonly observed (e.g. Vermeulen et al., 2003). This is consistent with AGN-driven outflows, where cold gas is accelerated away from the central regions. Thus, AGN outflows can have a direct impact on the gas available for star formation.

Not only is redshifted H I absorption less common, but its velocity offsets are typically smaller than those observed in blueshifted components. It remains unclear whether this reflects an intrinsic difference in the role of H I in AGN feeding, or whether inflowing gas is more difficult to detect observationally. In addition, the interpretation of redshifted absorption is not straightforward, since similar velocity offsets can arise from circumnuclear rotation. This is illustrated by the case of Centaurus A, where redshifted absorption was initially interpreted as inflow, but was later shown to be more consistent with a rotating circumnuclear disk (Morganti et al., 2008). Nevertheless, even if rare, clearer examples of H I inflow have been reported (e.g. Struve and Conway (2012), Maccagni et al. (2017), and Dutta and Srianand (2022)). In these cases, the absorption is typically characterised by narrow components that are redshifted relative to the systemic velocity, which are more difficult to reconcile with regular rotation and are therefore more naturally interpreted as individual gas clouds moving toward the central regions.

Taken together, these results indicate that H I absorption traces a complex circumnuclear environment in which multiple kinematic components can coexist. Regular rotation, inflow, and outflow may all be present within the same system, and their relative importance likely varies between galaxies. As a result, H I absorption is not a straightforward tracer of AGN fuelling alone, but rather provides a broader view of the interplay between cold gas and nuclear activity.

CHAPTER 4

Radio Interferometry

4.1 Fundamentals of radio interferometry

Radio interferometry is based on the principle that spatial information about the sky brightness distribution can be recovered by correlating the signals received by pairs of antennas separated by a finite distance. By measuring the complex voltages received at widely separated antennas and correlating them, an interferometer can achieve a much higher angular resolution than that of a single dish, with the resolution being primarily determined by the longest baselines in the array. Each pair of antennas forms a baseline that samples a specific spatial frequency component of the sky brightness distribution. The fundamental quantity measured by an interferometer is the complex visibility.

This can be illustrated with a simple two-element interferometer, shown in Fig. 4.1. Radiation from a source arrives at the two antennas with a geometric delay that depends on the baseline vector **b** and the direction of the source on the sky. This geometric delay can be written as

$$\tau_g = \frac{\mathbf{b} \cdot \mathbf{s}}{c}, \tag{4.1}$$

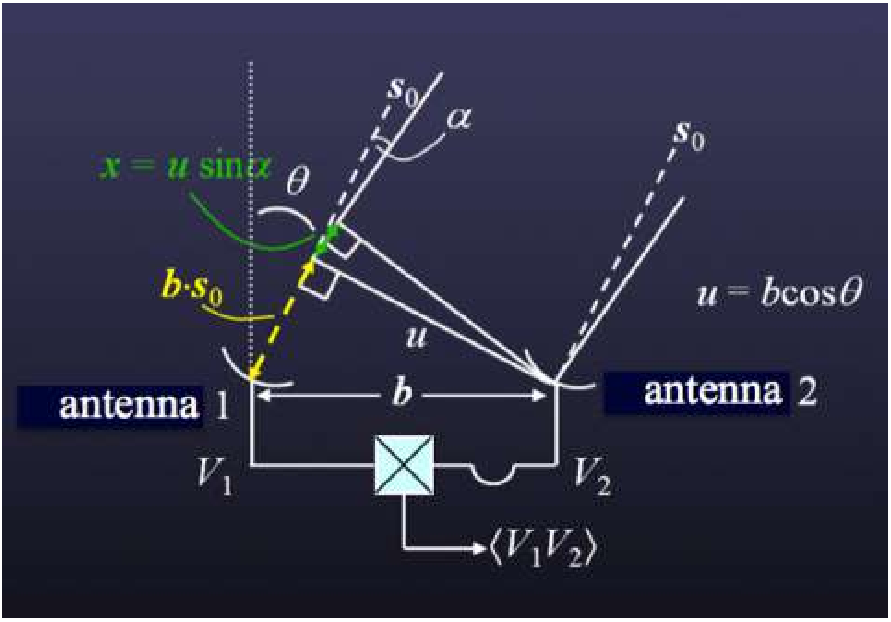

Figure 4.1: Schematic of a two-element radio interferometer. A baseline **b** separates two antennas observing a source in direction **s**. The difference in path length introduces a geometric delay τ_g between the received signals, resulting in a phase difference that is measured through their correlation. The projection of the baseline onto the source direction determines the spatial frequency sampled by the interferometer. Image credit: ALMA Science Portal.

where **s** is a unit vector pointing toward the source and c is the speed of light. This delay introduces a phase difference between the signals received at the two antennas, given by

$$\phi = 2\pi\nu\tau_g = \frac{2\pi}{\lambda}\,\mathbf{b}\cdot\mathbf{s}, \tag{4.2}$$

where ν is the observing frequency and λ is the corresponding wavelength.

The measured signal is therefore sensitive to the projection of the baseline onto the source direction. Each baseline samples a specific spatial frequency of the sky brightness distribution, corresponding to structures on a particular angular scale, with longer baselines probing finer detail and shorter baselines probing more extended emission. The correlation of the signals from the two antennas yields the complex visibility, which encodes both the amplitude and phase of this measurement.

For an extended sky brightness distribution $I(\mathbf{s})$, the visibility measured by a baseline can be written as

$$V(\mathbf{b}) = \int I(\mathbf{s})\, e^{-2\pi i\, \mathbf{b}\cdot\mathbf{s}/\lambda}\, d\Omega. \tag{4.3}$$

To express this relation in a more practical form, it is convenient to introduce a coordinate system on the sky. Defining (l, m) as the direction cosines with respect to the pointing center, and expressing the baseline in units of wavelength as (u, v, w), the visibility can be written as

$$V(u, v, w) = \iint \frac{I(l, m)}{\sqrt{1 - l^2 - m^2}}\, e^{-2\pi i(ul+vm+w(n-1))}\, dl\, dm, \tag{4.4}$$

where $n = \sqrt{1 - l^2 - m^2}$. This is the general measurement equation for an interferometer.

The coordinates (u, v, w) define a spatial frequency coordinate system associated with the interferometer, where the baseline vector is expressed in units of wavelength. In this framework, the (u, v) components correspond to spatial frequencies on the plane of the sky, while the w-component accounts for the projection along the line of sight. The set of visibilities $V(u, v, w)$ therefore represents a sampling of the sky brightness distribution in Fourier space, commonly referred to as the UV plane.

For small fields of view, where $l, m \ll 1$, the term involving w can be neglected and $n \approx 1$. In this approximation, the expression simplifies to

$$V(u, v) = \iint I(l, m)\, e^{-2\pi i(ul+vm)}\, dl\, dm, \tag{4.5}$$

which shows that the measured visibilities correspond to the two-dimensional Fourier transform of the sky brightness distribution.

While this approximation is valid for small fields of view, it breaks down for wide-field observations where the non-coplanar nature of the array becomes significant. In such cases, the w-term, which accounts for the deviation of the baselines from a common plane, introduces phase errors that cannot be neglected and lead to distortions in the reconstructed image. This effect becomes increasingly important for instruments with large fields of view, such as MeerKAT. To address this, modern imaging algorithms explicitly account for the w-term during the inversion process. For example, the imager `WSClean` implements the *w*-stacking algorithm, which corrects for the *w*-term by separating the data into layers of constant *w* and applying the corresponding phase corrections during imaging (Offringa et al., 2014).

4.2 Sampling of the UV plane

In practice, an interferometer does not measure the visibility function continuously across the UV plane, but instead samples it at a finite number of discrete locations determined by the distribution of baselines in the array. The UV plane represents the Fourier domain of the sky brightness distribution, where each point corresponds to a specific spatial frequency and direction (or angle) on the sky. These spatial frequencies correspond to structures on particular angular scales. Each antenna pair measurement provides two points in this plane: the visibility and its complex conjugate, set by the projected baseline in units of wavelength.

This sampling can be visualized in Fig. 4.2. The left panel shows the physical configuration of the array, where each pair of antennas defines a baseline. The middle panel shows the corresponding instantaneous sampling of the UV plane. Each point in the UV plane is produced by a pair of antennas, since a baseline is defined by the difference between their positions, and the full set of sampled points is therefore determined by all possible antenna pairs, directly reflecting the array configuration. In fact, for a snapshot observation, this sampling can be understood as the autocorrelation of the antenna distribution projected onto the plane perpendicular to the source direction, excluding the zero-spacing term, which is not measured by interferometers. As the Earth rotates, the baselines change with time as projected onto the sky, causing each antenna pair to trace out a track in the UV plane, as shown in the right panel. The resulting sampling pattern, known as the UV coverage, determines how completely the Fourier transform of the sky brightness distribution is measured.

Because only a finite number of spatial frequencies are sampled, the Fourier plane is inherently incomplete. As a result, the inverse Fourier transform of the visibilities does not yield the true sky brightness distribution and instead has no unique solution, requiring additional assumptions about the sky brightness distribution. In particular, the absence of very short baselines leads to missing information on extended emission, while the longest baselines set the maximum achievable angular resolution.

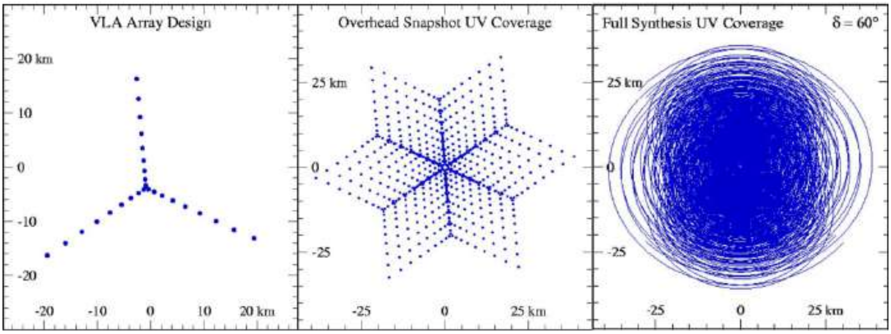

Figure 4.2: Example of UV coverage for the Very Large Array (VLA). Left: antenna configuration (see Fig. 1.4). Middle: instantaneous sampling of the UV plane. Right: full UV coverage from Earth rotation synthesis. Image credit: National Radio Astronomy Observatory.

4.3 Image reconstruction and deconvolution

The incomplete sampling of the UV plane means that the inverse Fourier transform of the measured visibilities does not directly recover the true sky brightness distribution. This process is illustrated in Fig. 4.3.

In the Fourier domain (top row of Fig. 4.3), the left panel represents the UV plane, which corresponds to the full Fourier transform of the sky brightness distribution. However, an interferometer does not measure this quantity directly. Instead, it samples the UV plane at a finite number of discrete points, determined by the available baselines, as shown in the middle panel. The measured UV data therefore correspond to the true UV plane multiplied by the sampling pattern, resulting in the sampled UV plane shown in the right panel.

Applying the inverse Fourier transform to the measured UV data (top right panel of Fig. 4.3) yields an image in the sky domain. However, because the UV plane is only sampled at discrete points, this operation does not recover the true image (bottom left panel), but instead produces the dirty image, shown in the bottom right panel. The difference between the dirty image and the true image is set by the dirty beam, shown in the middle panel. The dirty beam is the Fourier transform of the UV sampling and acts as the point spread function (PSF) of the interferometer. Due to the incomplete and irregular sampling of the UV plane, it typically contains significant sidelobes, which introduce artefacts that can obscure faint emission and complicate

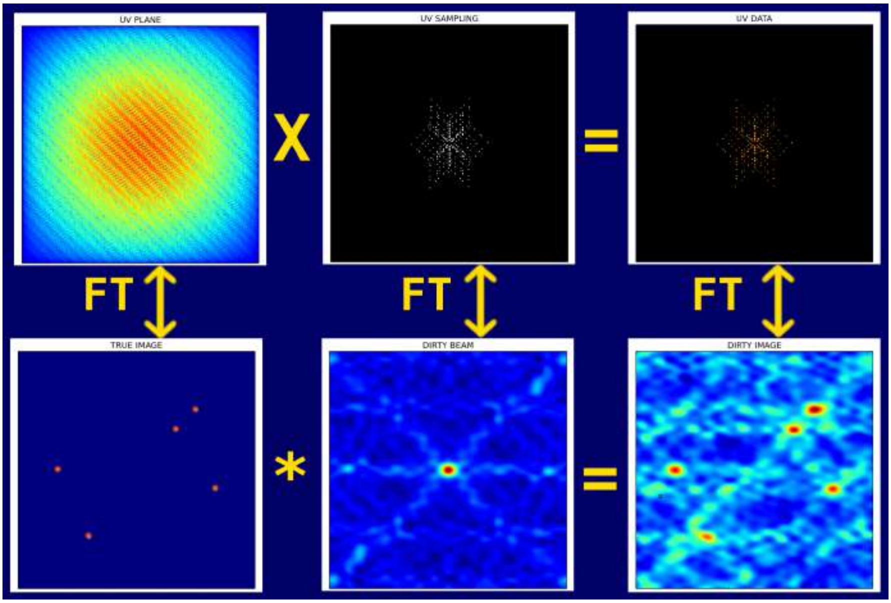

Figure 4.3: Illustration of interferometric image formation. Top row: the UV plane (left) is sampled at discrete points by the interferometer (middle), producing the measured UV data (right). Bottom row: applying the inverse Fourier transform yields the corresponding image domain representation. Due to incomplete UV sampling, the reconstructed image (dirty image, right) is the convolution of the true image (left) with the dirty beam (middle). Image credit: Iván Martí-Vidal.

the interpretation of the observed structure.

To remove these effects, deconvolution techniques are applied to the dirty image. This is what is known as "cleaning" the image. The most commonly used method in radio interferometry is the CLEAN algorithm (Högbom, 1974). In practice, CLEAN assumes that the sky brightness distribution can be represented as a collection of discrete point-like components. The algorithm proceeds iteratively by identifying the brightest peak in the dirty image and subtracting a scaled version of the dirty beam centered at that position. This subtraction removes not only the peak itself, but also the pattern of sidelobes produced by that source. The position and flux associated with this peak are recorded as part of a model of the sky brightness distribution. The process is then repeated on the residual image, where a new brightest peak is identified and treated in the same way. In this manner, CLEAN progressively reduces the influence of sidelobes while building up a model of the underlying emission. Once this process is finished, the model made by the collection of point-like components is convolved with an idealized beam, known as the clean beam, which is typically taken to be a Gaussian approximation of the central component of the dirty beam. The convolved model is then combined with the residual image to produce the restored image.

4.4 Spectral data cubes and derived products

In radio interferometric observations, imaging is typically performed across a range of frequencies. This results in a three-dimensional dataset known as a data cube, where two axes correspond to spatial coordinates on the sky and the third axis represents frequency, or alternatively velocity. This structure is illustrated in Fig. 4.4. Each slice of the cube along the spectral axis corresponds to a channel map, that is, an image of the sky at a specific frequency. By assembling these channel maps together, the data cube captures how the emission varies across the sky and as a function of frequency.

The data cube can be explored in different ways to extract physical information. Integrating the emission along the spectral axis produces moment maps, as shown on the left-hand side of Fig. 4.4. The zeroth moment (moment 0) corresponds to the total emission, tracing the overall distribution of H I. An example of this is shown by the contours in the left panel of Fig. 2.4. Higher-order moments provide information on the velocity (moment 1) and velocity dispersion of the gas (moment 2). In Fig. 4.4, the lower left panel illustrates how different velocity components can be separated and compared, highlighting variations in the kinematic structure of the emission. Additionally, the cube can be explored along the spatial axes by extracting spectra, as illustrated on the right-hand side of Fig. 4.4. By extracting spectra from individual positions or regions, it is possible to trace the velocity structure of the gas along the line of sight. Together, these representations provide complementary views of the same dataset, linking the spatial distribution of the emission with its kinematic properties.

4.5 Weighting, tapering, and spatial filtering

Although deconvolution techniques such as CLEAN improve the fidelity of the reconstructed image, the final result still depends on how the visibilities are weighted

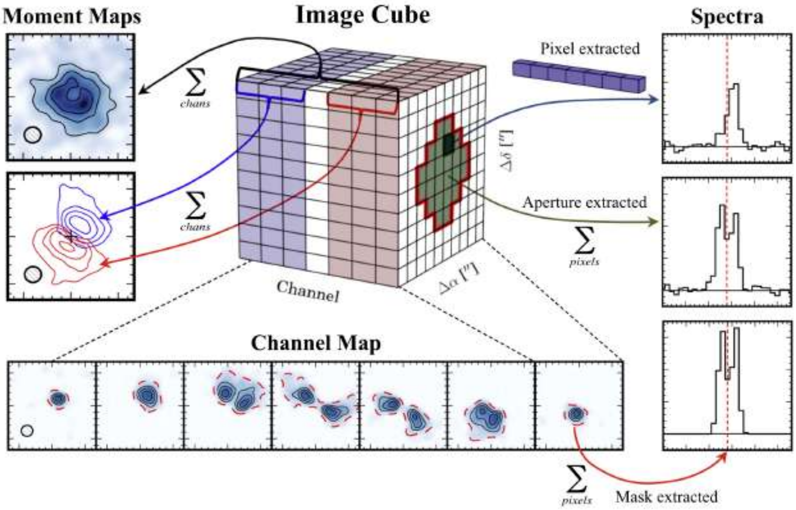

Figure 4.4: Schematic representation of a spectral data cube. Each slice along the spectral axis corresponds to a channel map, representing the sky brightness distribution at a given frequency. Integrating along the spectral axis produces moment maps, while extracting along the spatial axes yields spectra from individual pixels or regions. From Loomis et al. (2018).

during the imaging process. Prior to the Fourier transform step that produces the dirty image, the visibilities must be gridded onto a discrete UV plane, where multiple measurements can fall within the same pixel. In this step, each visibility is assigned a weight that determines how strongly it contributes to the final image. Different weighting schemes can be used to combine the visibilities within each pixel, and these choices directly influence the properties of the resulting image, including its angular resolution and noise level, and the structure of the synthesized beam.

At the two extremes, visibilities can be weighted using either natural or uniform weighting. Natural weighting assigns weights according to the inverse variance of each visibility, giving more importance to measurements with higher signal-to-noise ratio. Since densely sampled regions of the UV plane contain more visibilities, this scheme naturally favours them. In contrast, uniform weighting assigns weights based on the number of visibilities within each (u, v) cell, reducing the contribution of densely sampled regions so that all parts of the UV plane are more equally represented. The key difference between these approaches is that natural weighting prioritizes the quality of the measurements, while uniform weighting compensates for the non-uniform sampling of the UV plane. Between these two extremes, robust weighting introduces a tunable compromise, allowing a continuous transition between natural and uniform weighting.

Robust weighting was introduced by (Briggs, 1995) as a way to bridge these two approaches. Instead of applying a single weighting scheme across the entire UV plane, it adjusts the weights based on the local density of visibilities, with sparse regions weighted more like natural weighting and dense regions more like uniform weighting. The extent to which the weighting follows this behaviour is controlled by the robustness parameter: large values produce weighting schemes closer to natural weighting overall, while small (and negative) values approach uniform weighting.

In practice, different values of the robustness parameter lead to different trade-offs between noise and resolution. Natural weighting minimises the noise in the image but produces a broader synthesized beam, while uniform weighting improves resolution and reduces sidelobes at the cost of higher noise. This behaviour is illustrated in Fig. 4.5, where decreasing the robustness parameter leads to a narrower synthesized beam and higher noise, while increasing it produces a broader beam with lower noise. By varying the robustness parameter, it is possible to move between these regimes and select a balance appropriate for the scientific goals of the observation.

In addition to the weighting schemes described above, visibilities can be further modified through a taper parameter. This parameter adjusts the weights as a function of distance from the center of the UV plane, typically reducing the contribution of visibilities at larger (u, v) radii. Since these correspond to longer baselines, this reduces the contribution of high-resolution information and results in a broader synthesized beam. This is particularly useful when studying extended emission, as it increases the sensitivity to large-scale structures that are otherwise difficult to recover at higher resolution. By reducing the contribution of long baselines, which probe small spatial scales, the image becomes more sensitive to diffuse emission, at the expense of fine spatial detail.

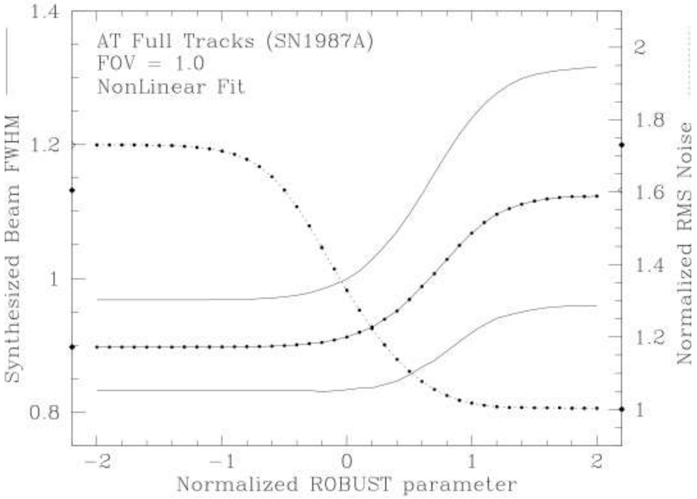

Figure 4.5: Trade-off between synthesized beam size and image noise as a function of the robustness parameter. The three solid curves show the synthesized beam FWHM, corresponding to the major axis (B_{maj}), minor axis (B_{min}), and their geometric mean. The dotted curve shows the normalized RMS noise (right axis). From Briggs, 1995.

CHAPTER 5

Data Processing

5.1 Observational data overview

The data used in this work are part of a deep MeerKAT H I and radio continuum mosaic of the Antlia cluster (more details on the Antlia cluster are given in Chapter 6; SCI-20210212-KH-01, PI: K. Hess). The observations consist of 10 overlapping pointings covering a total area of approximately 8.5 deg^2, designed to map the cluster core, its outskirts, and the surrounding environment within a single dataset. This mosaic provides wide-area coverage combined with high sensitivity to neutral hydrogen, enabling the study of gas properties across a range of environments within the cluster.

These observations were carried out with the MeerKAT radio interferometer, located in the Karoo region of South Africa (Fig. 5.1). MeerKAT consists of 64 dishes with baselines ranging from tens of meters to approximately 8 km, providing high sensitivity and angular resolution for H I observations. MeerKAT is the successor to KAT-7 and serves as a precursor to the SKA. Previous H I observations of the Antlia cluster were carried out with the KAT-7 array (Hess et al., 2015), which consisted of seven dishes and provided the first unresolved view of the H I distribution in the cluster. This project therefore represents a direct follow-up to that work, enabling

Figure 5.1: The MeerKAT radio interferometer located in the Karoo region of South Africa. The array consists of 64 dishes distributed over baselines of up to ~8 km.

a significantly more detailed view of the H I distribution in the Antlia cluster and allowing us to trace it to larger radii.

The observations were carried out in L-band, covering a frequency range of approximately 900–1670 MHz. The data were recorded using the 32K correlator mode, providing 32 768 spectral channels with a channel width of 26.1 kHz. The mosaic was observed over eight observing sessions, with an average on-source integration time of approximately 4.5 hours per pointing.

The raw visibility data were processed on the ilifu computing cluster hosted at the Inter-University Institute for Data Intensive Astronomy (IDIA) using the CARACal pipeline[1], which is designed for automated calibration and imaging of MeerKAT observations. The calibration included standard cross-calibration steps, consisting of bandpass and gain calibration using calibrator sources, followed by a self-calibration step to refine the gain solutions using continuum emission within the target field.

The subsequent imaging strategy, including the choice of imaging parameters, the multi-resolution processing, and the source-finding procedure, is described in the following sections.

---

[1] `https://caracal.readthedocs.io`

Table 5.1: H I data cube properties for the four imaging setups. The name given to each cube corresponds to the average of the major and minor axes of the synthesized beam. Listed are the Briggs robustness parameter, the applied uv-taper, the resulting synthesized beam, the rms noise per channel, and the corresponding column density sensitivity evaluated at a level of $3\sigma_{\mathrm{NGC3281}}\Delta v$. Here, $\sigma_{\mathrm{NGC3281}}$ is the rms noise measured around the mask of NGC 3281 at the respective resolution (computed using SoFiA-2), and we adopt $\Delta v = 20\ \mathrm{km\,s^{-1}}$.

name	robust	taper (kλ)	resolution (arcsec)	noise (Jy beam^{-1})	$N_{\mathrm{HI},3\sigma}$ (cm^{-2})
70″	0.5	60	71.1″ × 69.3″	3.5×10^{-4}	5.3×10^{18}
48″	0.5	30	49.7″ × 46.1″	2.8×10^{-4}	8.2×10^{18}
30″	0.0	15	34.4″ × 26.2″	2.7×10^{-4}	2.1×10^{19}
16″	0.0	6	20.5″ × 12.1″	2.2×10^{-4}	6.6×10^{19}

5.2 Imaging parameter choices

The imaging of interferometric data requires a balance between angular resolution and surface brightness sensitivity. This balance is primarily controlled through the choice of visibility weighting and the application of uv-tapering, as discussed in Chapter 4. In this work, a set of imaging parameters was selected to probe different spatial scales of the H I emission in the Antlia cluster.

We adopted Briggs weighting with two values of the robust parameter, combined with a set of uv-tapers to produce images at multiple angular resolutions. Specifically, robust values of 0.5 and 0 were used together with uv-tapers of 60, 30, 15, and 6 kλ. The adopted combinations are summarized in Table 5.1.

The different imaging configurations are referred to by the characteristic angular resolution of the resulting data cubes, given by the average of the major and minor axes of the synthesized beam. Throughout this work, we therefore refer to the cubes as the 70″, 48″, 30″, and 16″ datasets, corresponding to progressively higher angular resolution.

The chosen combinations reflect a progression from high surface brightness sensitivity to high angular resolution. At the lowest resolution (70″), the use of a relatively high robust parameter together with a strong uv-taper maximizes sensitivity to extended, diffuse H I emission. As the resolution increases (48″, 30″, and 16″), the taper is reduced and a lower robust value is adopted, placing greater weight on longer baselines and allowing smaller-scale structures to be resolved.

5.3 Multi-resolution imaging strategy

Concept of the multi-resolution approach

The imaging strategy adopted in this work follows the approach developed in the Fornax cluster survey (Serra et al., 2023) and the MHONGOOSE survey (de Blok et al., 2024). The key idea is to process the data sequentially from low to high angular resolution, using the higher sensitivity of the low-resolution cubes to guide the recovery of emission at higher resolutions.

At low resolution (e.g. the 70″ cube), the sensitivity to diffuse emission is maximized, enabling robust detection of extended H I structures. At higher resolutions (48″, 30″, and 16″), the sensitivity to extended emission decreases, but smaller-scale structure can be resolved. The multi-resolution approach therefore combines the strengths of both regimes to recover the H I distribution across a wide range of spatial scales.

Iterative mask-driven approach

A key component of this method is the use of source-finding masks to guide the cleaning process across resolutions. In this context, a mask is a three-dimensional selection of pixels in the data cube that are identified as containing signal.

At the lowest resolution (70″), source finding is first performed (see Section 5.4) to generate an initial mask. This mask is then used to constrain the cleaning of the data, restricting the deconvolution to regions where emission is detected. After cleaning, source finding is repeated on the improved cube to produce an updated mask. This updated mask is then used as input for the cleaning of the next-highest-resolution dataset.

This process is repeated across the different resolutions, such that the cleaning at each stage is guided by progressively refined masks. In this way, faint emission detected at low resolution can be consistently recovered at higher resolution, even where the signal would otherwise fall below the detection threshold.

Data processing workflow

At each of the imaging configurations listed in Table 5.1, the data were first processed in the visibility domain, including continuum subtraction and mitigation of contaminating emission such as solar interference. The data were then imaged and deconvolved for each pointing and observing session, producing spectral data cubes. This resulted in a set of cubes for the eight observing sessions across the 10 pointings. These cubes were then combined by stacking the observations corresponding to each pointing, increasing the overall sensitivity and producing a single cube per pointing. In parallel, the corresponding PSF cubes were combined in the same manner, which is required for the subsequent processing steps.

The resulting set of stacked cubes were first combined into a single mosaic at the lowest resolution (70″) using `MosaicQueen`[2], producing the full 2.8° × 3.6° mosaic. This initial low-resolution mosaic was inspected, revealing the presence of residual continuum emission arising from an inadequate subtraction due to strong H I emission. The brightest H I sources also exhibited strong H I sidelobes, which are not residual artifacts but arise from the intrinsic response of the MeerKAT beam and become significant only for very bright sources. These effects affected the overall data quality and compromised the reliability of the initial source finding.

To address these issues, an improved imaged based continuum subtraction and cleaning strategy was required. The residual continuum emission was first mitigated by fitting and subtracting a natural cubic spline baseline along the spectral axis at each spatial pixel. However, the cleaning could not be performed directly on the mosaic, as the PSF varies across the field and cannot be represented by a single PSF. Instead, the cleaning was carried out in the image plane on the stacked cubes of the individual pointings using the Apercal implementation of Miriad, parallelized by channel. A shallow clean was first applied to each pointing, using a threshold of 3σ and restricted to a source mask derived from the initial low-resolution mosaic, as described above, effectively removing the strongest sidelobe structures associated with the bright continuum sources.

The shallow cleaned pointings were then recombined into a mosaic, producing an improved cube for the full field. This updated mosaic was used to perform a deeper source finding step, yielding an initial mask for the full dataset. This mask was then regridded back to the individual pointings and used to guide a subsequent deeper clean, performed down to a threshold of 0.5σ and restricted to the mask.

For the higher-resolution imaging configurations, the cubic spline continuum subtraction was repeated, but an additional shallow cleaning step was not required, as the cleaning was guided by the mask obtained at the previous resolution. This iterative process allowed the recovery of emission to be progressively refined from low to high resolution.

---

[2] `https://github.com/caracal-pipeline/MosaicQueen`

5.4 Source finding

The identification of H I emission within the data cubes was carried out using the SoFiA-2 source finding software (Serra et al., 2015; Westmeier et al., 2021). In this context, source finding refers to the automated detection of emission within three-dimensional data cubes. The output of this process consists of a catalog of detected sources together with a corresponding mask, which defines the spatial and spectral extent of the detected emission. This mask is a key component of the analysis, as it is used to guide the cleaning of the data and forms the basis of the final source catalog.

The source finding was performed iteratively as part of the multi-resolution imaging strategy described in the previous section. The detection was performed using the smooth-and-clip (S+C) algorithm implemented in SoFiA-2, in which the data cube is smoothed over a set of spatial and spectral scales and thresholded relative to the local noise. Detected pixels are grouped into three-dimensional structures, and a reliability filter is applied to distinguish genuine H I emission from noise fluctuations based on their statistical properties. This filtering is illustrated in Fig. 5.2, where detections are shown in different projections of parameter space. Negative detections (red points) trace the noise distribution, while positive detections (blue points) include both real sources and noise fluctuations. The reliability filter identifies sources that separate from the noise-dominated population, which are shown as black points.

At each stage of the workflow, the source finding was intentionally performed using relatively permissive detection parameters in order to maximize completeness and ensure that faint emission was not missed. The resulting catalogs and masks were then visually inspected using CASA together with diagnostic products generated using the SoFiA Image Pipeline (SIP; Hess 2022), which produces moment maps, position–velocity diagrams, spectral profiles, and multiwavelength overlays based on the SoFiA source catalog and masks. This inspection was performed at all spatial resolutions. Detections lacking spatial or spectral coherence, or associated with residual sidelobes, noise fluctuations, or continuum subtraction artifacts, were identified as spurious and removed manually before the masks were used in subsequent cleaning steps.

An example of a detected H I source and its corresponding diagnostic products is shown in Fig. 5.3. The source exhibits a clear optical counterpart in the DECam r-band image, spatially coincident with the H I emission. The moment-0 map shows an extended and symmetric H I distribution, while the moment-1 map displays a smooth velocity gradient consistent with ordered rotation. The position–velocity diagrams further confirm this kinematic structure, and the integrated spectrum shows a high

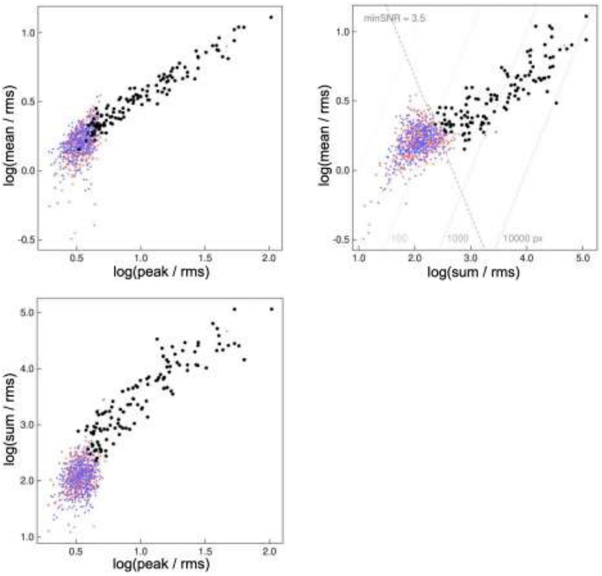

Figure 5.2: Reliability analysis from SoFiA-2 for the 70″ deep-clean cube. The panels show different projections of the parameter space used to classify detections: *top-left:* log(mean/rms) versus log(peak/rms), *top-right:* log(mean/rms) versus log(sum/rms), and *bottom-left:* log(sum/rms) versus log(peak/rms). Each point corresponds to a detection identified by the source finder. Red points represent negative detections tracing the noise distribution, while blue points correspond to positive detections prior to reliability filtering. Black points indicate sources classified as reliable by the algorithm. The dashed line in the top-right panel represents the statistical boundary used by the reliability filter to separate genuine H I emission from noise.

signal-to-noise detection with a well-defined profile. Together, these diagnostics indicate a robust and physically coherent H I detection.

These diagnostics helped assess the reliability of each detection. While the presence of an optical counterpart or a clear velocity gradient provided supporting evidence, neither was strictly required. In practice, genuine H I detections were identified by emission that is spatially well-defined and persists across multiple consecutive channels, whereas spurious detections were typically irregular and confined to isolated pixels or channels.

The final masks obtained for the 70″, 48″, 30″, and 16″ cubes are shown in

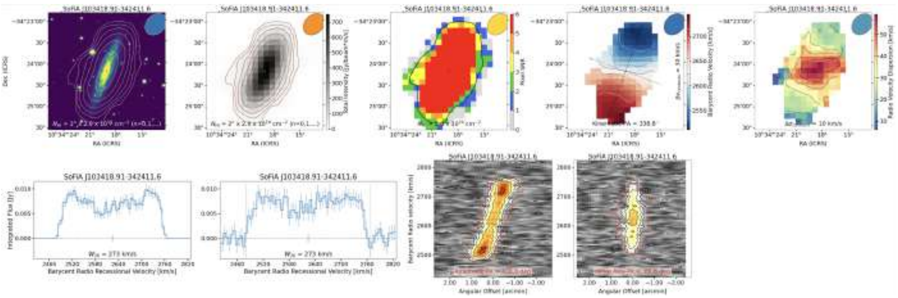

Figure 5.3: Example of a detected H I source and its corresponding SIP diagnostic products. *Top row (left to right):* DECam optical image (r-band) with H I contours, integrated H I intensity (moment-0) map, pixel signal-to-noise ratio map, velocity field (moment-1), and velocity dispersion map (moment-2). *Bottom row (left to right):* integrated spectrum, masked/aperture spectrum, and position–velocity diagrams along the major and minor axes. The source is consistent with a disk galaxy hosting an extended H I reservoir.

Fig. 5.4. These masks represent the final outcome of the source-finding procedure and define the H I detections used throughout the analysis. The figure illustrates the spatial extent of the H I emission identified across the Antlia field and how the detected structures are represented across different angular resolutions. Not all sources are detected at all resolutions, reflecting the different sensitivity of each dataset to diffuse and compact H I emission.

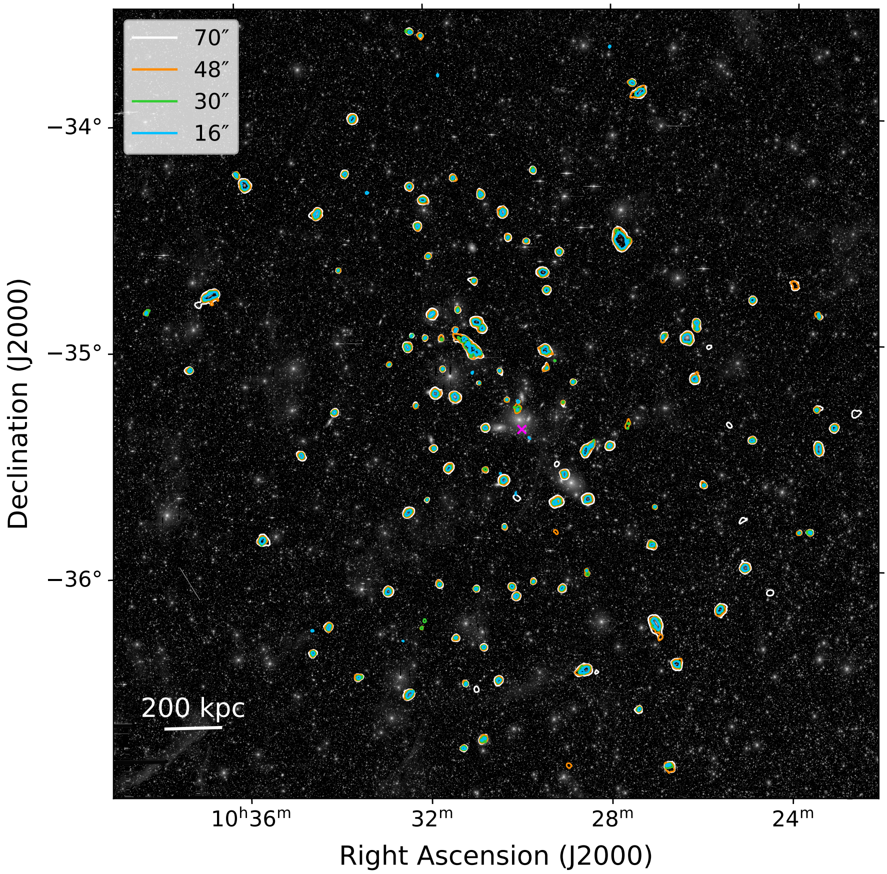

Figure 5.4: DECam *r*-band image of the Antlia cluster overlaid with the final H I masks derived from the source-finding procedure at each resolution; white, orange, lime, and sky blue correspond to the 70″, 48″, 30″, and 16″ datasets, respectively. The magenta cross marks the adopted center of the Antlia cluster. The comparison highlights how extended, diffuse structures are more prominent at lower resolution, while higher-resolution datasets resolve the more compact components of the H I distribution.

CHAPTER 6

NGC 3281 in the Antlia Cluster

6.1 The Antlia cluster

The Antlia cluster is the third closest galaxy cluster to the Milky Way Galaxy, at a distance of $\sim$ 38 Mpc (Hess et al., 2015). It has a virial radius of $\sim$ 887 kpc (Wong et al., 2016) and a total mass of $\sim 8 \times 10^{13}\, M_{\odot}$, placing it among the nearby cluster population alongside Virgo and Fornax. Unlike these more relaxed systems, Antlia is a dynamically young cluster that is still in the process of assembly.

The cluster is composed of two main substructures centered on the two brightest cluster galaxies (BCGs), NGC 3268 and NGC 3258 (see Fig. 6.1), which are in the process of merging. These two groups are aligned along the same direction as the large-scale filament connecting Antlia to the Hydra Cluster, suggesting a connection between the merger geometry and the surrounding large-scale structure.

Previous H I observations of the Antlia cluster with KAT-7 showed that H I detections are predominantly located in the outskirts, with the central regions largely devoid of neutral atomic hydrogen (Hess et al., 2015). This is illustrated in Fig. 6.2, where the detections are distributed around the cluster and avoid the regions of strongest X-ray emission. However, in dynamically young and merging clusters, galaxies may still retain significant amounts of cold gas and show signs of ongoing

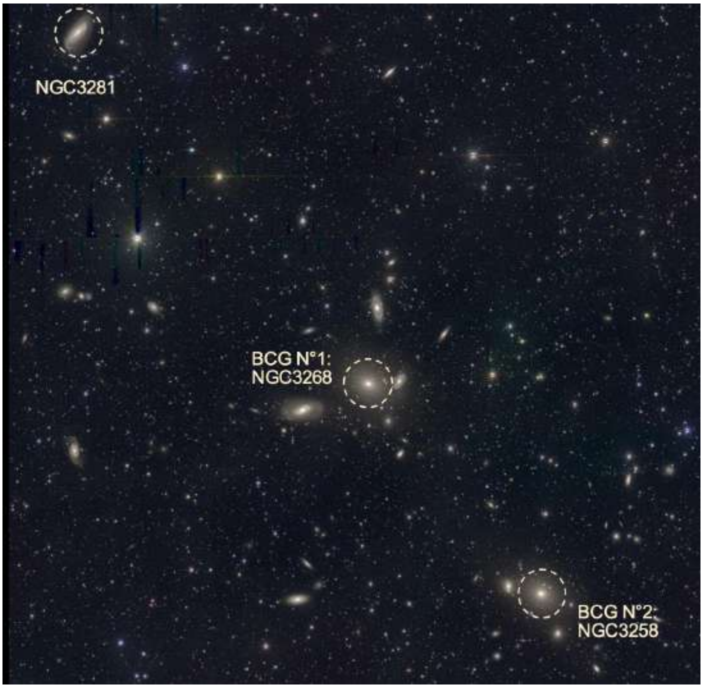

Figure 6.1: Optical image of the Antlia cluster showing its main structural components. The two brightest cluster galaxies (BCGs), NGC 3268 and NGC 3258, define the primary substructures of the cluster, which are believed to be in the process of merging. NGC 3281 is located in the outskirts of the cluster, within the region where environmental effects begin to influence galaxy evolution. The field of view covers approximately the inner half of the cluster virial radius.

evolution compared to more relaxed systems (Cava et al., 2017; Noble et al., 2017; Stroe et al., 2017). As shown in Fig. 5.4, the deeper MeerKAT observations reveal a larger population of H I sources across the cluster, including low H I mass systems located closer to the cluster center than previously detected.

The dynamical state of a cluster is reflected in the properties of the ICM. In relaxed cool-core clusters such as Virgo, the X-ray surface brightness rises steeply toward the center, tracing a dense and centrally concentrated gas distribution. In contrast, Antlia exhibits a relatively uniform X-ray surface brightness and temperature distribution in its central regions, lacking the strong central peak characteristic of cool-core systems

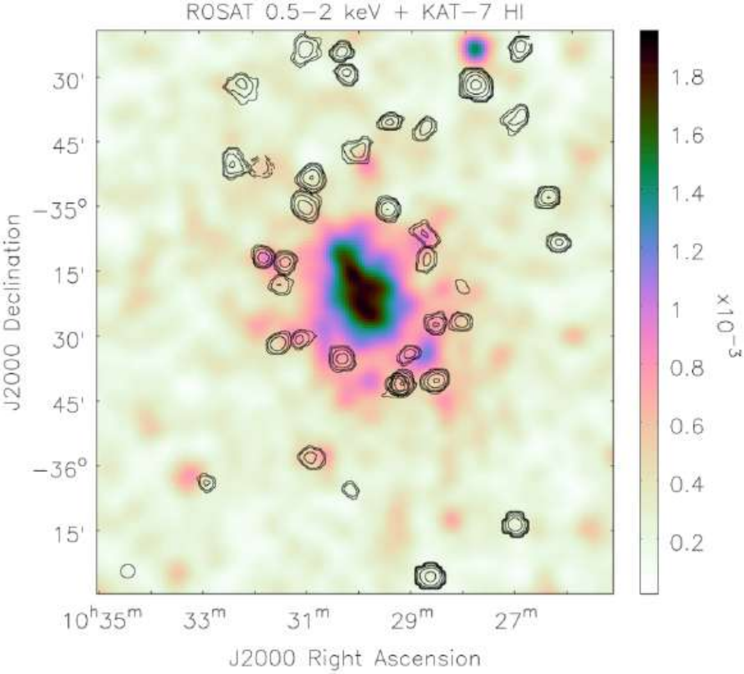

Figure 6.2: ROSAT 0.5–2 keV X-ray image of the Antlia cluster, tracing the hot ICM, overlaid with H I contours from KAT-7 observations (Hess et al., 2015). The X-ray emission is concentrated toward the cluster center, while H I-rich galaxies are predominantly located in the outskirts, illustrating the impact of the cluster environment on the neutral gas content of galaxies.

(Nakazawa et al., 2000; Wong et al., 2016). This indicates that the ICM has not yet settled into a relaxed configuration.

In a system such as Antlia, which is relatively low mass and dynamically disturbed, gravitational interactions may play a particularly important role alongside hydrodynamical processes, enhancing tidal effects in addition to RPS. Together, these conditions create an environment in which multiple mechanisms can act simultaneously on the cold gas component of galaxies.

At the same time, the processes shaping the cold gas component may also transport gas toward the central regions of galaxies. X-ray studies have shown that a fraction of galaxies in Antlia host active galactic nuclei, indicating that gas can still reach the nucleus even within this dynamically evolving environment (Hu et al., 2023). This highlights that, alongside gas removal, mechanisms capable of funneling gas inward may also be operating, linking the environmental transformation of galaxies to the triggering of nuclear activity.

Together, these properties make Antlia a particularly suitable system for studying the cold gas content of galaxies across a range of environments within a single cluster. Its proximity and dynamical state allow the H I distribution to be probed from the outskirts to the inner regions, capturing galaxies at different stages of interaction with the cluster environment. The sensitivity and spatial resolution of the MeerKAT observations enable the detection of both compact and diffuse H I structures, providing a detailed view of the gas distribution across the system.

6.2 NGC 3281

A remarkable example of a galaxy in which multiple evolutionary processes may be acting simultaneously is NGC 3281, located on the north-eastern side of the Antlia cluster, along the axis defined by the Hydra–Antlia filament and the ongoing merger between its two main substructures (see Fig. 6.1). NGC 3281 is an early-type spiral galaxy of morphological type Sab and hosts an AGN classified as a Seyfert 2 system (Phillips et al., 1983; Storchi-Bergmann et al., 1992). It has a stellar mass of $\log_{10}(M_*/M_\odot) \sim 9.6$ (Hess et al., 2015) and an inclination of $i \approx 64^\circ$ (Storchi-Bergmann et al., 1992). The galaxy is located at a projected distance of ~ 430 kpc from the center of the Antlia cluster, corresponding to approximately half of its virial radius.

Although NGC 3281 has been studied primarily in the context of its AGN, its evolution has largely been interpreted from a nuclear perspective. Only recently, with the availability of deep H I observations and the environmental context provided by the Antlia cluster, has it become possible to examine the galaxy as part of a larger system.

NGC 3281 hosts a heavily obscured Seyfert 2 nucleus, with X-ray observations revealing Compton-thick column densities ($N_\mathrm{H} \sim 10^{24}\,\mathrm{cm}^{-2}$) consistent with a deeply embedded central engine (Vignali and Comastri, 2002). Optical observations revealed a prominent biconical ionisation structure extending on kiloparsec scales (Storchi-Bergmann et al., 1992). Radio continuum observations show kpc-scale bipolar outflows roughly perpendicular to the disk, while ALMA CO(2–1) observations reveal molecular gas in the central regions, tracing a multiphase circumnuclear environment, as illustrated in Fig. 6.3 (Dall'Agnol de Oliveira et al., 2023). Previous H I observations by Hess et al. (2015) detected NGC 3281 in absorption against its radio continuum source, tracing neutral gas along the line of sight to the nucleus, while the presence of spatially resolved H I emission remained unclear.

Within the Antlia cluster, H I observations show that neutral gas is largely absent within the central ~ 200 kpc, with detections preferentially located at larger radii (Hess et al., 2015). NGC 3281, located at ~ 430 kpc, lies within this intermediate region where galaxies are expected to be undergoing environmental processing. This makes it an ideal system for studying the impact of the cluster environment on the gas content of cluster galaxies.

The combination of its location within the cluster, its AGN activity, and its observed gas properties makes NGC 3281 a relevant system for examining how internal and external processes may act together in dense environments. In the following which comprise this licentiate thesis, we present the H I properties of NGC 3281 and explore their connection to both its nuclear activity and its surrounding environment.

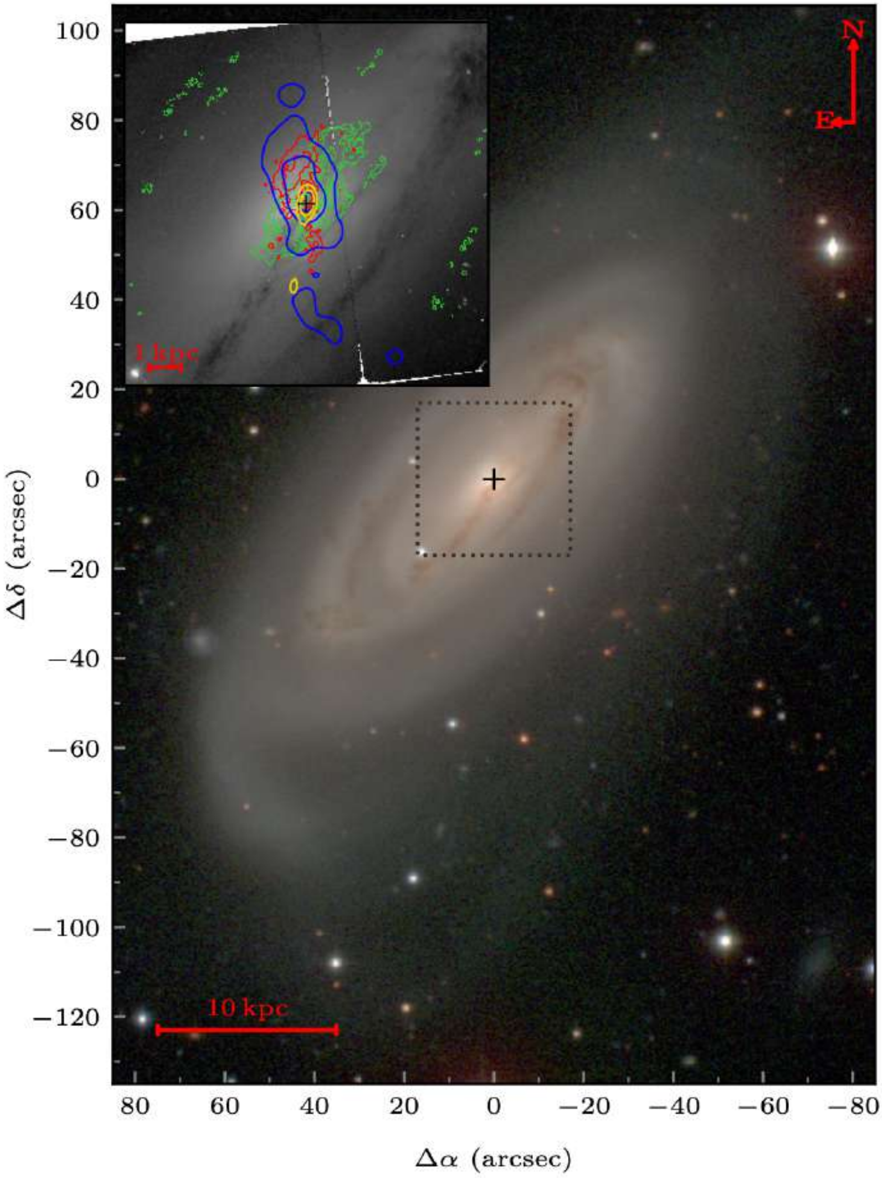

Figure 6.3: Optical image of NGC 3281. The zoomed central region, shown in the upper panel, includes multiwavelength data overlaid: [O III] emission (red), X-ray emission (blue), radio continuum (yellow), and molecular gas traced by CO(2–1) (green) (Dall'Agnol de Oliveira et al., 2023). The cross marks the position of the nucleus.

CHAPTER 7

Summary of included papers

This chapter provides a summary of the included papers.

7.1 Paper A

Vicente Salinas, Kelley M. Hess, Junhyun Baek, Clara C. de la Casa, Ralf Kotulla, S. S. Sridhar, Hao Chen, Aeree Chung, Kana Morokuma-Matsui, Valeria Olivares, Yuanyuan Su, Ming Sun
An environmental view of the galaxy NGC 3281
To be submitted to Monthly Notices of the Royal Astronomical Society (MNRAS) .

References

Hubble, E. (Jan. 1926). “Extra-galactic nebulae”. In: Contrib. Mt. Wilson Obs. 324, pp. 1–49.

Zwicky, F. (Jan. 1933). “Die Rotverschiebung von extragalaktischen Nebeln”. In: Helvetica Physica Acta 6, pp. 110–127.

Hubble, E. (1936). Realm of the Nebulae.

Field, G. B. (Jan. 1958). “Excitation of the Hydrogen 21-CM Line”. In: Proc. IRE 46, pp. 240–250.

de Vaucouleurs, G. (Jan. 1959). “Classification and Morphology of External Galaxies.” In: Handbuch der Physik 53, p. 275.

Ryle, M. and A. Hewish (Jan. 1960). “The synthesis of large radio telescopes”. In: 120, p. 220.

Sandage, A. (1961). The Hubble Atlas of Galaxies.

Schmidt, M. (Mar. 1963). “3C 273 : A Star-Like Object with Large Red-Shift”. In: 197.4872, p. 1040.

Lynden-Bell, D. (Aug. 1969). “Galactic nuclei as collapsed quasars”. In: 223.5207, pp. 690–694.

Roberts, M. S. (July 1970). “The Detection of 21-CENTIMETER Hydrogen Absorption Arising from Within the Radio Galaxy Centaurus a”. In: 161, p. L9.

Gunn, J. E. and J. R. Gott III (Aug. 1972). “On the Infall of Matter Into Clusters of Galaxies and Some Effects on Their Evolution”. In: 176, p. 1.

Toomre, A. and J. Toomre (Dec. 1972). “Galactic Bridges and Tails”. In: 178, pp. 623–666.

Davies, R. D. and B. M. Lewis (Jan. 1973). “Neutral hydrogen in Virgo cluster galaxies.” In: 165, pp. 231–244.

Fanaroff, B. L. and J. M. Riley (May 1974). "The morphology of extragalactic radio sources of high and low luminosity". In: 167, 31P–36P.

Högbom, J. A. (June 1974). "Aperture Synthesis with a Non-Regular Distribution of Interferometer Baselines". In: 15, p. 417.

Khachikian, E. Y. and D. W. Weedman (Sept. 1974). "An atlas of Seyfert galaxies." In: 192, pp. 581–589.

Wolfe, A. M. and G. R. Burbidge (Sept. 1975). "Physical conditions and the location of the absorption-line systems in the QSO 3C 286 and the BL Lacertae object PKS 0735+178." In: 200, pp. 548–557.

Blandford, R. D. and R. L. Znajek (May 1977). "Electromagnetic extraction of energy from Kerr black holes." In: 179, pp. 433–456.

Cowie, L. L. and C. F. McKee (Jan. 1977). "The evaporation of spherical clouds in a hot gas. I. Classical and saturated mass loss rates." In: 211, pp. 135–146.

Cowie, L. L. and A. Songaila (Apr. 1977). "Thermal evaporation of gas within galaxies by a hot intergalactic medium". In: 266, pp. 501–503.

McKee, C. F. and J. P. Ostriker (Nov. 1977). "A theory of the interstellar medium: three components regulated by supernova explosions in an inhomogeneous substrate." In: 218, pp. 148–169.

Blandford, R. D. and M. J. Rees (Mar. 1978). "Extended and compact extragalactic radio sources: interpretation and theory." In: 17, pp. 265–274.

Gallagher, J. S. (July 1978). "Possible optical evidence for ram-pressure-sweeping in the Hydra I cluster of galaxies." In: 223, pp. 386–390.

White, S. D. M. and M. J. Rees (May 1978). "Core condensation in heavy halos: a two-stage theory for galaxy formation and clustering." In: 183, pp. 341–358.

Rybicki, G. B. and A. P. Lightman (1979). Radiative processes in astrophysics.

Dressler, A. (Mar. 1980). "Galaxy morphology in rich clusters: implications for the formation and evolution of galaxies." In: 236, pp. 351–365.

Larson, R. B., B. M. Tinsley, and C. N. Caldwell (May 1980). "The evolution of disk galaxies and the origin of S0 galaxies". In: 237, pp. 692–707.

Ostriker, J. P. (Jan. 1980). "Elliptical Galaxies are not Made by Merging Spiral Galaxies". In: Comments on Astrophysics 8, p. 177.

Peebles, P. J. E. (1980). The large-scale structure of the universe.

Rubin, V. C., W. K. Ford Jr., and N. Thonnard (June 1980). "Rotational properties of 21 SC galaxies with a large range of luminosities and radii, from NGC 4605 (R=4kpc) to UGC 2885 (R=122kpc)." In: 238, pp. 471–487.

Nulsen, P. E. J. (Mar. 1982). “Transport processes and the stripping of cluster galaxies.” In: 198, pp. 1007–1016.

Davies, R. L. et al. (Mar. 1983). “The kinematic properties of faint elliptical galaxies.” In: 266, pp. 41–57.

Merritt, D. (Jan. 1983). “Relaxation and tidal stripping in rich clusters of galaxies. I. Evolution of the mass distribution.” In: 264, pp. 24–48.

Phillips, M. M., P. A. Charles, and J. A. Baldwin (Mar. 1983). “Nearby galaxies with Seyfert-like nuclei.” In: 266, pp. 485–501.

Antonucci, R. R. J. and J. S. Miller (Oct. 1985). “Spectropolarimetry and the nature of NGC 1068.” In: 297, pp. 621–632.

Giovanelli, R. and M. P. Haynes (May 1985). “Gas deficiency in cluster galaxies : a comparison of nine clusters.” In: 292, pp. 404–425.

Sarazin, C. L. (Jan. 1986). “X-ray emission in galaxy clusters”. In: Rev. Mod. Phys. 58.1, pp. 1–115.

Warmels, R. H. (Mar. 1988). “The HI properties of spiral galaxies in the Virgo cluster. III. The HI surface density distribution in 36 galaxies.” In: 72, pp. 427–447.

Kellermann, K. I. et al. (Oct. 1989). “VLA Observations of Objects in the Palomar Bright Quasar Survey”. In: 98, p. 1195.

Shlosman, I., J. Frank, and M. C. Begelman (Mar. 1989). “Bars within bars: a mechanism for fuelling active galactic nuclei”. In: 338.6210, pp. 45–47.

van Gorkom, J. H. et al. (Mar. 1989). “H I Absorption in Radio Elliptical Galaxies—Evidence for Infall”. In: 97, p. 708.

Byrd, G. and M. Valtonen (Feb. 1990). “Tidal Generation of Active Spirals and S0 Galaxies by Rich Clusters”. In: 350, p. 89.

Cayatte, V. et al. (Sept. 1990). “VLA Observations of Neutral Hydrogen in Virgo Cluster Galaxies. I. The Atlas”. In: 100, p. 604.

Barnes, J. E. and L. E. Hernquist (Apr. 1991). “Fueling Starburst Galaxies with Gas-rich Mergers”. In: 370, p. L65.

Barnes, J. E. and L. Hernquist (Jan. 1992). “Dynamics of interacting galaxies.” In: 30, pp. 705–742.

Storchi-Bergmann, T., A. S. Wilson, and J. A. Baldwin (Sept. 1992). “The Ionization Cone, Obscured Nucleus, and Gaseous Outflow in NGC 3281: A Prototypical Seyfert 2 Galaxy?” In: 396, p. 45.

Antonucci, R. (Jan. 1993). “Unified models for active galactic nuclei and quasars.” In: 31, pp. 473–521.

Böhringer, H. et al. (Apr. 1994). "The structure of the Virgo cluster of galaxies from Rosat X-ray images". In: 368.6474, pp. 828–831.

Briggs, D. S. (Dec. 1995). "High Fidelity Interferometric Imaging: Robust Weighting and NNLS Deconvolution". In: AAS Meeting Abstracts. Vol. 187. AAS Meeting Abstracts, 112.02, p. 112.02.

Gavazzi, G. et al. (Dec. 1995). "The radio and optical structure of three peculiar galaxies in A 1367." In: 304, p. 325.

Urry, C. M. and P. Padovani (Sept. 1995). "Unified Schemes for Radio-Loud Active Galactic Nuclei". In: 107, p. 803.

Bond, J. R., L. Kofman, and D. Pogosyan (Apr. 1996). "How filaments of galaxies are woven into the cosmic web". In: 380.6575, pp. 603–606.

Mihos, J. C. and L. Hernquist (June 1996). "Gasdynamics and Starbursts in Major Mergers". In: 464, p. 641.

Moore, B. et al. (Feb. 1996). "Galaxy harassment and the evolution of clusters of galaxies". In: 379.6566, pp. 613–616.

Solanes, J. M., R. Giovanelli, and M. P. Haynes (Apr. 1996). "The H i Content of Spirals. I. Field Galaxy H i Mass Functions and H i Mass–Optical Size Regressions". In: 461, p. 609.

Broeils, A. H. and M.-H. Rhee (Aug. 1997). "Short 21-cm WSRT observations of spiral and irregular galaxies. HI properties." In: 324, pp. 877–887.

Ho, L. C., A. V. Filippenko, and W. L. W. Sargent (Oct. 1997). "A Search for "Dwarf" Seyfert Nuclei. III. Spectroscopic Parameters and Properties of the Host Galaxies". In: 112.2, pp. 315–390.

Makino, J. and P. Hut (May 1997). "Merger Rate of Equal-Mass Spherical Galaxies". In: 481.1, pp. 83–94.

Kennicutt Jr., R. C. (May 1998). "The Global Schmidt Law in Star-forming Galaxies". In: 498.2, pp. 541–552.

Moore, B., G. Lake, and N. Katz (Mar. 1998). "Morphological Transformation from Galaxy Harassment". In: 495.1, pp. 139–151.

Silk, J. and M. J. Rees (Mar. 1998). "Quasars and galaxy formation". In: 331, pp. L1–L4.

Nakazawa, K. et al. (Aug. 2000). "ASCA Observations of a Near-by Cluster in Antlia". In: 52, pp. 623–630.

Morganti, R. et al. (Jan. 2001). "H I absorption in the central kpc of radio galaxies". In: The Central Kiloparsec of Starbursts and AGN. Ed. by J. H. Knapen et al. Vol. 249. ASP Conf. Ser. P. 632.

Solanes, J. M. et al. (Feb. 2001). "The H I Content of Spirals. II. Gas Deficiency in Cluster Galaxies". In: 548.1, pp. 97–113.

Strateva, I. et al. (Oct. 2001). "Color Separation of Galaxy Types in the Sloan Digital Sky Survey Imaging Data". In: 122.4, pp. 1861–1874.

Vignali, C. and A. Comastri (Jan. 2002). "Disclosing the true nature of the Sy 2 galaxy NGC 3281: One more Compton-thick source". In: 381, pp. 834–840.

Burkert, A. and T. Naab (2003). "Major Mergers and the Origin of Elliptical Galaxies". In: Galaxies and Chaos. Ed. by G. Contopoulos and N. Voglis. Vol. 626, pp. 327–339.

Crenshaw, D. M., S. B. Kraemer, and I. M. George (Jan. 2003). "Mass Loss from the Nuclei of Active Galaxies". In: 41, pp. 117–167.

Vermeulen, R. C. et al. (June 2003). "Observations of H I absorbing gas in compact radio sources at cosmological redshifts". In: 404, pp. 861–870.

Fujita, Y. (Feb. 2004). "Pre-Processing of Galaxies before Entering a Cluster". In: 56, pp. 29–43.

Lin, Y.-T. and J. J. Mohr (Dec. 2004). "K-band Properties of Galaxy Clusters and Groups: Brightest Cluster Galaxies and Intracluster Light". In: 617.2, pp. 879–895.

Meyer, M. J. et al. (June 2004). "The HIPASS catalogue - I. Data presentation". In: 350.4, pp. 1195–1209.

Schaye, J. (July 2004). "Star Formation Thresholds and Galaxy Edges: Why and Where". In: 609.2, pp. 667–682.

Croston, J. H. et al. (Apr. 2005). "Jet/Environment Interactions of FRI and FRII Radio Galaxies". In: X-Ray and Radio Connections. Ed. by L. O. Sjouwerman and K. K. Dyer, 7.06, p. 7.06.

Oosterloo, T. and J. van Gorkom (July 2005). "A large H I cloud near the centre of the Virgo cluster". In: 437.1, pp. L19–L22.

Springel, V. et al. (June 2005). "Simulations of the formation, evolution and clustering of galaxies and quasars". In: 435.7042, pp. 629–636.

Veilleux, S., G. Cecil, and J. Bland-Hawthorn (Sept. 2005). "Galactic Winds". In: 43.1, pp. 769–826.

Boselli, A. and G. Gavazzi (Apr. 2006). "Environmental Effects on Late-Type Galaxies in Nearby Clusters". In: 118.842, pp. 517–559.

Clowe, D. et al. (Sept. 2006). "A Direct Empirical Proof of the Existence of Dark Matter". In: 648.2, pp. L109–L113.

Mayer, L. et al. (July 2006). “Simultaneous ram pressure and tidal stripping; how dwarf spheroidals lost their gas”. In: 369.3, pp. 1021–1038.

Skrutskie, M. F. et al. (Feb. 2006). “The Two Micron All Sky Survey (2MASS)”. In: 131.2, pp. 1163–1183.

Vikhlinin, A. et al. (Apr. 2006). “Chandra Sample of Nearby Relaxed Galaxy Clusters: Mass, Gas Fraction, and Mass-Temperature Relation”. In: 640.2, pp. 691–709.

Gonzalez, A. H., D. Zaritsky, and A. I. Zabludoff (Sept. 2007). “A Census of Baryons in Galaxy Clusters and Groups”. In: 666.1, pp. 147–155.

Markevitch, M. and A. Vikhlinin (May 2007). “Shocks and cold fronts in galaxy clusters”. In: 443.1, pp. 1–53.

Binney, J. and S. Tremaine (2008). Galactic Dynamics: Second Edition.

Ghez, A. M. et al. (Dec. 2008). “Measuring Distance and Properties of the Milky Way’s Central Supermassive Black Hole with Stellar Orbits”. In: 689.2, pp. 1044–1062.

Krumholz, M. R., C. F. McKee, and J. Tumlinson (Dec. 2008). “The Atomic-to-Molecular Transition in Galaxies. I. An Analytic Approximation for Photodissociation Fronts in Finite Clouds”. In: 689.2, pp. 865–882.

Morganti, R. et al. (July 2008). “A circumnuclear disk of atomic hydrogen in Centaurus A”. In: 485.2, pp. L5–L8.

Tacconi, L. J. et al. (June 2008). “Submillimeter Galaxies at z $\sim$2: Evidence for Major Mergers and Constraints on Lifetimes, IMF, and CO-H_2 Conversion Factor”. In: 680.1, pp. 246–262.

Walter, F. et al. (Dec. 2008). “THINGS: The H I Nearby Galaxy Survey”. In: 136.6, pp. 2563–2647.

Blanton, M. R. and J. Moustakas (Sept. 2009). “Physical Properties and Environments of Nearby Galaxies”. In: 47.1, pp. 159–210.

Boselli, A. and G. Gavazzi (Dec. 2009). “The HI properties of galaxies in the Coma I cloud revisited”. In: 508.1, pp. 201–207.

Chung, A. et al. (Dec. 2009). “VLA Imaging of Virgo Spirals in Atomic Gas (VIVA). I. The Atlas and the H I Properties”. In: 138.6, pp. 1741–1816.

Krumholz, M. R., C. F. McKee, and J. Tumlinson (Mar. 2009). “The Atomic-to-Molecular Transition in Galaxies. II: H I and H_2 Column Densities”. In: 693.1, pp. 216–235.

Aragón-Calvo, M. A., R. van de Weygaert, and B. J. T. Jones (Nov. 2010). “Multiscale phenomenology of the cosmic web”. In: 408.4, pp. 2163–2187.

Feruglio, C. et al. (July 2010). “Quasar feedback revealed by giant molecular outflows”. In: 518, L155, p. L155.

Hopkins, P. F. and E. Quataert (Sept. 2010). “How do massive black holes get their gas?” In: 407.3, pp. 1529–1564.

Mo, H., F. C. van den Bosch, and S. White (2010). Galaxy Formation and Evolution.

Peng, Y.-j. et al. (Sept. 2010). “Mass and Environment as Drivers of Galaxy Evolution in SDSS and zCOSMOS and the Origin of the Schechter Function”. In: 721.1, pp. 193–221.

Tombesi, F. et al. (Oct. 2010). “Evidence for ultra-fast outflows in radio-quiet AGNs. I. Detection and statistical incidence of Fe K-shell absorption lines”. In: 521, A57, A57.

Allen, S. W., A. E. Evrard, and A. B. Mantz (Sept. 2011). “Cosmological Parameters from Observations of Galaxy Clusters”. In: 49.1, pp. 409–470.

Fabian, A. C. (Sept. 2012). “Observational Evidence of Active Galactic Nuclei Feedback”. In: 50, pp. 455–489.

Haines, C. P. et al. (Aug. 2012). “LoCuSS: A Dynamical Analysis of X-Ray Active Galactic Nuclei in Local Clusters”. In: 754.2, 97, p. 97.

Kravtsov, A. V. and S. Borgani (Sept. 2012). “Formation of Galaxy Clusters”. In: 50, pp. 353–409.

Smith, R., M. Fellhauer, and P. Assmann (Mar. 2012). “Ram pressure drag - the effects of ram pressure on dark matter and stellar disc dynamics”. In: 420.3, pp. 1990–2005.

Struve, C. and J. E. Conway (Oct. 2012). “The circumnuclear cold gas environments of the powerful radio galaxies 3C 236 and 4C 31.04”. In: 546, A22, A22.

Bolatto, A. D., M. Wolfire, and A. K. Leroy (Aug. 2013). “The CO-to-H_2 Conversion Factor”. In: 51.1, pp. 207–268.

Kormendy, J. and L. C. Ho (Aug. 2013). “Coevolution (Or Not) of Supermassive Black Holes and Host Galaxies”. In: 51.1, pp. 511–653.

Freundlich, J. et al. (Dec. 2014). “High-redshift star formation efficiency as uncovered by the IRAM PHIBSS programs”. In: SF2A-2014. Ed. by J. Ballet et al., pp. 387–390.

Heckman, T. M. and P. N. Best (Aug. 2014). “The Coevolution of Galaxies and Supermassive Black Holes: Insights from Surveys of the Contemporary Universe”. In: 52, pp. 589–660.

Offringa, A. R. et al. (Oct. 2014). “WSCLEAN: an implementation of a fast, generic wide-field imager for radio astronomy”. In: 444.1, pp. 606–619.

Planck Collaboration et al. (Nov. 2014). “Planck 2013 results. XIII. Galactic CO emission”. In: 571, A13, A13.

Hess, K. M. et al. (Sept. 2015). “KAT-7 science verification: cold gas, star formation, and substructure in the nearby Antlia Cluster”. In: 452.2, pp. 1617–1636.

Jaffé, Y. L. et al. (Apr. 2015). “BUDHIES II: a phase-space view of H I gas stripping and star formation quenching in cluster galaxies”. In: 448.2, pp. 1715–1728.

King, A. and K. Pounds (Aug. 2015). “Powerful Outflows and Feedback from Active Galactic Nuclei”. In: 53, pp. 115–154.

Serra, P. et al. (Apr. 2015). “SOFIA: a flexible source finder for 3D spectral line data”. In: 448.2, pp. 1922–1929.

Somerville, R. S. and R. Davé (Aug. 2015). “Physical Models of Galaxy Formation in a Cosmological Framework”. In: 53, pp. 51–113.

HI4PI Collaboration et al. (Oct. 2016). “HI4PI: A full-sky H I survey based on EBHIS and GASS”. In: 594, A116, A116.

Jaffé, Y. L. et al. (Sept. 2016). “BUDHIES - III: the fate of H I and the quenching of galaxies in evolving environments”. In: 461.2, pp. 1202–1221.

Poggianti, B. M. et al. (Mar. 2016). “Jellyfish Galaxy Candidates at Low Redshift”. In: 151.3, 78, p. 78.

Wang, J. et al. (Aug. 2016). “New lessons from the H I size-mass relation of galaxies”. In: 460.2, pp. 2143–2151.

Wong, K.-W. et al. (Sept. 2016). “Suzaku X-ray Observations of the Nearest Non-Cool Core Cluster, Antlia: Dynamically Young but with Remarkably Relaxed Outskirts”. In: 829.1, 49, p. 49.

Bellhouse, C. et al. (July 2017). “GASP. II. A MUSE View of Extreme Ram-Pressure Stripping along the Line of Sight: Kinematics of the Jellyfish Galaxy JO201”. In: 844.1, 49, p. 49.

Cava, A. et al. (Oct. 2017). “Structural and dynamical modeling of WINGS clusters. I. The distribution of cluster galaxies of different morphological classes within regular and irregular clusters”. In: 606, A108, A108.

Maccagni, F. M. et al. (Aug. 2017). “Kinematics and physical conditions of H I in nearby radio sources. The last survey of the old Westerbork Synthesis Radio Telescope”. In: 604, A43, A43.

Meyer, M. et al. (Nov. 2017). “Tracing HI Beyond the Local Universe”. In: 34, p. 52.

Noble, A. G. et al. (June 2017). “ALMA Observations of Gas-rich Galaxies in $z \sim 1.6$ Galaxy Clusters: Evidence for Higher Gas Fractions in High-density Environments”. In: 842.2, L21, p. L21.

Padovani, P. et al. (Aug. 2017). “Active galactic nuclei: what’s in a name?” In: 25.1, 2, p. 2.

Poggianti, B. M. et al. (July 2017). “GASP. I. Gas Stripping Phenomena in Galaxies with MUSE”. In: 844.1, 48, p. 48.

Rhee, J. et al. (July 2017). “Phase-space Analysis in the Group and Cluster Environment: Time Since Infall and Tidal Mass Loss”. In: 843.2, 128, p. 128.

Saintonge, A. et al. (Dec. 2017). “xCOLD GASS: The Complete IRAM 30 m Legacy Survey of Molecular Gas for Galaxy Evolution Studies”. In: 233.2, 22, p. 22.

Stroe, A. et al. (Mar. 2017). “A large Hα survey of star formation in relaxed and merging galaxy cluster environments at z $\sim$ 0.15-0.3”. In: 465.3, pp. 2916–2935.

Yoon, H. et al. (Apr. 2017). “A History of H I Stripping in Virgo: A Phase-space View of VIVA Galaxies”. In: 838.2, 81, p. 81.

Zasov, A. V. et al. (Apr. 2017). “Dark matter in galaxies”. In: Physics Uspekhi 60.1, p. 3.

Jaffé, Y. L. et al. (June 2018). “GASP. IX. Jellyfish galaxies in phase-space: an orbital study of intense ram-pressure stripping in clusters”. In: 476.4, pp. 4753–4764.

Kalberla, P. M. W. and U. Haud (Nov. 2018). “Properties of cold and warm H I gas phases derived from a Gaussian decomposition of HI4PI data”. In: 619, A58, A58.

Loomis, R. A. et al. (Apr. 2018). “Detecting Weak Spectral Lines in Interferometric Data through Matched Filtering”. In: 155.4, 182, p. 182.

Wang, Y. et al. (Feb. 2020). “The HI/OH/Recombination line survey of the inner Milky Way (THOR): data release 2 and H I overview”. In: 634, A83, A83.

Cortese, L., B. Catinella, and R. Smith (Aug. 2021). “The Dawes Review 9: The role of cold gas stripping on the star formation quenching of satellite galaxies”. In: 38, e035, e035.

Kleiner, D. et al. (Apr. 2021). “A MeerKAT view of pre-processing in the Fornax A group”. In: 648, A32, A32.

Predehl, P. et al. (Mar. 2021). “The eROSITA X-ray telescope on SRG”. In: 647, A1, A1.

Westmeier, T. et al. (Sept. 2021). “SOFIA 2 - an automated, parallel H I source finding pipeline for the WALLABY survey”. In: 506.3, pp. 3962–3976.

Dutta, R. and R. Srianand (Nov. 2022). “H I 21-cm absorption in radio-loud AGN with double-peaked [O III] emission”. In: 516.3, pp. 4338–4345.

Maier, C., C. P. Haines, and B. L. Ziegler (Feb. 2022). “Star-formation quenching of cluster galaxies as traced by metallicity and presence of active galactic nuclei, and galactic conformity”. In: 658, A190, A190.

Peluso, G. et al. (July 2022). "Exploring the AGN-Ram pressure stripping connection in local clusters". In: 44th COSPAR Scientific Assembly. Held 16-24 July. Vol. 44, p. 2336.

Saintonge, A. and B. Catinella (Aug. 2022). "The Cold Interstellar Medium of Galaxies in the Local Universe". In: 60, pp. 319–361.

Smith, R. et al. (July 2022). "A New Method to Constrain the Appearance and Disappearance of Observed Jellyfish Galaxy Tails". In: 934.1, 86, p. 86.

Vulcani, B. et al. (Mar. 2022). "The Relevance of Ram Pressure Stripping for the Evolution of Blue Cluster Galaxies as Seen at Optical Wavelengths". In: 927.1, 91, p. 91.

Dall'Agnol de Oliveira, B. et al. (July 2023). "Cold molecular gas outflow encasing the ionized one in the Seyfert galaxy NGC 3281". In: 522.3, pp. 3753–3765.

Gullieuszik, M. et al. (Mar. 2023). "UV and Hα HST Observations of Six GASP Jellyfish Galaxies". In: 945.1, 54, p. 54.

Hu, Z. et al. (Oct. 2023). "AMUSE-Antlia. I. Nuclear X-Ray Properties of Early-type Galaxies in a Dynamically Young Galaxy Cluster". In: 956.2, 104, p. 104.

Marasco, A. et al. (Nov. 2023). "The morphological transformation of ram pressure stripped galaxies: a pathway from late to early galaxy types". In: 525.4, pp. 5359–5377.

Serra, P. et al. (May 2023). "The MeerKAT Fornax Survey. I. Survey description and first evidence of ram pressure in the Fornax galaxy cluster". In: 673, A146, A146.

de Blok, W. J. G. et al. (Aug. 2024). "MHONGOOSE: A MeerKAT nearby galaxy H I survey". In: 688, A109, A109.

Deka, P. P. et al. (Feb. 2024). "The MeerKAT Absorption Line Survey (MALS) Data Release. I. Stokes I Image Catalogs at 11.4 GHz". In: 270.2, 33, p. 33.

O'Kane, C. J. et al. (Nov. 2024). "The effect of cosmic web filaments on galaxy evolution". In: 534.3, pp. 1682–1699.

Salinas, V. et al. (Sept. 2024). "Constraining the duration of ram pressure stripping features in the optical from the direction of jellyfish galaxy tails". In: 533.1, pp. 341–359.

de la Casa, C. C. et al. (Dec. 2025). "Starburst galaxies in the Hydra I cluster". In: 704, A264, A264.

Smith, R. et al. (Sept. 2025). "Distinguishing ram pressure from tidal interactions: Size-shape difference measure". In: 701, A6, A6.

Yoon, H. et al. (June 2025). "The first large absorption survey in H I (FLASH): II. Pilot survey data release and first results". In: 42, e088, e088.

Part II

Publications

PAPER A

An environmental view of the galaxy NGC 3281

Vicente Salinas, Kelley M. Hess, Junhyun Baek, Clara C. de la Casa, Ralf Kotulla,
S. S. Sridhar, Hao Chen, Aeree Chung, Kana Morokuma-Matsui, Valeria Olivares,
Yuanyuan Su, Ming Sun

To be submitted to Monthly Notices of the Royal Astronomical Society (MNRAS)

The layout has been revised.

MNRAS **000**, 1–15 (2024) Preprint 18 May 2026 Compiled using MNRAS LATEX style file v3.0

An environmental view of the galaxy NGC 3281

Vicente Salinas[1], Kelley M. Hess[1], Junhyun Baek[2], Clara C. de la Casa[3], Ralf Kotulla[4], S. S. Sridhar[5], Hao Chen[6], Aeree Chung[7], Kana Morokuma[8], Valeria Olivares[9], Yuanyuan Su[10], Ming Sun[11]

[1]*Department of Physics and Astronomy, Chalmers University of Technology, Onsala Space Observatory, SE-439 92 Onsala, Sweden*
[2]*Korea Astronomy and Space Science Institute, 776 Daedeok-daero, Yuseong-gu, Daejeon 34055, Republic of Korea*
[3]*Instituto de Astrofísica de Andalucía (CSIC), Glorieta de la Astronomía s/n, 18008 Granada, Spain*
[4]*Department of Astronomy, University of Wisconsin-Madison, 475 N Charter St, Madison, WI 53706, USA*
[5]*SKA Observatory, Jodrell Bank, Lower Withington, Macclesfield, SK11 9FT, United Kingdom*
[6]*Research Center for Computational Earth and Space Science, Zhejiang Laboratory, Hangzhou 311121, China*
[7]*Department of Astronomy, Yonsei University, 50 Yonsei-ro, Seodaemun-gu, Seoul 03722, Republic of Korea*
[8]*Institute of Astronomy, Graduate School of Science, The University of Tokyo, 2-21-1 Osawa, Mitaka, Tokyo 181-0015, Japan*
[9]*Departamento de Física, Universidad de Santiago de Chile, Av. Victor Jara 3659, Santiago 9170124, Chile*
[10]*Department of Physics and Astronomy, University of Kentucky, 505 Rose Street, Lexington, KY 40506, USA*
[11]*Department of Physics & Astronomy, University of Alabama in Huntsville, 301 Sparkman Dr NW, Huntsville, AL 35899, USA*

Accepted XXX. Received YYY; in original form ZZZ

ABSTRACT

Neutral atomic hydrogen (H i) provides the gas reservoir that fuels star formation. Environmental mechanisms in galaxy clusters alter the fate of this gas, thereby influencing galaxy evolution. These mechanisms range from gravitational interactions to hydrodynamical effects, which can ignite or enhance internal processes such as AGN activity. The current picture of cluster galaxy evolution is thus shaped by a complex interplay of these factors. We present an environmental study of the Seyfert 2 galaxy NGC 3281 in the Antlia cluster using deep MeerKAT H i and radio continuum observations, complemented by deep optical imaging. NGC 3281 hosts a truncated H i disk and is missing $\sim 81^{+12}_{-29}\%$ of its expected H i mass. We report the discovery of an isolated, large, starless H i cloud extending up to ∼ 200 kpc from NGC 3281 while carrying the kinematic signature of the galaxy's rotation. Together with two smaller nearby H i clouds, this material accounts for $\sim 18^{+25}_{-9}\%$ of the inferred missing H i. The H i morphology and distribution indicate ram pressure stripping as the dominant mechanism shaping the gas, while the complete detachment of the cloud and faint stellar features suggest that a past weak gravitational interaction contributed to loosening the gas reservoir. We estimate that the main H i cloud was stripped from the galaxy ∼ 300–350 Myr ago. We detect strong redshifted H i absorption consistent with ongoing cold gas inflow, and the radio continuum emission reveals kpc-scale bipolar outflows emerging from the nucleus. NGC 3281, therefore, represents one of the clearest nearby examples of a galaxy undergoing multiple simultaneous evolutionary processes.

Key words: galaxies: clusters: general – galaxies: clusters: intracluster medium – galaxies: evolution

1 INTRODUCTION

1.1 Environmental processes, H i, and AGN activity in clusters

It has been well established that the evolution of galaxies is greatly impacted by their environment (e.g. Davies & Lewis 1973; Dressler 1980; Kennicutt 1983; Giovanelli & Haynes 1985; Whitmore et al. 1993; Solanes et al. 2001; Baldry et al. 2006; Gavazzi et al. 2010; Peng et al. 2010). As the densest large-scale structures in the universe, galaxy clusters host the most extreme conditions for galaxy evolution. They serve as nodes in the cosmic web, where hundreds to thousands of galaxies converge, leading to gravitational interactions with other galaxies and the cluster potential, as well as effects driven by the interaction between the hot intracluster medium (ICM) and the interstellar medium (ISM). While these processes can temporarily enhance star formation (e.g. Kennicutt et al. 1987; Gavazzi et al. 1995; de la Casa et al. 2025), the end result that we observe is that galaxies in clusters experience a halt of their star formation compared to isolated galaxies of similar mass in the field (Boselli & Gavazzi 2014; Jaffé et al. 2016).

Physical mechanisms driving galaxy evolution are often divided into two broad categories: internal and external factors. On the one hand, internal processes occur naturally as a result of a galaxy's own processes, such as gravitational instabilities, active galactic nuclei (AGN) feedback, or supernova feedback. On the other hand, external factors are caused by the interaction between a galaxy and its environment, and become increasingly more prominent in denser environments. These are further classified into gravitational effects, such as mergers, tidal interactions, and harassment (Spitzer & Baade 1951; Merritt 1983; Moore et al. 1998), and hydrodynamical effects, including ram pressure stripping (RPS), thermal evaporation and viscous stripping (Gunn & Gott 1972; Cowie & Songaila 1977; Nulsen 1982).

Among the internal processes, AGN have been found to play an important role in a galaxy's evolution (Fabian 2012). These are powered by the accretion of material onto a supermassive black hole (SMBH), located at the center of galaxies (Rees 1984; Kormendy & Ho 2013). As a consequence of the accretion process, large amounts of energy are released outward into the ISM and the ICM (Silk & Rees 1998), often observable in the form of radio continuum outflows and jets (e.g. Blandford & Rees 1974). These can disturb the cold gas reservoir in a galaxy by heating or pushing the gas, thereby lowering the efficiency of star formation (Harrison 2017; Fiore et al. 2017; Nesvadba et al. 2021).

In this context, neutral atomic hydrogen (H I) provides a key tracer for studying how the cold gas reservoir in a galaxy is affected. In AGN host galaxies, H I outflows can be detected as blueshifted absorption against an underlying continuum (Morganti et al. 1998), while redshifted H I absorption can be a sign of inflow (e.g. Maccagni et al. 2017). More generally, H I emission provides a large scale view of the remaining cold gas distribution in a galaxy. As the least bound component of the ISM, H I can be easily stripped by gravitational interactions or RPS, making it highly sensitive to environmental effects.

Gravitational interactions between galaxies or with the cluster potential can alter multiple components in a galaxy, including both the stellar and gaseous components. This can completely change the morphology of a galaxy, often producing asymmetric features such as tidal tails, bridges, or disturbed gas kinematics (Toomre & Toomre 1972; Hibbard & van Gorkom 1996; Reynolds et al. 2020; Hank et al. 2025). In contrast, RPS primarily affects the gaseous component, typically producing one-sided features and an outside-in truncation of the neutral gas (Warmels 1988; Cayatte et al. 1990; Chung et al. 2009; Hess et al. 2022).

In the current picture of galaxy evolution in clusters (see Boselli & Gavazzi 2006; Cortese et al. 2021 for a review), all these mechanisms rarely act independently. Rather, what we observe is a combination of multiple effects happening simultaneously and potentially altering the effectiveness of each individual process. For instance, simulations by Mayer et al. (2006) show how tidal forces can weaken the gravitational potential, causing the gas in a galaxy to be more easily stripped by RPS. Tidal interactions and RPS are frequently expected to occur together in dense environments, which can make their combined signatures difficult to disentangle. This challenge is addressed with simulated samples in Smith et al. (2025), who demonstrate that their diagnostic becomes even more sensitive to detecting RPS when it occurs simultaneously with tidal interactions.

Many observational examples of gravitational and hydrodynamical processes acting together have also been found, such as in the Virgo cluster (Oosterloo & van Gorkom 2005) and in the Fornax cluster (Kleiner et al. 2021; Serra et al. 2023, 2024). These examples often show a clear one sided H I tail or extended H I cloud, together with signatures of a gravitational interaction, such as disturbed old stellar features or unusual velocity gradients. In Serra et al. (2023) they argue that tidal forces were a necessary step for RPS to be able to further displace the H I, given the relatively weak ram pressure in the Fornax cluster.

With the new generation of radio interferometers, sensitive H I observations are revealing increasingly low column density gas in clusters without an obvious optical counterpart (e.g. Koopmann 2008; Serra et al. 2013; Hess et al. 2015; Kleiner et al. 2021; Józsa et al. 2022). Such "clouds" of H I are often interpreted as the result of gas stripped from nearby galaxies. Recent simulations by Chaturvedi et al. (2024) tailored to MeerKAT (Jonas & MeerKAT Team 2016) sensitivities in Fornax-like clusters show a significant population of low column density H I clouds extending hundreds of kiloparsecs (~ 350 kpc on average) from the cluster galaxies into the ICM. Their study suggests these clouds are associated with stripped gas from satellite galaxies. However, the survival timescales of these clouds within the ICM remain uncertain, and could provide useful constraints on the physical processes governing gas stripping in cluster environments.

Another not fully understood connection is the extent to which environmental effects can influence nuclear activity. Conflicting results have been reported in the literature, with some claiming that the fraction of AGN in cluster galaxies is lower than that of the field (e.g. Dressler et al. 1985; Haines et al. 2012; Lopes et al. 2017), while others claim the fractions are comparable (e.g. Martini et al. 2007; von der Linden et al. 2010). Tidal interactions are known to efficiently drive inflows of gas toward the SMBH, and are therefore a well-established mechanism for triggering AGN activity (e.g. Shlosman et al. 1989; Byrd & Valtonen 1990; Di Matteo et al. 2005; Hopkins & Quataert 2010; Avirett-Mackenzie et al. 2024; Vásquez-Bustos et al. 2025). In this regard, galaxy-galaxy interactions would be more common in smaller groups rather than big galaxy clusters since merger rates are suppressed in high velocity dispersion environments (Ostriker 1980; Makino & Hut 1997). As a consequence, AGN activity may be preferentially associated with pre-processed galaxies in group environments prior to accretion into the cluster.

In contrast, the impact of RPS on nuclear activity remains more uncertain. While RPS can remove the gas that could feed the AGN, some studies suggest it may briefly enhance accretion during the peak of the stripping process (Poggianti et al. 2017; Peluso et al. 2022). According to Gunn & Gott (1972) formalism, RPS is more efficient when a galaxy moves fast and through a dense medium. Phase-space diagrams have shown these conditions occur preferentially for recently infalling galaxies (Rhee et al. 2017; Jaffé et al. 2018). Consistent with this picture, it has been shown that AGN in clusters are most likely to be found in the infalling region, rather than the virialized core (Haines et al. 2012; Maier et al. 2022).

1.2 The Antlia cluster

To shed light on some of these questions and explore these processes in detail, we focus on the nearby Antlia galaxy cluster. Antlia provides an environment to study galaxies in a dynamically young, low-mass, and unrelaxed cluster with a virial radius of ~ 887 kpc (Wong et al. 2016). It is located south-west of the Hydra cluster and is connected to it by a large scale structure filament. The cluster is composed of two groups centered on NGC 3258 and NGC 3268 that are in the process of merging along the same direction as the filament linking Antlia and Hydra, making Antlia a compelling system for studying infalling galaxies in the early stages of cluster assembly (Smith Castelli et al. 2008). Its proximity further enables detailed, well-resolved studies of the H I distribution in galaxies and their surroundings.

The dynamical state of the cluster is reflected in the properties of its ICM. Unlike relaxed cool-core clusters, Antlia exhibits a relatively uniform X-ray surface brightness distribution in its central regions, lacking the strong central peak characteristic of cool-core systems (Nakazawa et al. 2000; Wong et al. 2016). In such an environment, both hydrodynamical and gravitational processes are favoured and can strongly influence the cold gas component of galaxies. These processes may not only remove or redistribute gas, but also influence its transport toward the central regions of galaxies. Furthermore, Hu et al. (2023) find enhanced AGN activity in Antlia compared to more relaxed nearby clusters such as Virgo and Fornax, consistent with its dynamically young and merging state.

The H i study by Hess et al. (2015) (hereafter H15) shows that gas-rich galaxies in Antlia preferentially avoid the central region, with H i detections predominantly found at larger cluster-centric radii, based on the sensitivity limits of the available KAT-7 observations at the time. The MeerKAT observations used in this work, with substantially improved sensitivity and angular resolution, are part of a broader effort aimed at characterising the H i properties of galaxies and H i gas throughout the Antlia cluster, which will be presented in future studies.

1.3 NGC 3281

In this paper, we focus specifically on the environmentally affected spiral galaxy NGC 3281 and its immediate surroundings, using this system as a detailed case study to investigate the interplay between environmental effects and nuclear activity. NGC 3281 is a well-known Seyfert 2 galaxy (Phillips et al. 1983; Storchi-Bergmann et al. 1992) and hosts extended radio continuum emission (Liu et al. 2025). This makes it a particularly suitable target for studies of neutral gas in absorption and emission. The previous H i observations by H15 revealed both absorption against the central radio continuum and a nearby extended H i structure, motivating the detailed MeerKAT investigation of NGC 3281 and its surroundings presented in this work.

NGC 3281 is an early-type spiral galaxy of morphological type Sab (Winter et al. 2009). An inclination of $i \simeq 64°$ is commonly adopted in the literature for NGC 3281 (e.g. Storchi-Bergmann et al. 1992). With a stellar mass of order $M_* \sim 10^{9.5}\,M_\odot$ (H15), it is a moderately massive disk galaxy. It is located at a projected distance of ~ 430 kpc north-east of the centre of the Antlia cluster, roughly at half its virial radius, along the same direction as the filament connecting Antlia to the Hydra cluster and the merging axis of the two Antlia subgroups. Its projected location within the Antlia cluster therefore makes NGC 3281 a plausible candidate for a recently infalling galaxy.

NGC 3281 has been extensively studied in the context of its AGN, most notably by Storchi-Bergmann et al. (1992), who identified a heavily obscured Seyfert 2 nucleus and a prominent biconical ionisation structure extending on kiloparsec scales. Subsequent infrared and X-ray studies have shown that the nucleus of NGC 3281 is extremely obscured, with column densities in the Compton-thick regime and one of the deepest silicate absorption features observed among Seyfert galaxies, consistent with the presence of a compact dusty torus (Sales et al. 2011). Recent ALMA CO(2–1) observations by Dall'Agnol de Oliveira et al. (2023) (hereafter D23) have revealed the presence of cold molecular gas outflows encasing the ionised biconical structure, highlighting the multi-phase nature of AGN-driven outflows in NGC 3281.

Despite this extensive work on the nuclear properties of NGC 3281, the galactic disk and its environmental evolution within the Antlia cluster has received little attention. In particular, the connection between its AGN outflows and the large-scale distribution of neutral gas in its surroundings remains unexplored. While H15 reported extended H i in the vicinity of NGC 3281, and D23 noted optical features suggestive of a past gravitational perturbation, the origin of the surrounding neutral gas could not be assessed with previous data. With this study, we combine deep MeerKAT H i and radio continuum observations with DECam optical imaging to investigate the neutral gas environment of NGC 3281 and assess the role of environmental processes in shaping its present-day state and their connection to its AGN activity.

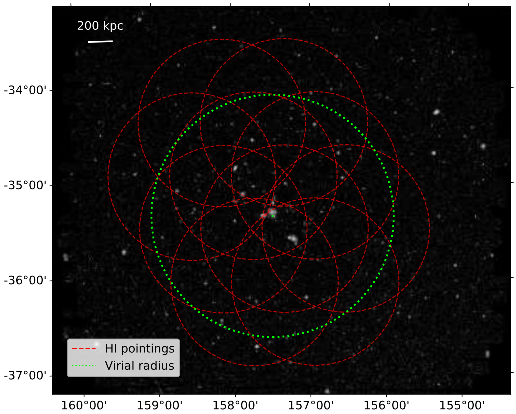

Figure 1. Optical DECam image of the Antlia cluster in the r-band, overlaid with the MeerKAT coverage. Red dashed circles indicate the edges of the 10 pointings down to the 10% sensitivity level. The green dotted circle represents the virial radius, and the cross marks the cluster center.

Throughout this paper we assume a ΛCDM cosmology, with a Hubble constant $H_0 = 73$ km s^{-1} Mpc^{-1}, present matter density of $\Omega_m = 0.27$, and dark energy density $\Omega_\Lambda = 0.73$. We adopt a cluster redshift of $z = 0.00933$, corresponding to a heliocentric velocity of $v_{\rm hel} = 2797$ km s^{-1} (Smith Castelli et al. 2008), and a flow-corrected distance of $D = 38.1 \pm 2.7$ Mpc, accounting for the influence of Virgo infall, the Great Attractor, and the Shapley supercluster. This distance is assumed for NGC 3281 and all nearby sources associated with the Antlia cluster. At a distance of 38.1 Mpc, 1 arcsec corresponds to 0.185 kpc.

2 DATA AND SAMPLE

2.1 MeerKAT Observations

We observed NGC 3281 and the surrounding environment as part of a 10 deg^2 mosaic of the Antlia Cluster with the MeerKAT Telescope (SCI-20210212-KH-01, PI: K. Hess). These observations represent the deepest H i and radio continuum observations of the Antlia cluster to date, covering the full cluster virial radius (887 kpc; Wong et al. 2016) and extending beyond it by approximately 1.2–1.4 times the virial radius along the direction of the Hydra–Antlia filament. The observations consisted of a 10-pointing mosaic taken in 32K mode, observed over eight sessions. The 10 overlapping pointings are shown in Fig. 1. The MeerKAT L-band receivers cover a frequency range of 856 MHz with an RF bandwidth between approximately 900–1670 MHz. In wideband fine (32K) mode, the data are divided into 32,768 channels with a channel width of 26.123 kHz (van der Byl et al. 2022).

In order to maintain the same UV coverage and subsequent PSF across the mosaic, we cycled between the 10 mosaic pointings, interspersed with regular visits to the gain calibrator. Each mosaic pointing was observed for ~ 240 seconds, the gain calibrators were observed ~ 40 minutes apart, and the mosaic pointings were visited 8 times per session. We observed a flux/bandpass and a polarization calibrator at the beginning, middle, and end of each session for a total of 6h20m per observing session. In total, each mosaic pointing

Table 1. H I data cube properties for the four imaging setups. The name given to each cube corresponds to the average of the major and minor axes of the synthesized beam. Listed are the Briggs robustness parameter and applied uv-taper. The resulting resolution is given as the synthesized beam size. The rms noise per channel was computed from a background region. The column density was evaluated at a level of $3\sigma_{\rm NGC3281}\Delta v$, where $\sigma_{\rm NGC\,3281}$ is the level of RMS noise around the mask of NGC 3281 at the respective resolution, calculated by SoFiA 2, and we adopt Δv = 20 km s^{-1}.

name	robust	taper (kλ)	resolution (arcsec)	noise (Jy beam^{-1})	$N_{\rm H\,I,3\sigma}$ (cm^{-2})
70″	0.5	60	71.1″ × 69.3″	3.5×10^{-4}	5.3×10^{18}
48″	0.5	30	49.7″ × 46.1″	2.8×10^{-4}	8.2×10^{18}
30″	0.0	15	34.4″ × 26.2″	2.7×10^{-4}	2.1×10^{19}
16″	0.0	6	20.5″ × 12.1″	2.2×10^{-4}	6.6×10^{19}

had just under 4.5 hours of on-source time before calibration and flagging.

The spectral line and the radio continuum data products were produced following different calibration schemes as described in sections 2.2 and 2.3, respectively.

2.2 Spectral line data reduction

Before spectral line calibration, we split off the frequency range 1390.00–1417.95 MHz. This data from each observing session were subsequently calibrated using the CARACal pipeline (Józsa et al. 2020) on the `ilifu` computer cluster hosted at the Inter-University Institute for Data Intensive Astronomy (IDIA)[1], using standard procedures.

For the spectral line imaging and H I source finding, we followed a similar strategy to what has been developed by the Fornax Cluster Survey (Serra et al. 2023) and MHONGOOSE surveys (de Blok et al. 2024): we imaged the cluster at the lowest spatial resolution first, performed source finding to create a clean mask, cleaned the data, and performed source finding again to create a "final mask". This final mask was then used as the starting point for cleaning the next-highest-resolution image. The source finding was performed using the SoFiA-2 software (Serra et al. 2015; Westmeier et al. 2021), and the cleaning steps were carried out using the Apercal (Adebahr et al. 2022) implementation of Miriad (Sault et al. 2011), parallelized by channel, to clean in the image plane.

At each resolution, the H I cubes for each pointing, per session, were imaged separately from the original UV data, and images from each session of a given pointing were then co-added (as were the PSFs). The co-added pointings were then mosaicked using mosaic-queen to create the full 2.8 deg x 3.6 deg mosaic. Upon inspecting the data we identified two main issues affecting the initial source finding on the lowest resolution mosaic. First, a number of bright H I sources in the field exhibited strong sidelobes. Second, the continuum subtraction performed during the UVLIN step in CARACal was imperfect in the vicinity of bright sources, resulting in negative bowls that biased the initial source finding. Residual continuum was removed prior to cleaning by iteratively fitting and subtracting a natural cubic spline baseline along the spectral axis at each spatial pixel. To mitigate the sidelobe contamination, we first performed a shallow clean on the individual co-added pointings using a 3σ threshold and restricted to the source mask, effectively removing the worst sidelobes, before re-mosaicking them to perform a more complete source finding. Using the resulting initial mask for the full mosaic, the mask was regridded back to the individual pointings and used to guide a subsequent deeper, mask-constrained clean down to a 0.5σ threshold. For the higher-resolution images, the cubic spline continuum subtraction was repeated, but an additional shallow clean was not required, as the cleaning was guided by the mask obtained at the previous resolution.

For the lowest resolution we ran the CARACal imaging step with a robust and taper parameter of $r = 0.5$ and $k\lambda = 60$, respectively. This provided an average resolution of 70″. Then, for the following resolutions we utilized ($r = 0.5, k\lambda = 30$), ($r = 0, k\lambda = 15$), and ($r = 0, k\lambda = 6$), yielding average resolutions of 48″, 30″, and 16″, respectively. Throughout this paper, we will refer to the different resolutions images by these average values. Table 1 provides a summary of our imaging parameters and statistics.

2.3 Radio continuum data reduction

Unlike the spectral line data analysis discussed in the previous section, the radio continuum data reduction included visibility data from the entire observing bandwidth from 900 – 1670 MHz. The raw 32K fine-channelised visibility data were first averaged to the equivalent of visibility data produced by the 4K correlator mode before proceeding with calibration and imaging.

We calibrated and imaged our visibility data following standard prescription using the Common Astronomy Software Application (CASA version 6.4; CASA Team et al. 2022) and `WSClean` (version 3.1; Offringa et al. 2014; Offringa & Smirnov 2017) software packages. The calibration and imaging strategy implemented in our pipeline is functionally similar to other publicly available MeerKAT pipelines like the `IDIA` pipeline[2] and the `CARACal` pipeline[3]. The calibration applied to each target, based on gain solutions derived from the calibrator scans, was further refined through several iterations of phase-only self-calibration and a final phase-and-amplitude self-calibration iteration.

We imaged each target pointing separately using `WSClean`. The calibrated visibilities were Fourier-transformed using the fast W-gridder algorithm (Arras et al. 2021; Ye et al. 2022) with a Briggs visibility weighting scheme (Briggs 1995). The images from the individual pointings were combined using a linear mosaicing strategy, taking the MeerKAT primary beam into account. The radio continuum emission from NGC 3281 is discussed in section 3.2 below. The full radio continuum mosaic will be presented in a future publication.

2.4 Optical imaging

In addition to the MeerKAT observations, we make use of deep optical imaging of the Antlia cluster obtained with the Dark Energy Camera (DECam; Flaugher et al. 2015) in the u, g, and r bands. These images provide the highest quality optical view of NGC 3281 to date and are used throughout this work as a reference for the stellar morphology and surrounding environment. RGB composite images were constructed using the r, g, and u bands, respectively. The r- and g-band emission primarily traces the evolved stellar population and large-scale stellar structure, while the u band is more sensitive to younger stellar populations and regions of recent star formation.

The DECam imaging was reduced following standard procedures

---

[1] `https://www.idia.ac.za/`

[2] `https://github.com/idia-astro/pipelines`

[3] `https://github.com/caracal-pipeline/caracal`

including bias subtraction, flat-fielding, astrometric calibration, background subtraction, and construction of the final mosaics (same procedure as described in Hess et al. 2022; de la Casa et al. 2025).

3 RESULTS

3.1 Optical morphology

Our DECam imaging of the Antlia cluster provides the highest quality optical images of NGC 3281 to date. In Fig. 2 we present a set of panels, where the RGB composite (r, g, and u bands) of NGC 3281 serves as background. This new optical view has clarified some key aspects of its morphology, as we can appreciate more clearly its disturbed morphology than what previous images in the literature might suggest (e.g. Storchi-Bergmann et al. 1992; Dall'Agnol de Oliveira et al. 2023). In addition to the previously seen bright and compact spiral tail on the south-east part of the galaxy, labeled as the "Compact Tail" in Fig. 2, we now see two large diffuse tail-like structures on opposite sides of the disk. Together, they have a characteristic "S" morphology (Toomre & Toomre 1972), labeled as the upper and lower "S" features in Fig. 2, which is a strong indicator of past gravitational interactions. Notably, the tip of the "Compact Tail" is facing towards the end of the diffuse spiral tail on the south-west side, i.e. the "Compact Tail" is facing against the overall rotation direction of the galaxy, further reinforcing the disturbed nature. D23 reported an optical blob, also seen here; located above the "Compact Tail" and east of the galaxy, which they hypothesize could be tied to a minor merger event. This feature is labeled as the "Optical Blob" in Fig. 2.

3.2 Radio continuum

In the top left panel of Fig. 2 we present the MeerKAT radio continuum emission at 1.276 GHz and 7″ resolution overlaid on the optical RGB image, revealing the AGN kpc-scale outflows coming from the center of the galaxy, which extend perpendicularly to the galaxy's major axis in both directions. The one to the north has a projected length (down to the 3 σ level) of 9.5 kpc and the one to the south extends to 8.9 kpc. The core region seen at the highest emission contour (24 σ) is mostly aligned with the minor axis and symmetric, albeit slightly narrower at the north-east side than the south-west end. Further south-west in this direction, there is a dense blob seen at the same contour level.

The lowest emission contours (3, 6, 12 σ) show a much more asymmetric structure. Relative to the minor axis, the northern part is skewed towards the east. In the southern part, we see a large extension towards the east and a smaller portion also to the west. The overall shape of the outflows is reminiscent of that expected from frustrated outflows (Mukherjee et al. 2018a,b), in which the interaction between the AGN-driven material and a dense, clumpy ISM can produce strong shocks and distort the outflow morphology, preventing the gas from expanding efficiently outwards. However, as we will see in the discussion, we suspect some of the asymmetric features are caused by background sources.

East of the outflow, we detect two isolated radio continuum blobs that are smaller than the beam size. One of which coincides with an optical blob that appears to stop at the end of the dust trail. However, this may correspond to a background galaxy. Further to the left is the "Optical Blob" mentioned in D23.

3.3 H I emission and absorption in NGC 3281

In the top right panel of Fig. 2 we show the H I emission and absorption in NGC 3281 at 16″ resolution (~ 3 kpc). At this highest resolution, it is clear that the H I emission does not extend farther than the optical disk, which is characteristic of a truncated H I disk (e.g. Boselli & Gavazzi 2014).

In the bottom left panel of Fig. 2, we show the integrated spectrum and the spectrum at the peak of the H I absorption, which coincides with the center of the galaxy. The deep absorption dominates over the emission, especially close to the center of the galaxy, where there is little to no H I emission. The absorption shows three major dips in the spectrum, where the left-most one has additional subfeatures.

In the bottom right panel of Fig. 2, we show the line of sight velocity map (i.e. the moment 1 map) of the H I emission. The velocity map is consistent with what is expected from a rotating disk. It should be noted that because we are excluding the absorption part on this plot, the velocity gradient does not show a smooth transition between each side of the rotation. On the approaching part (south), the peak of emission is around twice that of the emission on the receding part (north). The H I absorption is a likely culprit for this difference, by blocking more of the emission on one side than on the other. This suspicion is based on the (apparently) redshifted absorption relative to the systemic velocity of the galaxy (taken from D23, see the following subsection). It is also interesting to note that the emission is less extended spatially in the receding part, reaching up to ~ 7.9 kpc along the major axis up until the farthest contour at a column density of 6.6×10^{19} cm^{-2}, while the approaching side reaches ~ 10.5 kpc. Therefore, it is unclear if the lack of emission on the receding side could also be an intrinsic consequence of the remaining H I distribution in the galaxy.

3.4 Kinematics in NGC 3281

To better understand the origin of the apparent redshifted absorption, we used the ALMA CO(2-1) data from D23, and extracted the integrated spectrum, from which they derived a systemic velocity of $v_{\text{sys,LSRK}} = 3332$ km/s in the LSRK system. We utilize this value as our systemic velocity for NGC 3281 since the molecular gas is more centrally concentrated and tightly bound to the galaxy than the H I. We converted this velocity to the barycentric frame (3343 km/s), in which our data are measured, and compare it with our H I spectrum in Fig. 3. The CO spectrum exhibits a double peaked profile, with the systemic velocity located at its midpoint as expected of rotating disk emission. In contrast, the systemic velocity does not pass through the midpoint of the H I spectrum. Rather, the overall emission and absorption appear to be asymmetric with respect to the systemic velocity, with the asymmetry features more redshifted in absorption: the receding side (right of the systemic velocity in Fig. 3) shows two out of the three big dips in the spectrum.

The combination of emission and absorption makes it difficult to determine a proper quantitative value for the overall redshift of the H I relative to the systemic velocity of the galaxy. As it is unclear whether the effect is acting uniformly throughout the entire spectral range or not, or if it is mostly occurring for the H I absorption. An option to estimate this is to take the midpoint of the receding and approaching velocities at the flat part of the H I rotation curve, $v_{\text{rec, flat}}$ and $v_{\text{app, flat}}$, respectively. To (roughly) estimate these values, we constructed a position-velocity (PV) diagram of NGC 3281 in Fig. 4.

We took slices along the major axis of NGC 3281 at the 16″ resolution image. For the slice dimensions we picked a length larger

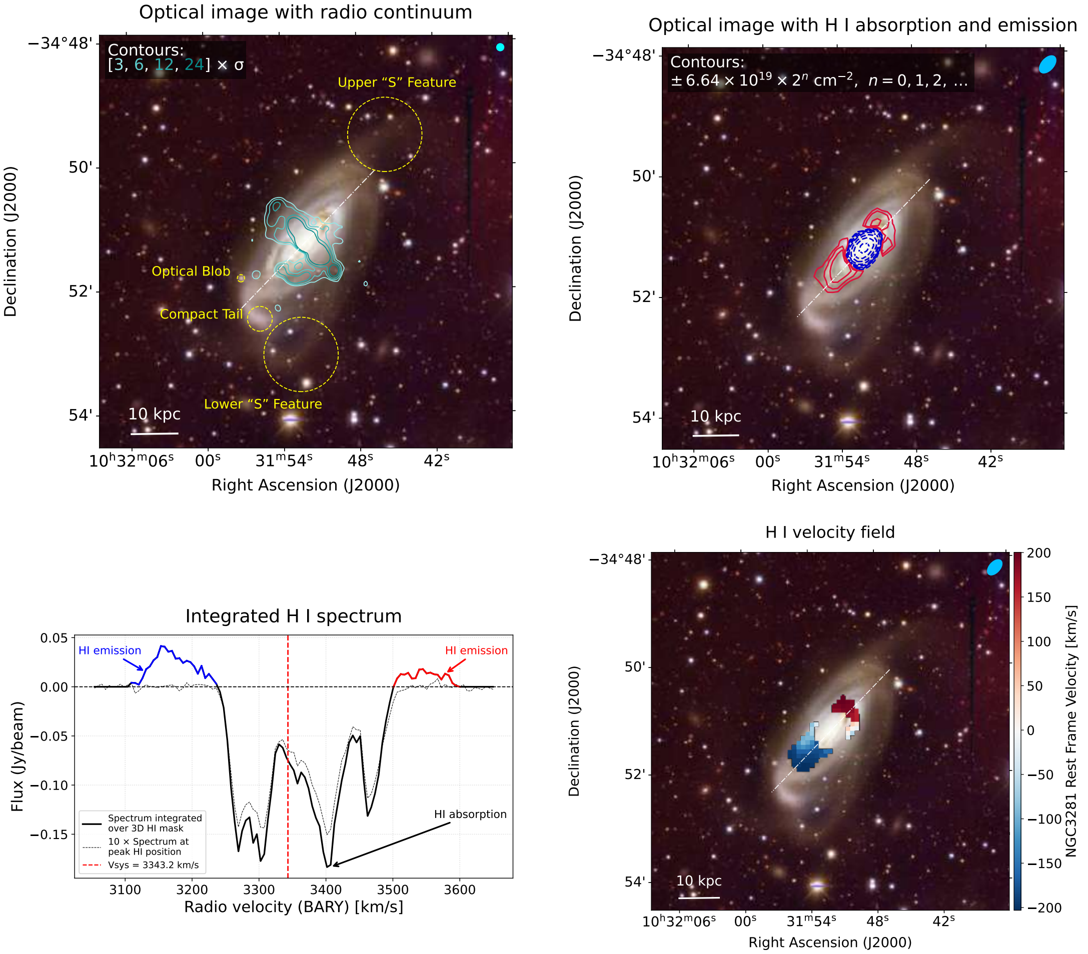

Figure 2. Top left: Radio continuum contours (cyan) overlaid on the optical RGB image of NGC 3281. We utilize the 7″ resolution. The cyan ellipse at the top left corner represents the beam. The dashed yellow circles and labels identify optical features discussed in the text, including the optical blob, compact tail, and the upper and lower "S" features. **Top right:** H I absorption (dashed blue) and emission (solid red) moment 0 contours overlaid on the optical RGB image. We utilize the 16″ resolution. The sky blue ellipse at the top left corner represents the beam. We note that due to spatial overlap of emission and absorption, each pixel of the moment 0 map is composed of the net sum across the spectral axis of positive (emission) and negative (absorption) values, thus this plot is showing the component that dominates at each pixel. **Bottom left:** Integrated H I spectrum within the 3D mask (thick solid line). Highlighted in blue and red is the emission part of the spectrum. The plot also shows the spectrum across the brightest pixel (thin dashed line). The dashed red vertical line represents the systemic velocity of NGC 3281 computed in D23 from CO data. **Bottom right:** Moment 1 of the H I emission, also in the 16″ resolution. The white dash-dotted line shown in the overlay panels represents the optical major axis of the galaxy.

than the H I extent, and we tested various widths using multiples of the beam size: 0.5, 1, 1.5, 2, 2.5. Ultimately we picked 1.5 times the beam size as the best width (23.6″) because the neighboring width options (1 and 2 times the beam size, respectively) yield similar results. This is the one shown in Fig. 4, where the main panel is the PV diagram made from the 23.6″ slice shown in the bottom panel.

Our method of estimating $v_{\rm rec,\,flat}$ and $v_{\rm app,\,flat}$ was performed by selecting the median value between the velocities measured at the outermost point of the three lowest contours. For this we picked the velocity at the first channel where the flux is larger than 2 times the background noise, which is computed as the standard deviation of the corresponding spectrum (at a given spatial extent) after removing all the spectral positions inside the mask. The right panel in Fig. 4 shows the integrated spectrum inside the PV slice, and the integrated background noise. The green horizontal lines in Fig. 4 indicate the selected median velocity. From here we get $v_{\rm rec,\,flat}$ = 246 km/s and $v_{\rm app,\,flat}$ = −206 km/s. The different values are a consequence of the redshifted distribution. The midpoint between these values stands at $v_{\rm mid}$ = 3363 km/s (see dotted blue vertical line in Fig. 3), which

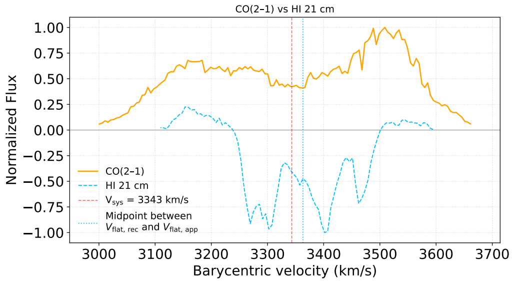

Figure 3. Integrated CO vs H I spectrum. The solid orange line is the (normalized) spectrum of the sum of each spaxel within the 3D mask (integrated spectrum) of the CO data from D23. The dashed light blue line is the (normalized) integrated spectrum of the 3D mask of our H I data. The red dashed vertical line is the systemic velocity of NGC 3281, as calculated from D23. The vertical dotted light blue line is meant to represent the midpoint between the receding and approaching velocities at the flat part of the rotation curve. Of which values were estimated from the PV diagram in Fig. 4.

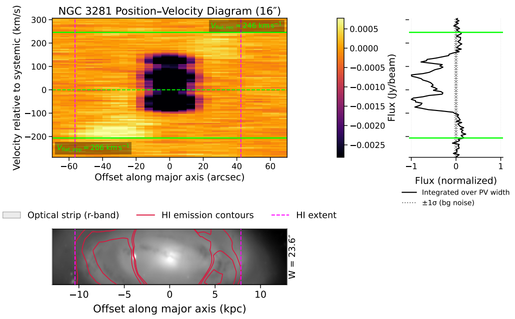

Figure 4. Position-Velocity (PV) diagram of NGC 3281. This PV diagram is made from a slice along the major axis of NGC 3281 at the 16″ resolution image. The width of the slice is 23.6″, which corresponds to ∼ 1.5 times the size of the beam. This region is represented in the bottom panel, showing the optical strip and the overlaid H I moment 0 emission from Fig. 2. The magenta vertical lines represent the extent of the H I emission as given by the lowest contour. On the right side we show the integrated spectrum (black solid line) over the selected PV slice. The dotted lines represents the standard deviation of the background (i.e. excluding pixels within the source mask) inside the PV region. The green horizontal lines represent our selected position of the flat part of the galaxy's rotation. These are measured relative to the systemic velocity of NGC 3281 (dashed green line centered at zero).

provides an estimate of the redshift with respect to the systemic velocity, such that $v_{\rm mid} - v_{\rm sys} \sim 20$ km/s.

After correcting by the inclination of the galaxy $i = 64$, we get $v_{\rm rec,\,flat} = 273.5$ km/s and $v_{\rm app,\,flat} = -229.5$ km/s. The mean of the absolute values yields a final overall velocity of $v_{\rm flat} = 251.5$ km/s. We note that this inclination was derived from the large-scale optical isophotes (Storchi-Bergmann et al. 1992). Although D23 obtained a somewhat different inclination ($i \sim 73°$) from modeling the central CO kinematics, we adopt the optical value here because the H,I traces a more extended component of the galaxy. In addition, the molecular gas distribution in the central regions is known to be kinematically disturbed, showing signatures of outflows and inflows (D23).

We stress that these results should be treated as rough estimations, given the asymmetry and truncated nature of the H I distribution. Nevertheless, we utilize them to provide context and further estimate other quantities (see section 4.1).

3.5 NGC 3281 mass estimation

Although measuring the remaining H I mass in NGC 3281 directly is not possible because of the absorption at the center, we can alternatively apply the H I size-mass relation (Broeils & Rhee 1997) to provide an estimate using the H I emission extent. For this we compute the H I diameter as $D_{\rm H\,I} = 16.2 \pm 1.1$ kpc (87.5″), by measuring the extent of the H I at a column density of 1.25×10^{20} cm^{-2} along the major axis. Then we make use of the linear fit given in equation 2 from Wang et al. (2016), from which we obtain a H I mass of $M_{\rm H\,I} = (7.9 \pm 2.6) \times 10^8\ M_\odot$.

We can estimate the expected H I mass for a galaxy like NGC 3281 using a couple of different methods: one is the optical size of the galaxy, typically used to compute the H I deficiency (Solanes et al. 1996), such that

$$\log_{10}\left(h^2 M_{\rm H\,I,exp}\right) = c + d\ \log_{10}\left[\left(\frac{hD_{25}}{\rm kpc}\right)^2\right], \tag{1}$$

where $M_{\rm H\,I,exp}$ is the expected H I mass, D_{25} is the optical diameter measured at the $\mu_B = 25$ mag arcsec^{-2} isophote, $h = H_0/(100\ {\rm km\,s^{-1}\,Mpc^{-1}}) = 0.73$, and $c = 7.75 \pm 0.08$, $d = 0.595 \pm 0.030$ are the coefficients given for a Sab galaxy, tabulated in table 3 from Boselli & Gavazzi (2009). We utilize a value of $D_{25} = 185.4 \pm 8.7'' = 34.3 \pm 2.9$ kpc from HyperLEDA (Makarov et al. 2014). This method yields a value of $M_{\rm H\,I,exp} = 4.86^{+4.56}_{-2.35} \times 10^9\ M_\odot$ (Logarithmic intrinsic scatter of $\sigma_{\rm int} = 0.26$ dex; Solanes et al. 1996).

Another method we consider is the M_*–$M_{\rm H\,I}$ relation. For this we picked the WISE stellar mass of $\log_{10}(M_*/{\rm M_\odot}) = 9.60 \pm 0.05$ from H15, and use it on the M_*–$M_{\rm H\,I}$ fit from equation 9 in Parkash et al. (2018). We obtain a value of $M_{\rm H\,I,exp} = 2.14^{+3.24}_{-1.29} \times 10^9\ M_\odot$ (Logarithmic intrinsic scatter of $\sigma_{\rm int} = 0.4$ dex; Parkash et al. 2018).

To get a single estimate we combined both methods using a generalized least squares average in logarithmic space (see Appendix A). Because D_{25} and M_* trace related properties, we used a correlation coefficient of 0.5. Ultimately, we obtain $M_{\rm H\,I,exp} = 4.14^{+3.72}_{-1.96} \times 10^9$ M$_\odot$.

Using our value of the remaining H I mass in the galaxy $M_{\rm H\,I}$ and the "healthy" H I mass expectation $M_{\rm H\,I,exp}$, we find that NGC 3281 has lost ∼ 81% of its H I content, due to environmental processes. If we consider the extreme ends of the uncertainties in both quantities, the missing fraction lies somewhere between ∼ 52% and ∼ 93%. Therefore, NGC 3281 has lost more than half of its original H I content.

3.6 Outskirts of NGC 3281

In Fig. 5 we present the H I moment 0 distribution overlaid on top of the optical vicinity of NGC 3281, for each of our different resolutions. The H I moment-0 contours are shown in different colors computed at the level of $3\sigma_{\rm NGC\,3281}\Delta v$, where $\sigma_{\rm NGC\,3281}$ is the level of RMS noise around the mask of NGC 3281 at the respective resolution, calculated by SoFiA 2, and the channel width Δv is set at a standard value of $\Delta v = 20$ km/s. In addition, in Fig. 6 (top panel) we show the velocity map (moment 1) of the 48″ resolution in the same region as in Fig. 5, where the line of sight velocity is centered at the systemic velocity of NGC 3281. We do this to give a sense of the relative proximity of the sources around NGC 3281.

The majority of the H I sources in this region of the sky have an optical counterpart, i.e., they belong to a galaxy. Among these, NGC3258E is the closest galaxy in redshift to NGC 3281 (south-east of NGC 3281), with a mean velocity difference of 300 km/s. Unlike NGC 3281, however, NGC3258E has a larger H I extent than its optical disk. Meaning it still holds a "healthy" amount of H I. South-east of NGC3258E there is another galaxy, GALEX-ASC J103248.40−350425.0, centered at $\alpha_{J2000} = 10^{h}32^{m}48.41^{s}$ and $\delta_{J2000} = -35°04'25.0''$. This source is the second closest galaxy in redshift to NGC 3281, with a velocity difference of 350 km/s. Its H I distribution appears comparable in extent to its optical counterpart.

3.7 Outskirts of NGC 3281: The H I clouds

From the combined multi-resolution H I maps shown in Fig. 5, we identify 5 sources without optical counterparts within 200 km/s of NGC 3281. We refer to these as "clouds" of H I. Three of these clouds are located within ∼ 100 kpc of NGC 3281, while the other two are found farther away toward the cluster center.

The most notable source is the very extended source starting about 85 kpc south-west away from NGC 3281, already discovered in H15. We have called this source the "Big Cloud", and is one of the largest H I sources found in the entirety of Antlia, in terms of its linear size. It is also one of the most massive systems in Antlia. See Fig. 6 (bottom panel) for a closer look on this source H I distribution, where we show the moment 1 map of this cloud in all four resolutions. The most striking feature is its elongated morphology, reaching up to 115 kpc in length at the lowest resolution (70″) and 72 kpc at the highest (16″). Another remarkable feature is the velocity distribution, showing a pattern reminiscent of a rotating disk that surprisingly is oriented along the minor axis of NGC 3281 (see left-bottom panel in Fig. 2), such that the north-west side is receding and the south-east side is approaching. The mass of the cloud is $M_{\mathrm{H\,I,BigCloud}} = 5.79{\times}10^{8}\ \mathrm{M_{\odot}}$.

Nearby, we find two other less massive clouds: "Small Cloud 1" and "Small Cloud 2". They are located at projected distances of ∼ 73 kpc and ∼ 65 kpc from NGC 3281, respectively. Their masses are $M_{\mathrm{H\,I,S1}} = 1.20{\times}10^{7}\ \mathrm{M_{\odot}}$ and $M_{\mathrm{H\,I,S2}} = 1.18{\times}10^{7}\ \mathrm{M_{\odot}}$, respectively. For Small Cloud 1 (directly on the top east edge of the Big Cloud) there is a similar velocity orientation as the Big Cloud, but less defined. And for Small Cloud 2 the velocity distribution does not show an ordered velocity gradient.

Farther away from NGC 3281 in the south-west direction (∼ 360 kpc), there are two clouds near the cluster center, next to one of Antlia's BCGs: NGC 3268. We have called these the "core clouds". These clouds are located at projected distances of ∼ 50–90 kpc from the Antlia cluster center. The smallest one on top has a mass of $M_{\mathrm{H\,I,C1}} = 7.34 \times 10^{6}\ \mathrm{M_{\odot}}$ and the one below has a mass of $M_{\mathrm{H\,I,C2}} = 5.85{\times}10^{7}\ \mathrm{M_{\odot}}$. Both have a rotating-like velocity gradient, but not aligned with NGC 3281 orientation like in the case of the Big Cloud.

All these H I clouds except for the Big Cloud are a completely new discovery, as they were not detected in H15.

Given how close these sources are in redshift to NGC 3281, and the fact they are aligned along the direction toward the cluster center, we constructed a PV diagram using a slice that goes from NGC 3281 all the way to the Core Clouds in Fig. 7. We utilized the 48″ image and a slice width of 450″. The slice is shown below the PV diagram in Fig. 7, with the 48″ H I moment 0 contours overlaid on top of the optical. From this plot it is clear how the three nearby clouds are within 200 km/s on the blue side relative to NGC 3281 systemic velocity, and the core clouds are also within 200 km/s, but on the red side.

4 DISCUSSION

In this section, we explore the recent evolutionary history of NGC 3281 and its connection with the Big Cloud and surrounding smaller H I clouds. We discuss the potential physical processes that lead to their current state. Finally, we relate these findings back to the AGN activity in NGC 3281.

4.1 NGC 3281 past environmental effects and the origin of the Big H I cloud

Our results support a scenario in which NGC 3281 has been significantly affected by its cluster environment, with RPS playing a dominant role in shaping its present-day H I distribution. This is indicated by the truncated H I disk of NGC 3281, the elongated morphology of the Big Cloud, and the strongly one-sided distribution of H I debris, with all detected clouds located to the south-west of the galaxy, toward the cluster center. Such a configuration is consistent with RPS acting on an infalling galaxy that has recently passed pericenter and is now moving away from the cluster core.

At the same time, RPS alone is insufficient to explain the observed gas morphology. Most notably, the Big H I Cloud is fully disconnected from NGC 3281, whereas in many RPS systems stripped gas remains at least partially connected to the host galaxy (e.g. Gavazzi et al. 1995; Chen et al. 2020; Hess et al. 2022). In addition, the Big Cloud exhibits a velocity distribution aligned with the rotation of NGC 3281, suggesting that it inherited its kinematic imprint from the galaxy. The presence of tidal optical features, including the upper and lower "S" features and the "Compact Tail" shown in Fig. 2, further indicates that NGC 3281 has experienced a gravitational perturbation. We therefore argue that a gravitational interaction likely played an important role by loosening the gas reservoir and enabling efficient detachment once ram pressure began acting, in a similar manner to RPS examples observed in the Fornax cluster (Serra et al. 2023). In this framework, the nearby smaller clouds are also likely to be connected to the same event.

Accounting for uncertainties in the expected H I mass of NGC 3281, the combined mass of the Big Cloud and the two Small Clouds would represent between approximately ∼ 9% and ∼ 43% (with a central estimate of ∼ 18%) of the missing H I. This implies that a non-negligible fraction of the stripped gas has survived in the ICM rather than being rapidly mixed or ionized.

In this context, the Big Cloud may represent the most prominent remnant of a RPS tail associated with NGC 3281. However, the lack of a detectable optical counterpart is not trivial. The inferred infalling trajectory of NGC 3281 would provide favorable conditions for efficient stripping, which in many systems leads to in-situ star formation within the stripped tail (e.g. Gavazzi et al. 1995; Gullieuszik et al. 2023). However, even at the highest angular resolution, the Big Cloud reaches only modest H I column densities, with a peak H I column density of $N_{\mathrm{H\,I,peak}} \approx 2.7 \times 10^{20}\ \mathrm{cm^{-2}}$, corresponding to a beam-averaged gas surface density of $\Sigma_{\mathrm{H\,I,peak}} \approx 2.1\ M_{\odot}\ \mathrm{pc^{-2}}$, well below the canonical threshold typically associated with widespread star formation (Kennicutt 1998; Bigiel et al. 2008). Although unresolved sub-kpc density enhancements cannot be excluded at our spatial resolution, the observed gas surface densities suggest that star formation within the cloud would be inefficient overall. At the same time, the estimated timescales since stripping are comparable to the

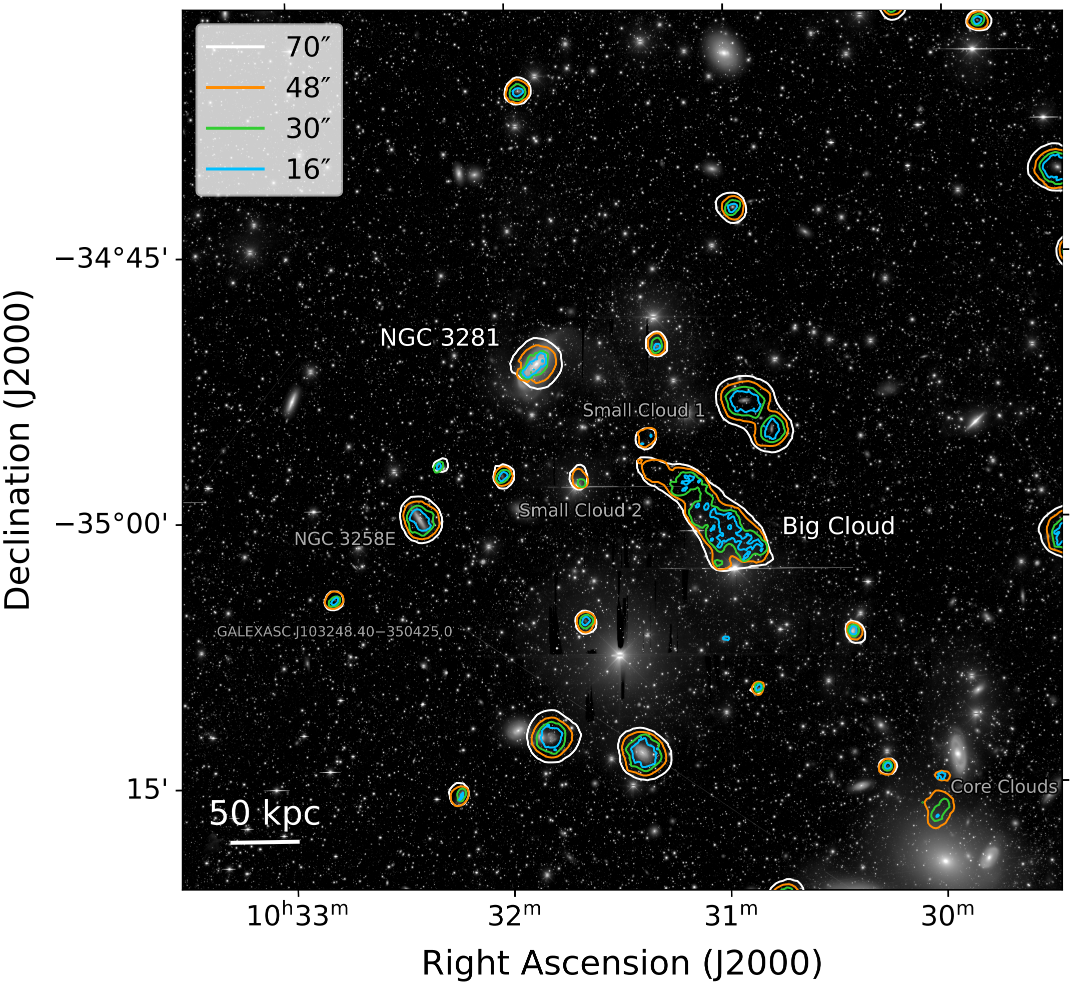

Figure 5. Vicinity around NGC 3281 in the optical (r-band), overlaid with the moment-0 maps of the H I detections for each resolution; white, orange, green, and sky blue from lowest to highest resolution, respectively. The contours around NGC 3281 include both emission and absorption. Each contour was computed at the level of $3\sigma_{\rm NGC3281}\Delta v$ assuming Δv = 20 km s^{-1}, corresponding to column densities of 5.3×10^{18}, 8.2×10^{18}, 2.1×10^{19}, and 6.6×10^{19} cm^{-2} from lowest to highest resolution, respectively.

expected fading times of optical tails produced by in-situ star formation within the ram-pressure-stripped gas. In high-mass clusters, optical RPS tails are estimated to persist for 659^{+281}_{-281} Myr after pericenter (Salinas et al. 2024), which is within the expected timescale since NGC 3281 left pericenter. For a relatively massive galaxy such as NGC 3281, the combination of a weak gravitational perturbation and subsequent RPS may have dispersed the stripped gas over large spatial scales, preventing it from reaching the high densities required for efficient star formation.

Despite evidence for a gravitational perturbation, the stellar disk of NGC 3281 remains largely intact, indicating that any interaction must have been relatively weak. We do not find any obviously perturbed galaxy in the vicinity of NGC 3281 that could have been responsible for the interaction. However, given the inferred trajectory of NGC 3281 through the cluster center, tidal perturbations associated with the cluster potential or interactions near NGC 3268 may also have contributed to disturbing the gas reservoir. The “Compact Tail” observed to the south of NGC 3281 may represent a remnant of such an interaction. Alternatively, if the perturbing companion has already merged with or been disrupted by NGC 3281, the interaction could instead correspond to a past minor merger.

The presence of additional H I clouds near the cluster center at a similar redshift to NGC 3281 suggests that they may be physically connected to its past environmental history. Given that NGC 3281 is likely an infalling system, the spatial distribution of the surrounding H I clouds is consistent with a trajectory in which the galaxy crossed

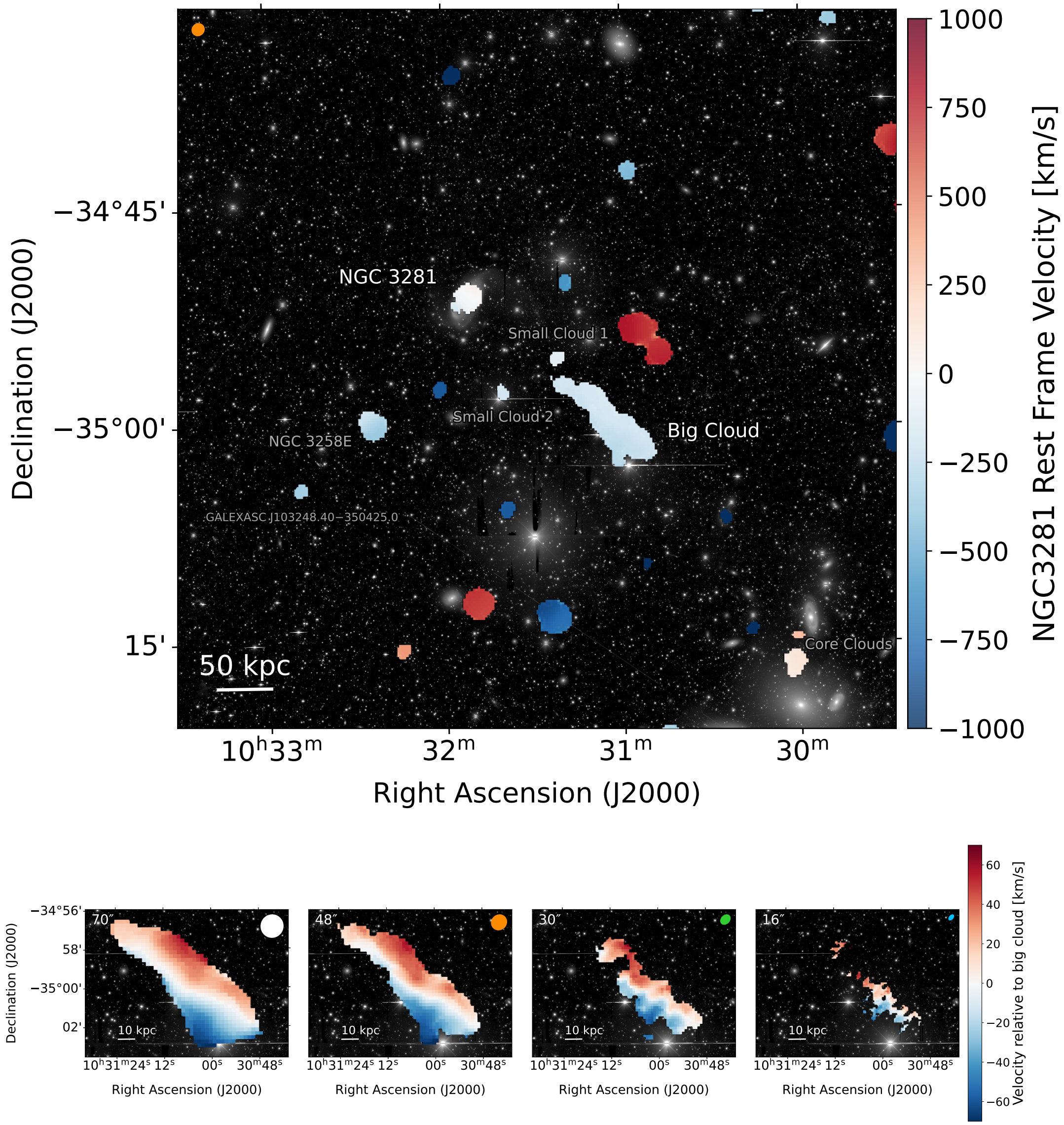

Figure 6. Velocity maps (moment 1) of the H I in the vicinity of NGC 3281. **Top:** Moment-1 velocity field overlaid on the optical (r-band) image at 48″ resolution. **Bottom:** Moment-1 velocity maps of the H I "Big Cloud" at 70″, 48″, 30″, and 16″ resolution (from left to right). Blue colors indicate blueshifted gas and red colors indicate redshifted gas, with velocities centered on the systemic velocity of NGC 3281 (top) and on the flux-weighted systemic velocity of the Big Cloud (bottom), computed above a $3\sigma_{\mathrm{NGC3281}}\Delta\nu$ threshold. Ellipses indicate the synthesized beams, colored according to their respective resolution as in the contours from Fig. 5.

the central cluster region where the Core Clouds are currently located. If so, the interaction or stripping event responsible for the present state of NGC 3281 may have occurred near the cluster core, potentially involving interactions with the massive central galaxies.

The spatial and kinematic configuration of NGC 3281 and the surrounding H I clouds is illustrated by the PV diagram in Fig. 7, which shows NGC 3281 and the nearby H I structures along the same velocity range. In our supposed scenario, NGC 3281 would have crossed the cluster center approximately ∼ 430 kpc (in projection) from its present location, where it would have experienced its max-

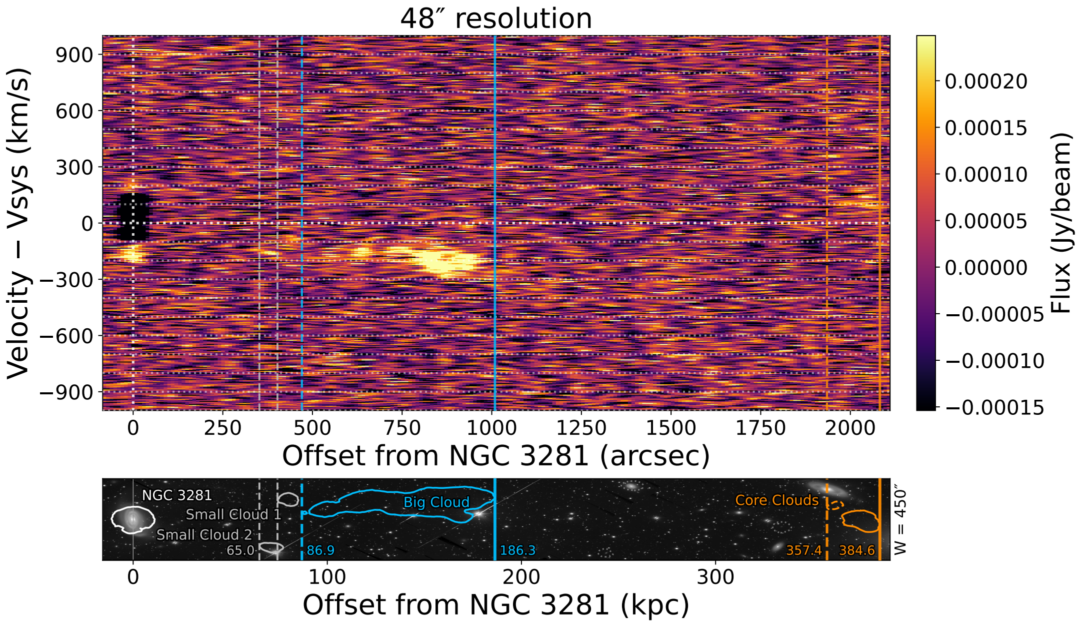

Figure 7. Position-Velocity (PV) diagram of the region along the direction starting at NGC 3281 and ending at the “core clouds”. This PV slice was made with the 48″ resolution image, on a rectangular slice with a width of 450″. This is shown on the bottom subpanel, which shows the optical (r-band) slice with the 48″ resolution moment 0 H I sources overlaid on top. We highlight the sources that are within 200 km/s of the systemic velocity of NGC 3281: the “Big cloud” (cyan), the “small clouds” 1 and 2 (gray), and the “core clouds” (orange). Other sources in the region are marked with a dim dashed gray contour. Gray vertical lines (dashed) mark the closest points from NGC 3281 to the “small clouds” 1 and 2. Cyan vertical lines mark the closest (dashed) and farthest (solid) point from NGC 3281 to the “Big cloud”. Orange vertical lines mark the closest (dashed) and farthest (solid) point from NGC 3281 to the “Core clouds”.

imum ram pressure and likely developed a stripped gas tail. As the galaxy moves away from the cluster core, it would have subsequently passed through the region currently occupied by the Core Clouds.

For the Core Clouds to be physically connected to NGC 3281, the stripped gas must both fully detach from the galaxy and survive in the ICM until the present day. The former is consistent with the need for a gravitational perturbation to weaken the gas reservoir prior to or during stripping. Adopting the velocity dispersion of the Antlia cluster, $\sigma = 656$ km s^{-1} (H15), as a characteristic orbital velocity, and a projected separation of $d_{\mathrm{NGC3281,CC}} \sim 380$ kpc between NGC 3281 and the Core Clouds, the implied survival timescale is $t_{\mathrm{CC}} \sim d_{\mathrm{NGC3281,CC}}/\sigma \sim 570$ Myr.

As NGC 3281 continues to move away from the cluster core, similar considerations apply to the origin of the Big Cloud and the nearby smaller H I clouds, although the required survival times are shorter due to their closer proximity. Using the projected separation to the farthest extent of the Big Cloud, $d_{\mathrm{NGC3281,BC}} \sim 200$ kpc, yields a characteristic timescale of $t_{\mathrm{BC}} \sim 300$ Myr, roughly half of that inferred for the Core Clouds.

An independent estimate of the timescale associated with the Big Cloud can be obtained from its width, which reaches ∼ 45.6 kpc at its widest point. If the gas largely ceased rotating once detached from the galaxy and subsequently expanded radially, then we can utilize the $v_{\mathrm{flat}} = 251.5$ km/s rotation velocity measurement of NGC 3281 (see Section 3.4) as the velocity of the expanding gas. This would yield a timescale of $t_{\mathrm{BC,width}} \sim 350$ Myr, which is fairly consistent with the estimated timescale of t_{BC}, suggesting the Big Cloud left the galaxy ∼ 300 − 350 Myr ago.

Using the H I radius of $R_{\mathrm{H\,I}} \sim 8.1$ kpc derived in Section 3.5, we additionally estimate a characteristic dynamical timescale of $t_{\mathrm{dyn}} = 2\pi R_{\mathrm{H\,I}}/v_{\mathrm{flat}} \sim 200$ Myr for NGC 3281. This suggests that the disturbed gaseous structures could plausibly survive over at least one galactic dynamical time after the stripping event.

One of the earliest well-studied observational examples of a similar phenomenon is the discovery of a large, detached H I plume associated with NGC 4388 in the Virgo cluster, where stripped neutral gas was shown to survive for $\gtrsim 100$ Myr in the ICM (Oosterloo & van Gorkom 2005), consistent with our current findings. However, the projected gap between the host galaxy and the H I cloud is considerably larger in NGC 3281.

The long-term survival of the Big Cloud, despite the apparent absence of a stellar counterpart, may thus reflect the manner in which the gas was removed. A weak gravitational perturbation could have preserved the rotational coherence of the stripped gas, while RPS efficiently displaced it from the galaxy. This may have stabilized the H I against a quick dispersal in the ICM, allowing the Big Cloud to remain detectable for longer.

While the association between NGC 3281 and the Big Cloud, as well as the nearby smaller clouds, is strongly supported by their spatial and kinematic properties, the connection to the Core Clouds remains more speculative. Nevertheless, given the inferred trajectory of NGC 3281 through the cluster core, such a connection remains plausible. One possibility is that the gravitational perturbation affecting NGC 3281 was not a single impulsive event, but instead an ongoing minor merger that disturbed the galaxy over an extended period during its infall. Repeated weak perturbations could have progressively lowered the binding of the cold gas, allowing RPS to detach material in multiple episodes during the galaxy's infall and potentially giving rise to detached H I clouds at different locations along the galaxy's trajectory.

4.2 Feeding of the AGN

One of the most remarkable features of NGC 3281 is the strong H I absorption at its center, the only H I absorption detection in the Antlia cluster. Even more striking is that the absorption is redshifted (by ~ 20 km/s), which is less common than blueshifted H I absorption (Morganti & Oosterloo 2018). Because the absorption is redshifted with respect to the systemic velocity, it has the signature of inflowing gas (e.g. Struve & Conway 2012; Maccagni et al. 2017; Dutta & Srianand 2022). Although redshifted absorption can also arise from circumnuclear rotation (Morganti et al. 2008), the absorption profile does not show a significant blueshifted absorption component or excess, favoring an inflow interpretation. This infall of gas provides evidence for ongoing accretion and feeding of the SMBH, which is ultimately responsible for the AGN outflows that we observe in the radio continuum. Independent evidence for ongoing nuclear fueling in NGC 3281 is provided by its X-ray variability, with NGC 3281 reported to be among the most variable sources in the best-observed subset of Seyfert 2 galaxies (Boorman et al. 2024; P. Boorman, priv. comm.).

To interpret the observed morphology of the radio continuum outflows, we place them in the context of the multi-phase outflow geometry reported in previous works. Storchi-Bergmann et al. (1992) proposed two possible biconical configurations for NGC 3281, with outflow axis inclinations of approximately 64° and 109° with respect to the line of sight. ALMA observations of the molecular gas in D23 favour the latter configuration, in which the outflow axis is tilted with respect to the galaxy disk, corresponding to an offset of ~ 20° from perpendicular. In such a configuration, the outflow propagates through a dense and clumpy ISM and is therefore expected to experience strong interaction. This interaction can promote asymmetric, bubble-like radio structures and provide favourable conditions for the entrainment or survival of cold gas, as shown by numerical simulations of low-power AGN jets interacting with a clumpy ISM (Tanner & Weaver 2022).

Within this framework, the radio continuum morphology of NGC 3281 can be interpreted as being consistent with a tilted outflow whose large-scale appearance is influenced by interaction with the surrounding ISM. This would explain the asymmetric and distorted structures observed at low surface brightness. The higher surface-brightness radio emission, however, appears more symmetric, and the overall emission is roughly perpendicular to the galaxy disk, highlighting that the radio continuum does not necessarily trace the same outflow geometry as the molecular gas. This is not necessarily contradictory, since a similar transition from an inclined launch to an apparently perpendicular large-scale morphology is seen in simulations of jet-disk interactions (Mukherjee et al. 2018b, see Figs. 14–15).

Given the projected extent of the radio continuum outflows, we can give a rough estimate of the characteristic dynamical timescale associated with the current outflow by adopting a representative expansion velocity. For expansion speeds of $v_{\rm out} \sim 200$–500 km s^{-1}, consistent with bulk velocities measured for entrained gas in jet–ISM interaction systems (Müller-Sánchez et al. 2011; Hardcastle et al. 2012) and with expectations from simulations of frustrated, pressure-driven outflows (Mukherjee et al. 2018a,b), the observed radio extent of ~ 9 kpc implies a characteristic timescale of $t_{\rm dyn} \sim 20$–45 Myr.

We note that some of the low-level radio continuum features may be affected by background sources. In particular, the extended feature to the south-east shows a bump in surface brightness at a considerable distance from the main outflow, while the southernmost disconnected emission peak also appears to coincide with an optical blob.

Given the extraordinary circumstances of NGC 3281, showing evidence of both a past gravitational interaction and ram pressure stripping, it is natural to consider whether this evolutionary history has led to the present nuclear activity in the galaxy. In simulations by King & Nixon (2015), gravitational interactions can lower the angular momentum of H I clouds via tidal stress and cloud-cloud collision, facilitating inflow. Multiple works have tried to link environmental effects to the onset of the nuclear activity in galaxies, with mixed conclusions (e.g. Haines et al. 2012; von der Linden et al. 2010; Poggianti et al. 2017; Peluso et al. 2022; Ricarte et al. 2020; Tiwari et al. 2025). NGC 3281 provides a unique detailed example that could bring insight into this debate.

The characteristic timescale inferred for the current radio continuum outflow is significantly shorter than the timescale associated with the formation and survival of the Big H I Cloud. As discussed in Section 4.1, the Big Cloud likely became detached from NGC 3281 approximately ~ 300–350 Myr ago as a result of RPS aided by a gravitational perturbation. Comparing these timescales, the environmental history of NGC 3281 would in principle allow for multiple episodes of nuclear activity since the main stripping event. Assuming characteristic radio outflow timescales of ~ 20–45 Myr, this implies that an upper limit of order ~ 10 such AGN episodes could have occurred.

While proving a direct causal link between the environmental effects and the onset of the AGN activity is challenging, the consistency of the inferred timescales and physical properties provides compelling circumstantial evidence for a connection. In particular, the strong presence of redshifted H I absorption on a truncated H I disk together with the short timescale of the current radio outflow is naturally accommodated within a framework in which large-scale environmental processes have progressively redistributed and destabilised the cold gas reservoir over the past few hundred Myr. In this scenario, RPS and weak gravitational interactions likely helped create favourable conditions for delayed or recurrent SMBH fueling.

5 SUMMARY AND CONCLUSIONS

In this work, we present an environmental view of the galaxy NGC 3281 in the Antlia cluster. Using new deep MeerKAT H I and radio continuum observations, complemented by new deep optical imaging, we examine the neutral gas distribution and radio outflows of the galaxy, together with the H I content of its surrounding environment.

We find that NGC 3281 hosts a truncated H I disk and is missing approximately $\sim 81^{+12}_{-29}$% of its expected H I mass. Compelling evidence indicates that part of this material has been displaced from the galaxy and now resides in a prominent, fully detached H I structure (the Big Cloud), together with two smaller nearby H I clouds, which together account for approximately $\sim 18^{+25}_{-9}$% of the inferred missing H I. All detected H I debris is located on the south-west side of the galaxy, toward the Antlia cluster center.

The truncated H I disk, the strongly one-sided distribution of H I debris, and the extended morphology of the Big Cloud all point toward RPS as the dominant mechanism shaping the observed H I distribution. However, the complete detachment of the Big Cloud, together with its kinematical imprint of the galaxy rotation, suggests that RPS alone is insufficient. This interpretation is further supported by deep optical imaging from DECam, which reveals faint stellar features indicative of a past weak gravitational interaction, likely contributing to the loosening of the gas reservoir of NGC 3281.

Based on its projected separation, spatial extent, and kinematic properties, the Big H I Cloud likely became detached from the galaxy ~ 300–350 Myr ago, placing a lower limit on the survival time of neutral gas in the ICM. In addition, the presence of H I clouds near the Antlia cluster core at a similar redshift to NGC 3281 suggests that stripping-related material may persist even longer, potentially extending this limit to ~ 600 Myr, although the physical association of these Core Clouds with NGC 3281 remains speculative.

NGC 3281 exhibits strong redshifted H I absorption against the nuclear radio continuum, providing direct evidence for ongoing inflow of cold gas toward the nucleus and naturally linking the environmentally processed gas reservoir with the current phase of SMBH fueling.

As a result of the ongoing nuclear fueling, the radio continuum emission of NGC 3281 reveals kpc-scale bipolar outflows emerging from the nuclear region. At high surface brightness, the emission appears relatively symmetric and perpendicular to the galaxy disk, while lower surface-brightness structures are more asymmetric. This morphology is consistent with interaction between the outflowing material and a dense, clumpy ISM.

Compared to the timescales associated with the environmental processes affecting NGC 3281, the inferred timescale for the radio continuum outflows is much shorter. Adopting representative expansion velocities from the literature, we estimate a dynamical timescale of only ~ 20–45 Myr for the present outflow. On this basis, the environmental history of NGC 3281 would allow for multiple episodes of nuclear activity since the main gas stripping event, potentially up to of order ~ 10.

NGC 3281 represents a rare nearby example in which the interplay between environmental processes and AGN activity can be studied in exceptional detail. This work provides the first characterisation of the environmental effects acting on NGC 3281, based on the deepest and highest-resolution H I and radio continuum data available for this system to date. Together, these results highlight how large-scale environmental processes can precondition the cold gas reservoir of cluster galaxies over hundreds of Myr.

Future work will be crucial to further test and refine this picture. Constraints on the thermodynamic state of the Antlia ICM around NGC 3281, such as density and pressure profiles derived from X-ray observations (e.g. Srivastava et al. 2025), would enable direct estimates of the ram pressure experienced by the galaxy along its inferred orbit. Tailored hydrodynamical modeling could allow for a more quantitative assessment of the relative roles of RPS and weak gravitational interactions, and help clarify whether the observed AGN activity can arise naturally from environmentally driven gas redistribution. In that respect, the quantities obtained in this work provide useful constraints. Finally, the data obtained for this work will be used to characterize the H I content of the Antlia cluster as a whole, allowing NGC 3281 to be placed in a broader environmental context. In particular, its location in phase space and its properties relative to other environmentally affected galaxies in Antlia will provide further insight into its evolutionary history.

ACKNOWLEDGEMENTS

The MeerKAT telescope is operated by the South African Radio Astronomy Observatory, which is a facility of the National Research Foundation, an agency of the Department of Science and Innovation. We acknowledge the use of the ilifu cloud computing facility – www.ilifu.ac.za, a partnership between the University of Cape Town, the University of the Western Cape, Stellenbosch University, Sol Plaatje University and the Cape Peninsula University of Technology. The ilifu facility is supported by contributions from the Inter-University Institute for Data Intensive Astronomy (IDIA – a partnership between the University of Cape Town, the University of Pretoria and the University of the Western Cape), the Computational Biology division at UCT and the Data Intensive Research Initiative of South Africa (DIRISA). The MeerKAT data published here have been reduced using the CARACal pipeline, partially supported by ERC Starting grant number 679627 "FORNAX", MAECI Grant Number ZA18GR02, DST-NRF Grant Number 113121 as part of the ISARP Joint Research Scheme, and BMBF project 05A17PC2 for D-MeerKAT. This research was supported by Zhejiang Provincial Natural Science Foundation of China (Grant No. LY24A030001) and the Leading Innovation and Entrepreneurship Team of Zhejiang Province of China (Grant No. 2023R01008). Information about CARACal can be obtained online under the URL: https://caracal.readthedocs.io

DATA AVAILABILITY

REFERENCES

Adebahr B., et al., 2022, Astronomy and Computing, 38, 100514
Arras P., Reinecke M., Westermann R., Enßlin T. A., 2021, A&A, 646, A58
Avirett-Mackenzie M. S., et al., 2024, MNRAS, 528, 6915
Baldry I. K., Balogh M. L., Bower R. G., Glazebrook K., Nichol R. C., Bamford S. P., Budavari T., 2006, MNRAS, 373, 469
Bigiel F., Leroy A., Walter F., Brinks E., de Blok W. J. G., Madore B., Thornley M. D., 2008, AJ, 136, 2846
Blandford R. D., Rees M. J., 1974, MNRAS, 169, 395
Boorman P. G., et al., 2024, Frontiers in Astronomy and Space Sciences, 11, 1335459
Boselli A., Gavazzi G., 2006, PASP, 118, 517
Boselli A., Gavazzi G., 2009, A&A, 508, 201
Boselli A., Gavazzi G., 2014, A&ARv, 22, 74
Briggs D., 1995, PhD thesis, PhD Thesis, New Mexico Institute of Mining and Technology
Broeils A. H., Rhee M. H., 1997, A&A, 324, 877
Byrd G., Valtonen M., 1990, ApJ, 350, 89
CASA Team et al., 2022, PASP, 134, 114501
Cayatte V., van Gorkom J. H., Balkowski C., Kotanyi C., 1990, AJ, 100, 604
Chaturvedi A., Tonnesen S., Bryan G. L., Popping G., Hilker M., Serra P., Genel S., 2024, ApJ, 969, 28
Chen H., et al., 2020, MNRAS, 496, 4654
Chung A., van Gorkom J. H., Kenney J. D. P., Crowl H., Vollmer B., 2009, AJ, 138, 1741
Cortese L., Catinella B., Smith R., 2021, Publ. Astron. Soc. Australia, 38, e035
Cowie L. L., Songaila A., 1977, Nature, 266, 501
Dall'Agnol de Oliveira B., Storchi-Bergmann T., Morganti R., Riffel R. A., Ramakrishnan V., 2023, MNRAS, 522, 3753
Davies R. D., Lewis B. M., 1973, MNRAS, 165, 231
Di Matteo T., Springel V., Hernquist L., 2005, Nature, 433, 604
Dressler A., 1980, ApJ, 236, 351
Dressler A., Thompson I. B., Shectman S. A., 1985, ApJ, 288, 481
Dutta R., Srianand R., 2022, MNRAS, 516, 4338
Fabian A. C., 2012, ARA&A, 50, 455
Fiore F., et al., 2017, A&A, 601, A143

Flaugher B., et al., 2015, AJ, 150, 150

Gavazzi G., Contursi A., Carrasco L., Boselli A., Kennicutt R., Scodeggio M., Jaffe W., 1995, A&A, 304, 325

Gavazzi G., Fumagalli M., Cucciati O., Boselli A., 2010, A&A, 517, A73

Giovanelli R., Haynes M. P., 1985, ApJ, 292, 404

Gullieuszik M., et al., 2023, ApJ, 945, 54

Gunn J. E., Gott III J. R., 1972, ApJ, 176, 1

Haines C. P., et al., 2012, ApJ, 754, 97

Hank N. A. N., Verheijen M. A. W., Blyth S.-L., Davé R., Oman K. A., Deg N., Glowacki M., 2025, MNRAS, 540, 3047

Hardcastle M. J., et al., 2012, MNRAS, 424, 1774

Harrison C. M., 2017, Nature Astronomy, 1, 0165

Hess K. M., Jarrett T. H., Carignan C., Passmoor S. S., Goedhart S., 2015, MNRAS, 452, 1617

Hess K. M., Kotulla R., Chen H., Carignan C., Gallagher J. S., Jarrett T. H., Kraan-Korteweg R. C., 2022, A&A, 668, A184

Hibbard J. E., van Gorkom J. H., 1996, AJ, 111, 655

Hopkins P. F., Quataert E., 2010, MNRAS, 407, 1529

Jaffé Y. L., et al., 2016, MNRAS, 461, 1202

Jaffé Y. L., et al., 2018, MNRAS, 476, 4753

Jonas J., MeerKAT Team 2016, in MeerKAT Science: On the Pathway to the SKA. p. 1, doi:10.22323/1.277.0001

Józsa G. I. G., et al., 2020, in Pizzo R., Deul E. R., Mol J. D., de Plaa J., Verkouter H., eds, Astronomical Society of the Pacific Conference Series Vol. 527, Astronomical Data Analysis Software and Systems XXIX. p. 635 (`arXiv:2006.02955`), doi:10.48550/arXiv.2006.02955

Józsa G. I. G., et al., 2022, ApJ, 926, 167

Kennicutt Jr. R. C., 1983, AJ, 88, 483

Kennicutt Jr. R. C., 1998, ApJ, 498, 541

Kennicutt Jr. R. C., Keel W. C., van der Hulst J. M., Hummel E., Roettiger K. A., 1987, AJ, 93, 1011

King A., Nixon C., 2015, MNRAS, 453, L46

Kleiner D., et al., 2021, A&A, 648, A32

Koopmann R. A., 2008, in Davies J. I., Disney M. J., eds, IAU Symposium Vol. 244, Dark Galaxies and Lost Baryons. pp 362–363 (`arXiv:0707.3277`), doi:10.1017/S1743921307014287

Kormendy J., Ho L. C., 2013, ARA&A, 51, 511

Liu J.-R., Feng H., Wang J.-M., 2025, arXiv e-prints, p. arXiv:2509.21958

Lopes P. A. A., Ribeiro A. L. B., Rembold S. B., 2017, MNRAS, 472, 409

Maccagni F. M., Morganti R., Oosterloo T. A., Geréb K., Maddox N., 2017, A&A, 604, A43

Maier C., Haines C. P., Ziegler B. L., 2022, A&A, 658, A190

Makarov D., Prugniel P., Terekhova N., Courtois H., Vauglin I., 2014, A&A, 570, A13

Makino J., Hut P., 1997, ApJ, 481, 83

Martini P., Mulchaey J. S., Kelson D. D., 2007, ApJ, 664, 761

Mayer L., Mastropietro C., Wadsley J., Stadel J., Moore B., 2006, MNRAS, 369, 1021

Merritt D., 1983, ApJ, 264, 24

Moore B., Lake G., Katz N., 1998, ApJ, 495, 139

Morganti R., Oosterloo T., 2018, A&ARv, 26, 4

Morganti R., Oosterloo T., Tsvetanov Z., 1998, AJ, 115, 915

Morganti R., Oosterloo T., Struve C., Saripalli L., 2008, A&A, 485, L5

Mukherjee D., Wagner A. Y., Bicknell G. V., Morganti R., Oosterloo T., Nesvadba N., Sutherland R. S., 2018a, MNRAS, 476, 80

Mukherjee D., Bicknell G. V., Wagner A. Y., Sutherland R. S., Silk J., 2018b, MNRAS, 479, 5544

Müller-Sánchez F., Prieto M. A., Hicks E. K. S., Vives-Arias H., Davies R. I., Malkan M., Tacconi L. J., Genzel R., 2011, ApJ, 739, 69

Nakazawa K., Makishima K., Fukazawa Y., Tamura T., 2000, PASJ, 52, 623

Nesvadba N. P. H., et al., 2021, A&A, 654, A8

Nulsen P. E. J., 1982, MNRAS, 198, 1007

Offringa A. R., Smirnov O., 2017, MNRAS, 471, 301

Offringa A. R., McKinley B., Hurley-Walker et al., 2014, MNRAS, 444, 606

Oosterloo T., van Gorkom J., 2005, A&A, 437, L19

Ostriker J. P., 1980, Comments on Astrophysics, 8, 177

Parkash V., Brown M. J. I., Jarrett T. H., Bonne N. J., 2018, ApJ, 864, 40

Peluso G., Poggianti B., Vulcani B., Moretti A., Radovich M., 2022, in 44th COSPAR Scientific Assembly. Held 16-24 July. p. 2336

Peng Y.-j., et al., 2010, ApJ, 721, 193

Phillips M. M., Charles P. A., Baldwin J. A., 1983, ApJ, 266, 485

Poggianti B. M., et al., 2017, Nature, 548, 304

Rees M. J., 1984, ARA&A, 22, 471

Reynolds T. N., Westmeier T., Staveley-Smith L., Chauhan G., Lagos C. D. P., 2020, MNRAS, 493, 5089

Rhee J., Smith R., Choi H., Yi S. K., Jaffé Y., Candlish G., Sánchez-Jánssen R., 2017, ApJ, 843, 128

Ricarte A., Tremmel M., Natarajan P., Quinn T., 2020, ApJ, 895, L8

Sales D. A., Pastoriza M. G., Riffel R., Winge C., Rodríguez-Ardila A., Carciofi A. C., 2011, ApJ, 738, 109

Salinas V., et al., 2024, MNRAS, 533, 341

Sault R. J., Teuben P., Wright M. C. H., 2011, MIRIAD: Multi-channel Image Reconstruction, Image Analysis, and Display, Astrophysics Source Code Library, record ascl:1106.007 (ascl:1106.007)

Serra P., et al., 2013, MNRAS, 428, 370

Serra P., et al., 2015, MNRAS, 448, 1922

Serra P., et al., 2023, A&A, 673, A146

Serra P., et al., 2024, A&A, 690, A4

Shlosman I., Frank J., Begelman M. C., 1989, Nature, 338, 45

Silk J., Rees M. J., 1998, A&A, 331, L1

Smith Castelli A. V., Bassino L. P., Richtler T., Cellone S. A., Aruta C., Infante L., 2008, MNRAS, 386, 2311

Smith R., Tonnesen S., Kraljic K., Calderón-Castillo P., Marasco A., Jaffe Y., Vulcani B., Poggianti B. M., 2025, A&A, 701, A6

Solanes J. M., Giovanelli R., Haynes M. P., 1996, ApJ, 461, 609

Solanes J. M., Manrique A., García-Gómez C., González-Casado G., Giovanelli R., Haynes M. P., 2001, ApJ, 548, 97

Spitzer Lyman J., Baade W., 1951, ApJ, 113, 413

Srivastava A., Reiprich T. H., Veronica A., Pacaud F., Dietl J., Knies F., Sasaki M., 2025, arXiv e-prints, p. arXiv:2512.00518

Storchi-Bergmann T., Wilson A. S., Baldwin J. A., 1992, ApJ, 396, 45

Struve C., Conway J. E., 2012, A&A, 546, A22

Tanner R., Weaver K. A., 2022, AJ, 163, 134

Tiwari J., Sun M., Luo R., Fossati M., Chen Chien-Ting J., Tamhane P., 2025, ApJ, 979, 134

Toomre A., Toomre J., 1972, ApJ, 178, 623

Vásquez-Bustos P., Argudo-Fernández M., Boquien M., Castillo-Baeza N., Castillo-Rencoret A., Ariza-Quintana D., 2025, A&A, 696, A206

Wang J., Koribalski B. S., Serra P., van der Hulst T., Roychowdhury S., Kamphuis P., Chengalur J. N., 2016, MNRAS, 460, 2143

Warmels R. H., 1988, A&AS, 72, 427

Westmeier T., et al., 2021, MNRAS, 506, 3962

Whitmore B. C., Gilmore D. M., Jones C., 1993, ApJ, 407, 489

Winter L. M., Mushotzky R. F., Reynolds C. S., Tueller J., 2009, ApJ, 690, 1322

Wong K.-W., Irwin J. A., Wik D. R., Sun M., Sarazin C. L., Fujita Y., Reiprich T. H., 2016, ApJ, 829, 49

Ye H., Gull S. F., Tan S. M., Nikolic B., 2022, MNRAS, 510, 4110

de Blok W. J. G., et al., 2024, A&A, 688, A109

de la Casa C. C., et al., 2025, A&A, 704, A264

van der Byl A., et al., 2022, Journal of Astronomical Telescopes, Instruments, and Systems, 8, 011006

von der Linden A., Wild V., Kauffmann G., White S. D. M., Weinmann S., 2010, MNRAS, 404, 1231

APPENDIX A: GENERALIZED LEAST SQUARES COMBINATION OF H I MASS ESTIMATES

In Section 3.5 we estimate the expected H I mass of an unperturbed NGC 3281 using two scaling relations that trace different global galaxy properties: (i) using the optical size D_{25} (Boselli & Gavazzi 2009), and (ii) the stellar mass M_* (Parkash et al. 2018). Each relation provides an estimate of $\log_{10} M_{\mathrm{H\,I,exp}}$ with an associated uncertainty expressed in dex. Because D_{25} and M_* trace related galaxy structure, these two estimates are not strictly independent. We therefore combine them using a generalized least squares average in logarithmic space, allowing for covariance between the predictors.

We define the vector of logarithmic expected H I masses

$$\boldsymbol{\mu} = \begin{pmatrix} \mu_1 \\ \mu_2 \end{pmatrix} = \begin{pmatrix} \log_{10} M^{(D_{25})}_{\mathrm{H\,I,exp}} \\ \log_{10} M^{(M_*)}_{\mathrm{H\,I,exp}} \end{pmatrix}, \tag{A1}$$

with corresponding uncertainties

$$\boldsymbol{\sigma} = \begin{pmatrix} \sigma_1 \\ \sigma_2 \end{pmatrix}. \tag{A2}$$

We construct the covariance matrix

$$\boldsymbol{\Sigma} = \begin{pmatrix} \sigma_1^2 & \rho\,\sigma_1\sigma_2 \\ \rho\,\sigma_1\sigma_2 & \sigma_2^2 \end{pmatrix}, \tag{A3}$$

and adopt a correlation coefficient of $\rho = 0.5$.

The generalized least squares estimator for the combined expected H I mass is

$$\mu_{\mathrm{GLS}} = \frac{\mathbf{1}^{\mathsf{T}}\boldsymbol{\Sigma}^{-1}\boldsymbol{\mu}}{\mathbf{1}^{\mathsf{T}}\boldsymbol{\Sigma}^{-1}\mathbf{1}}, \tag{A4}$$

where $\mathbf{1} = (1, 1)^{\mathsf{T}}$, with variance

$$\sigma^2_{\mathrm{GLS}} = \left(\mathbf{1}^{\mathsf{T}}\boldsymbol{\Sigma}^{-1}\mathbf{1}\right)^{-1}. \tag{A5}$$

The combined expected H I mass is then given by

$$\log_{10} M_{\mathrm{H\,I,exp}} = \mu_{\mathrm{GLS}} \pm \sigma_{\mathrm{GLS}}, \tag{A6}$$

This paper has been typeset from a TEX/LATEX file prepared by the author.